

REVIEW ARTICLE

Novel hydrodynamic phenomena in superfluid ^3He

A. P. Finne¹, V. B. Eltsov^{1,2}, R. Hänninen^{1,4}, N. B. Kopnin^{1,3},
J. Kopu¹, M. Krusius¹, M. Tsubota⁴, and G. E. Volovik^{1,3}

¹Low Temperature Laboratory, Helsinki University of Technology, P.O. Box 2200, FIN-02015 HUT, Finland

²Kapitza Institute for Physical Problems, 119334, Moscow, Russia

³Landau Institute for Theoretical Physics, 119334, Moscow, Russia

⁴Department of Physics, Osaka City University, Osaka 558-8585, Japan

Abstract. The superfluid phases of ^3He are systems with unique properties. The most interesting ones are revealed under rotation, when different types of topological defects can be seen with NMR measurement. Here we report on new observations in rotating flow. These include (1) the coexistence of continuous vortices (skyrmions) and singular vortices across the interface between two superfluids with essentially different properties, $^3\text{He-A}$ and $^3\text{He-B}$, and (2) the analog of the Kelvin-Helmholtz instability for the A-B interface when the two superfluids are sliding with respect to each other without friction. The latter is the first realization of an ideal shear-flow instability, which is not distorted by viscosity. Also, (3) a sharp transition between laminar and turbulent superfluid flow was observed for the first time. As distinct from the transition to turbulence in normal liquids, which is governed by the conventional Reynolds number, the observed transition is controlled by a new velocity-independent parameter. This parameter also modifies the Kolmogorov-Obukhov scaling law of the developed turbulence. Finally, (4) a helically twisted vortex state behind a propagating front of quantized vorticity was observed and identified. This front separates the Landau vortex-free state from the equilibrium vortex state in a rotating container, which imitates the solid-body rotation of a superfluid liquid.

Submitted to: *Rep. Prog. Phys.*

PACS numbers: 67.40.Vs, 67.57.De, 47.27.-i

1. Helium superfluids

Until 1972 the only known example of a truly inviscid fluid was superfluid $^4\text{He-II}$ at low flow velocities. Today its primacy is challenged by the discovery of superfluid ^3He in 1972 and the gaseous Bose-Einstein condensates in 1995. Nevertheless, in low temperature physics $^4\text{He-II}$ remains the epitome of a superfluid, the benchmark to which to compare to. Its perfect inviscid flow is known to persist only at velocities below some low critical limit at which quantized vortex lines are formed. These are topologically stable linear defects in the superfluid order parameter field with extraordinary properties. One of them is their turbulent flow, customarily known as superfluid turbulence or quantum turbulence, which appears, for instance, when the applied flow velocity is suddenly increased well above the critical limit. Recently the dynamics of quantized vortex lines has gained renewed interest, activated by the differences and similarities which have been discovered while exploring the other superfluid systems. A recent review by Vinen and Niemela [1] summarizes with updated references our understanding on vortex dynamics and turbulence in $^4\text{He-II}$.

The superfluid phases of ^3He provide a much broader spectrum of phenomena related to the beautiful world of vortices and other topological defects. Many of these phenomena have been discussed in earlier review papers and books [2, 3, 4, 5]. This review deals with the most recent observations made with a rotating cryostat in the Low Temperature Laboratory of the Helsinki University of Technology.

As bulk liquid, superfluid ^3He can exist in two different phases, $^3\text{He-A}$ and $^3\text{He-B}$ (there is also the third phase $^3\text{He-A}_1$ emerging at high magnetic field very close to the superfluid transition temperature T_c [6]). The flow properties of $^3\text{He-B}$ are isotropic in the absence of external fields, closely resembling the flow properties of $^4\text{He-II}$ with its quantized vorticity. One important difference between $^4\text{He-II}$ and $^3\text{He-B}$ concerns the vortex-core size, which is determined by the coherence length ξ of the superfluid. In $^4\text{He-II}$ the core radius is of atomic scale ~ 0.1 nm, while in $^3\text{He-B}$ it is $\gtrsim 10$ nm and thus at least two orders of magnitude larger. As we demonstrate in this review, this difference is not simply quantitative but has a substantial impact on the vortex dynamics in these two superfluids.

We now outline briefly the three main topics which are the subject of this review. $^3\text{He-A}$ is the most extraordinary superfluid of all that we know and its applications as a model system in physics have far reaching implications [5]. Most importantly, superfluid $^3\text{He-A}$ is an essentially anisotropic liquid and its vorticity is not quantized in general. Therefore, its flow allows for continuous vorticity. When the tiny dipolar coupling between the spin and orbital momenta of the Cooper pairs is taken into account, the vorticity of $^3\text{He-A}$ becomes quantized. However, it is continuously distributed throughout the vortex-core region, whose structural length scale is not the superfluid coherence length but the three orders of magnitude larger healing length $\xi_D \gtrsim 10 \mu\text{m}$ associated with dipolar coupling. Moreover, the typical continuous vortex is doubly quantized, *i.e.* its circulation is twice that of a $^3\text{He-B}$ vortex. Such a huge difference

between the vortices poses the problem of what happens at the boundary between these two liquids in the rotating container, or how the doubly-quantized continuous and singly-quantized singular vortices match each other across the interface (Sec. 2.1). The experimental resolution of this problem led us to the unexpected observation of dissipationless shear flow between two superfluids. The stability issues of such a state defines the first topic discussed in this review.

The possibility of constructing the shear flow arises as a result of different conditions for the vortex formation and pinning in the two superfluids. Both these properties are essentially determined by the vortex-core size. The core size of a $^3\text{He-B}$ vortex is intermediate between that in $^4\text{He-II}$ and $^3\text{He-A}$, which leads to very important consequences. On one hand, it is much larger than the microscopic core size in $^4\text{He-II}$. Therefore, pinning and surface roughness at bounding walls is not as important as in $^4\text{He-II}$. As distinct from $^4\text{He-II}$, with carefully chosen and prepared container surfaces pinning sites can be avoided, so that remanent vortex lines pinned to the surfaces do not exist. In that case, substantial vortex-free flow can be reached in a rotating container, before intrinsic vortex formation starts to intervene at relatively high critical velocities. In contrast, in $^4\text{He-II}$ vortex-free flow has generally little practical meaning because, even at very low velocities, remanent vorticity leads to efficient vortex formation. An important exception is flow through a sub-micron-size aperture in a thin membrane where the vortices are swept away from the immediate vicinity of the high-velocity flow and do not have a chance to become pinned there [7].

On the other hand, the core size of a $^3\text{He-B}$ vortex is much smaller than that of a continuous vortex in $^3\text{He-A}$. As a result, the critical velocity for the intrinsic vortex formation in $^3\text{He-B}$ is much larger than in $^3\text{He-A}$. This enables us to prepare a flow state in which vortices are already formed on the A-phase side of the interface, while on the B-phase side the vortex-free Landau state persists. This leads to a shear-flow state in which the two superfluids are sliding along each other. The relative flow of two superfluids is frictionless and, for the first time, provides a perfect arrangement for the experimental investigation of the classical Kelvin-Helmholtz instability which was theoretically predicted about hundred years ago (Sec. 2.4). In conventional liquids, the instability threshold for the formation of surface waves – ripples – is always smeared by viscosity.

Unexpectedly, even under these perfect conditions, the critical velocity for the onset of instability did not match the classical result derived for ideal liquids/gases (Sec. 3). The true modified criterion for the onset of instability, which proved to be in excellent agreement with experimental data, has at first glance paradoxical consequences. In particular, the instability threshold is not determined by the velocity $\mathbf{v}_{s2} - \mathbf{v}_{s1}$ of the relative superfluid motion of two liquids; the instability would occur even if the liquids would have the same superfluid velocity. Moreover, the instability would occur even for a single superfluid with a free surface. These new features result from the two-fluid nature of the superfluid liquid, which consists of the superfluid and normal fractions. The instability threshold is determined by the velocities $\mathbf{v}_{s1,2} - \mathbf{v}_n$ of each superfluid with

respect to the reference frame of the walls and thus with respect to the normal fractions of the two liquids, which in thermodynamic equilibrium move together with walls. In particular, the interface between the superfluid liquid and the vacuum becomes unstable when in the reference frame of the normal fraction the superfluid velocity exceeds the critical value [8, 9]. In the case of several (k) superfluid fractions in the same liquid, such as neutron and proton superfluid components in neutron stars, the threshold is determined by some combination of the superfluid velocities $\mathbf{v}_{sk} - \mathbf{v}_n$ [10].

Surprisingly, the observed mechanism of the interface instability, which is different from that in classical liquids, has many common features with the instability of the quantum vacuum beyond the horizon or in the ergoregion of the black hole. Here the ergoregion is defined as the region at the interface where the energy of surface waves, or ripplons, is negative. As excitations living at the interface, ripplons also provide a connection to the presently popular idea in cosmology, according to which the matter in our Universe lives on a hypersurface (membrane or simply brane) in a multidimensional space. Branes can be represented by topological defects, such as domain walls and strings, and by interfaces between different quantum vacua. In our case, the brane is defined by the interface between two quantum vacua – two superfluid phases of ^3He . The discussed instability of the A-B interface is thus in one-to-one correspondence to the instability of the quantum vacuum in the brane world. It occurs in the ergoregion because of the interaction between the matter living on the brane (represented by ripplons) and the matter living in higher-dimensional space (represented by quasiparticles in bulk superfluids).

Experiments with the A-B interface also revealed new behavior related to superfluid turbulence (Sec. 4), which is the second main topic discussed in this review. The non-linear stage in the development of the interface instability results in the injection of a few vortices from the interface into the rapidly moving $^3\text{He-B}$. It was found that the injection may or may not lead to turbulent flow in $^3\text{He-B}$. The fate of injected vortices depends on the value of a dimensionless intrinsic parameter q , which characterizes the mutual friction between the vortices and the normal component of the liquid. At q of order unity, a rather sharp transition is observed between the laminar evolution of the injected vortices at $q \gtrsim 1$ and the emerging turbulent many-vortex state of the whole superfluid at $q \lesssim 1$ [11].

In the Fermi superfluid $^3\text{He-B}$ the mutual friction between the vortices and the normal component is mediated by the fermionic quasiparticles living in the vortex core [12, 13, 14, 15], the so-called fermion zero modes. Their behavior is described by a theory similar to the BCS theory of superconductivity, according to which the temperature-dependent parameter $q(T)$, which is the ratio of the dissipative and reactive components of the mutual friction force, is a dimensionless function of T/T_c . The main reason why the transition separating the laminar and turbulent behavior has only been observed in $^3\text{He-B}$, and not in superfluid ^4He , is the favorable value of the parameter $q(T)$ in $^3\text{He-B}$ – crossing unity at $T \sim 0.6T_c$. The fortunate coincidence of a hydrodynamic transition in the middle of the experimentally accessible temperature range in $^3\text{He-B}$

enables exploring the dynamics in both flow regimes under otherwise similar conditions. In the Bose liquid $^4\text{He-II}$ the vortex dynamics is practically always turbulent. Laminar flow could be expected only within a few μK below the superfluid transition temperature T_λ from where there are no experiments available on vortex dynamics for comparison. Even there, the low viscosity of the normal component (in $^4\text{He-II}$ the normal component is one of the least viscous fluids) causes its flow to become easily turbulent, which can in turn influence the flow of the superfluid component.

In contrast, the normal component in ^3He superfluids has oil-like viscosity and is practically always in the state of laminar flow. The absence of turbulence in the flow of the normal component of $^3\text{He-B}$ amounts to a considerable simplification and to new effects that are not present in $^4\text{He-II}$. It gives rise to a new scaling law for the Kolmogorov-Richardson cascade in developed superfluid turbulence, depending on two Reynolds parameters: one velocity-dependent and the other independent on velocity (Sec. 4).

Of particular significance has been the exponentially steep temperature dependence of the laminar to turbulent transition which has allowed a whole new genre of studies on how turbulence is switched on. Probably the most interesting consequence of that is the observation of the propagating vortex front in a rotating container (Sec. 5). The front separates the metastable Landau vortex-free state from the equilibrium vortex state, which imitates the solid body rotation of superfluid liquid. Moreover, the motion of the front in the rotating container leads to the helical twisting of the propagating vortices, which can be experimentally detected. The considerations related to these observations form the third topic of the present review.

The above issues have been in the forefront of recent research and are in the focus of this review. They demonstrate the new features of the general phenomenon of superfluidity which have been revealed because of the much richer structure of superfluidity in ^3He compared to the ‘classical’ superfluidity of $^4\text{He-II}$, and which will be further exploited in the new superfluid states of the cold Bose and Fermi gases.

In addition to their hydrodynamic differences, $^4\text{He-II}$ and $^3\text{He-B}$ experiments often use different techniques to create and detect vortex lines. The temperature required for superfluid ^3He is a factor of 10^3 lower than for $^4\text{He-II}$. This sets restrictions on the type of experiments that can be conducted on ^3He superfluids. Uniform rotation can be used in any temperature range to create a hydrodynamic counterflow of the normal and superfluid components. Owing to better control over vortex formation in ^3He superfluids, rotation has proven to be a much more useful tool there to apply flow. In the zero-temperature limit, where the normal component becomes exponentially rarefied and no longer causes excessive viscous heating, vibrating wires [16] or grids [17] have been employed in the quiescent $^3\text{He-B}$ bath to create vortices. The oscillation is driven at amplitudes where the flow velocity at the surface of the vibrating body exceeds the critical value for Cooper-pair breaking [18]. As for vortex detection, in ^3He superfluids nuclear magnetic resonance (NMR) measurement provides a practical *noninvasive* method to count the number of vortex lines and to study their dynamics. In $^3\text{He-B}$ NMR

methods can be used from T_c down to about $0.2 T_c$. As the temperature decreases they become less sensitive to changes in counterflow and other control parameters. In this regime, the only measuring method developed to date for the study of vortices is to use vibrating wire resonators. These are used to create and detect quasiparticle excitations which in turn interact with the flow field of the vortices. In the zero-temperature regime of ballistic quasiparticle motion, measurements tracking deviations in the exponentially temperature-dependent equilibrium quasiparticle density [19], often in the presence of a quasiparticle beam [20], have turned out to be efficient tools for the study of vortices [21]. This technique can also be used for constructing dark matter detectors [22].

2. Hydrodynamics of rotating helium superfluids

2.1. Helium superfluids and vortex lines

Customarily $^4\text{He-II}$ is described with a wave function $\psi = |\psi_0|e^{i\varphi}$, where ψ_0 is the amplitude and φ the phase factor. The superfluid velocity is then defined as the gradient of the phase, $\mathbf{v}_s = (\kappa/2\pi)\nabla\varphi$ where $\kappa = 2\pi\hbar/m_4$. Since the curl of a gradient vanishes identically, $\nabla \times \mathbf{v}_s = 0$, the bulk superflow is irrotational. In principle rotational flow is thus excluded, but by forming quantized vortex lines the condensate can accommodate to rotating flow. In its simplest form a line vortex is a stable string-like object with a central hard core where the order parameter differs from its bulk form, thus forming a line singularity in the coherent order-parameter field. Since the condensate phase changes by $2\pi n$ around the core, where n is an integer number, the circulation of the superfluid velocity around the vortex core is quantized:

$$\oint d\mathbf{r} \cdot \mathbf{v}_s = n\kappa, \quad (1)$$

and κ plays the role of the circulation quantum. This persistent superfluid current around the core stores kinetic energy, providing the vortex with an energy per unit length, or line tension, which equals

$$\epsilon_v = \frac{1}{2} \rho_s \int_{r_c}^{r_v} dr (2\pi r) v_s^2 = \frac{\rho_s \kappa^2}{4\pi} n^2 \ln \left(\frac{r_v}{r_c} \right). \quad (2)$$

Here the upper (r_v) and lower (r_c) cutoffs are determined by the inter-vortex distance and the core size of the order of the superfluid coherence length ξ , respectively. Vortex lines with a singly-quantized structure $n = 1$ are thus energetically favourable. The superfluid hydrodynamics which follows from the introduction of the quantized vortex lines has been described in textbooks [23, 24].

The order parameter in superfluid ^3He relates to the wave function of the Cooper pairs, and has a complicated internal structure. Nevertheless, in $^3\text{He-B}$ it still contains an explicit phase variable φ . The above considerations remain valid with the exception that the circulation quantum is now given by $\kappa = 2\pi\hbar/(2m_3) = 0.066 \text{ mm}^2/\text{s}$, where $2m_3$ is the mass of the two ^3He atoms in the Cooper pair, rather than the single atom mass m_4 in the $^4\text{He-II}$ circulation quantum $\kappa = 0.099 \text{ mm}^2/\text{s}$. In what follows we use the

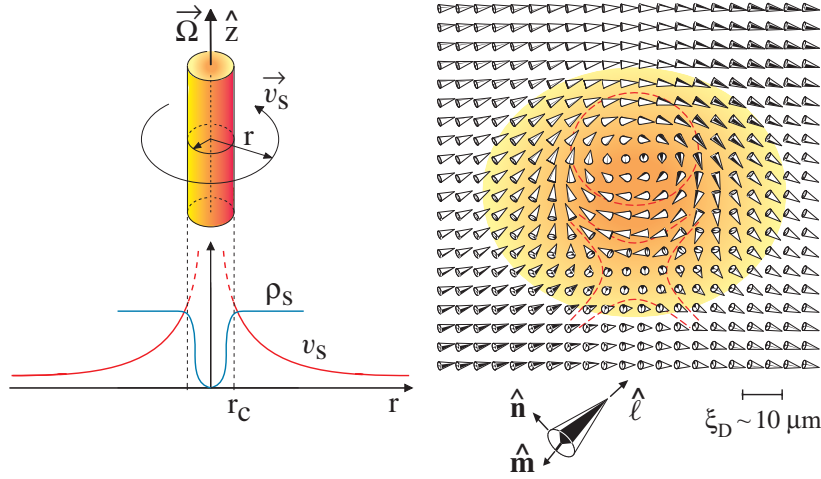


Figure 1. (Left) Macroscopic structure of quantized vortex line in He superfluids. The core radius r_c is on the order of the superfluid coherence length in $^4\text{He-II}$ ($\xi \sim 0.1 \text{ nm}$) and $^3\text{He-B}$ ($\xi \gtrsim 10 \text{ nm}$), but in $^3\text{He-A}$ the length scale is the healing length of the dipolar spin-orbit interaction ($\xi_D \gtrsim 10 \mu\text{m}$). (Right) Orbital order parameter texture of the soft core of the double-quantum vortex in $^3\text{He-A}$. The cones indicate the local direction and rotation of the orbital order parameter triad of unit vectors $\hat{\mathbf{l}}, \hat{\mathbf{m}}, \hat{\mathbf{n}}$. The topological winding number of the $\hat{\mathbf{l}}$ texture is $n = 2$. The texture is non-axisymmetric: it is composed of a circular half, or *meron*, and a hyperbolic meron, each with 2π circulation.

same symbol κ to denote the circulation quantum in both ^4He and ^3He , with appropriate values for each particular fluid. The superfluid order parameter does not vanish in the $^3\text{He-B}$ vortex core, but the order parameter state in the core is different from that in the bulk. Two different vortex-core structures are known to exist: an axisymmetric core at high temperatures and high pressures, and a non-axisymmetric at low temperatures [25, 26]. A first-order phase transition, which under equilibrium conditions occurs at $0.60 T_c$ at 29 bar pressure [25], separates these two core structures. At low pressures $P \lesssim 15 \text{ bar}$ only the nonaxisymmetric core exists. In both cases the core radius r_c is approximately equal to the coherence length $\xi \gtrsim 10 \text{ nm}$. An interesting curiosity to note is that this transition was the first phase transition ever observed within a defect, when it was discovered in 1981 [27]. A third vortex structure in bulk $^3\text{He-B}$ is the spin-mass vortex, a combination of a linear and a planar defect with both spin and mass flow currents around its core [28, 29, 3]. It will not be discussed in this review.

$^4\text{He-II}$ and $^3\text{He-B}$ are traditional Landau superfluids in that their superflow is potential, $\nabla \times \mathbf{v}_s = 0$, unless vortex line defects are present. In $^3\text{He-A}$, where the phase and the orbital structure (represented by the orbital vector $\hat{\mathbf{l}}$) of the order parameter are linked together, this condition is no longer strictly satisfied. Instead, the so-called Mermin-Ho relation holds [30]:

$$\nabla \times \mathbf{v}_s = \frac{\hbar}{4m_3} \epsilon_{ijk} \hat{l}_i (\nabla \hat{l}_j \times \nabla \hat{l}_k). \quad (3)$$

This implies that rotational superfluid flow can be accomplished via an inhomogeneous order-parameter texture $\hat{\mathbf{l}}(\mathbf{r})$. However, the energy cost of the necessary spatial variations, resulting from the rigidity of the order parameter, gives rise to a finite critical superflow velocity also in this system. At this velocity, vorticity with continuously winding structure of the order parameter orientation is formed so that in most cases no hard vortex core is involved. In the simplest form the structure of an isolated continuous vortex has the following spatial distribution of the orbital $\hat{\mathbf{l}}$ -field:

$$\hat{\mathbf{l}}(\rho, \phi) = \hat{\mathbf{z}} \cos \eta(\rho) + \hat{\boldsymbol{\rho}} \sin \eta(\rho) . \quad (4)$$

Here $\hat{\mathbf{z}}$, $\hat{\boldsymbol{\rho}}$ and $\hat{\boldsymbol{\phi}}$ are the unit vectors of the cylindrical coordinate system; $\eta(\rho)$ changes from $\eta(0) = 0$ to $\eta(\infty) = \pi$. This winding $\hat{\mathbf{l}}$ texture forms the so-called continuous soft core of the vortex [31], since it is in this region where the non-zero vorticity of superfluid velocity is concentrated:

$$\mathbf{v}_s(\rho, \phi) = \frac{\hbar}{2m_3\rho} [1 - \cos \eta(\rho)] \hat{\boldsymbol{\phi}} , \quad \nabla \times \mathbf{v}_s = \frac{\hbar}{2m} \sin \eta \left(\frac{\partial \eta}{\partial \rho} \right) \hat{\mathbf{z}} . \quad (5)$$

The circulation of the superfluid velocity around a contour enclosing the soft-core region is quantized, $\oint d\mathbf{r} \cdot \mathbf{v}_s = 2\kappa$, corresponding to the quantization number $n = 2$. Thus the object described by Eq. (4) is a continuous double-quantum vortex. By following the $\hat{\mathbf{l}}$ field across the cross section of the soft-core texture, it is noted that the $\hat{\mathbf{l}}$ vector goes through all possible orientations on the unit sphere. Such a topology of the vortex cross section in two spatial dimensions is known as a *skyrmion*.

In the magnetic field of the NMR measurements the continuous vortex is deformed and its structure is non-axisymmetric, see Fig. 1. However, its topology is robust to deformations, and the circulation remains the same: $\oint d\mathbf{r} \cdot \mathbf{v}_s = 2\kappa$. It is important to note that, since even in the soft-core region the order parameter retains its bulk structure, the core size of the continuous $^3\text{He-A}$ vortex is not set by the coherence length. Instead, the relevant length scale is the healing length corresponding to a weak spin-orbit coupling, $\xi_D \gtrsim 10 \mu\text{m}$, which is three order of magnitude larger.

Using the two halves of the skyrmion texture, the circular and hyperbolic *merons* (Fig. 1) as basic building blocks, other structures of continuous vorticity can be formed. An example are the various continuous periodic vortex textures in zero or low magnetic field [32, 33]. Another important structure is the vortex sheet [34, 35] which competes for living space with the double-quantum vortex line. A concise lexicon of these various structures can be found in Ref. [36].

The concept of the quantized vortex line dates back to Lars Onsager (1949) [37] and Richard Feynman (1955) [38] who found that the Landau irrotationality requirement $\nabla \times \mathbf{v}_s = 0$ has to be lifted at singular lines where $\nabla \times \mathbf{v}_s \neq 0$. In the case of $^3\text{He-A}$ these principles were put to a severe test which they finally survived when, in the context of the work of Mermin and Ho in 1976, Chechetkin (1976) [39] and Anderson and Toulouse (1977) [40] proposed the first example of a continuous vortex texture.

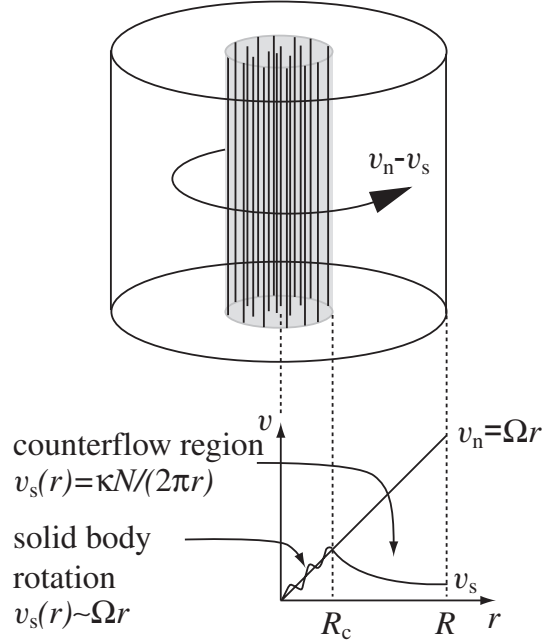


Figure 2. Schematic representation of a vortex cluster confined by the azimuthally circulating counterflow of the normal and superfluid components to the center of the rotating sample. The areal density of rectilinear singly-quantized vortex lines within the cluster is $2\Omega/\kappa$ and thus their number in a cluster of radius R_c is $N = \pi R_c^2 2\Omega/\kappa$.

2.2. Vortex states in rotating superfluid

The identification of the vortex structures of superfluid ^3He , and of the phase transitions separating these different structures, is based to a large extent on NMR measurements on a rotating sample. In rotation the vorticity $\nabla \times \mathbf{v}_s$ is aligned parallel to the rotation axis $\mathbf{\Omega}$ and generally forms a regular array over the cross section of the cylindrical sample. This is a particularly simple situation where both the structural and dynamic properties of these vortex structures can be analyzed.

The minimum energy configuration in rotation is the state with the equilibrium number of rectilinear vortex lines N_{eq} , which on average mimics solid-body rotation of the superfluid, *i.e.* $\langle \mathbf{v}_s \rangle = \mathbf{\Omega} \times \mathbf{r}$, or $\langle \nabla \times \mathbf{v}_s \rangle = 2\mathbf{\Omega}$. Since $\langle \nabla \times \mathbf{v}_s \rangle = n\kappa n_v$, the vortex density in the bulk is $n_v = 2\Omega/(n\kappa)$. The formation of a new vortex is associated with an energy barrier that has to be overcome before an elementary vortex loop can be nucleated. At sufficiently low applied flow velocities this is not possible, and metastable states with a vortex number N smaller than N_{eq} can be formed. These consist of a central vortex cluster with any number of vortex lines $0 < N \leq N_{\text{eq}}$. Within the cluster the rectilinear lines are packed to their equilibrium density $n_v = 2\Omega/(n\kappa)$, confined by the counterflow of the normal and superfluid components which circulates around the cluster with the velocity $\mathbf{v} = \mathbf{v}_n - \mathbf{v}_s = [\Omega r - n\kappa N/(2\pi r)] \hat{\phi}$. The first term is the velocity of the normal component, locked to co-rotation with the cylindrical container

(with radius R), while the second term arises from the combined persistent superflow of the N rectilinear vortex lines in the central cluster. An extreme case is the Landau state – the vortex-free state with $N = 0$ and $v_s = 0$ (as expressed in the rest frame of the laboratory). This is the state of maximum kinetic energy in the rotating frame. In many of the rotating experiments described below it is the initial state, the starting point for the measurements. Independently of N , the maximum counterflow velocity is at the cylindrical wall at $r = R$. This we call the velocity of the externally applied flow or the rotation drive of the cylindrical rotating container.

At constant rotation the stationary states are thus the equilibrium vortex state and the various metastable states with a depleted vortex cluster. In an ideal cylinder, which is exactly aligned parallel to the rotation axis, it is possible to have more than the equilibrium number of vortices N_{eq} , owing to a finite annihilation barrier [41]. Experimentally the exact value of N_{eq} is important for calibrating the measuring signals from a state with a well-defined configuration and number of vortices. Transient time-dependent rotating states are created in accelerating or decelerating rotation [42]. In Secs. 4 – 5 we describe measurements where rotation is kept constant and the dynamics evolves from vortex seed loops which have been introduced by external means into initially vortex-free counterflow.

2.3. Critical velocity of vortex formation

The first critical velocity of vortex formation in a rotating superfluid is that at which the free energy of the rectilinear vortex line becomes negative in the container frame. The corresponding angular velocity is known as the Feynman critical velocity, $\Omega_{\text{c1}} = \kappa/(2\pi R^2) \ln(R/r_c)$ [43]. It is analogous to the critical field H_{c1} for type II superconductors. For a rotating cylinder with a radius of a few mm, $\Omega_{\text{c1}} \sim 10^{-3}$ rad/s and is thus very small. However, although at $\Omega > \Omega_{\text{c1}}$ it becomes energetically favorable to introduce vortices in the rotating sample, some mechanism for their formation is required. A number of such mechanisms exist, due to sources both extrinsic and intrinsic to the superfluid itself, each with its characteristic critical velocity. For more discussion see Ref. [44]. Here we only summarize the basic ideas important for the overall picture.

In practice, in $^3\text{He-B}$ the lowest critical velocity Ω_c , which controls the formation of vortices, is found to depend on the shape and size of the container and the roughness of its surfaces. The simplest and most ideal case is a smooth-walled cylinder which is mounted with its symmetry axis as parallel to the rotation axis as possible. The surface quality is conditioned by the choice of material, the fabrication of the seams in the corners, and the cleanliness of the walls. Even residual gases, such as air or water, will condense on the wall during cool down, form small crystallites, and may determine Ω_c . In a good sample cylinder Ω_c is relatively high, of order 1 – 4 rad/s, so that large vortex-free counterflow can be achieved before the first vortex is formed. In the worst case extrinsic sources govern Ω_c . For instance, it can be determined by some pinning site, a piece of dirt, at which a remanent vortex may remain pinned indefinitely. If this

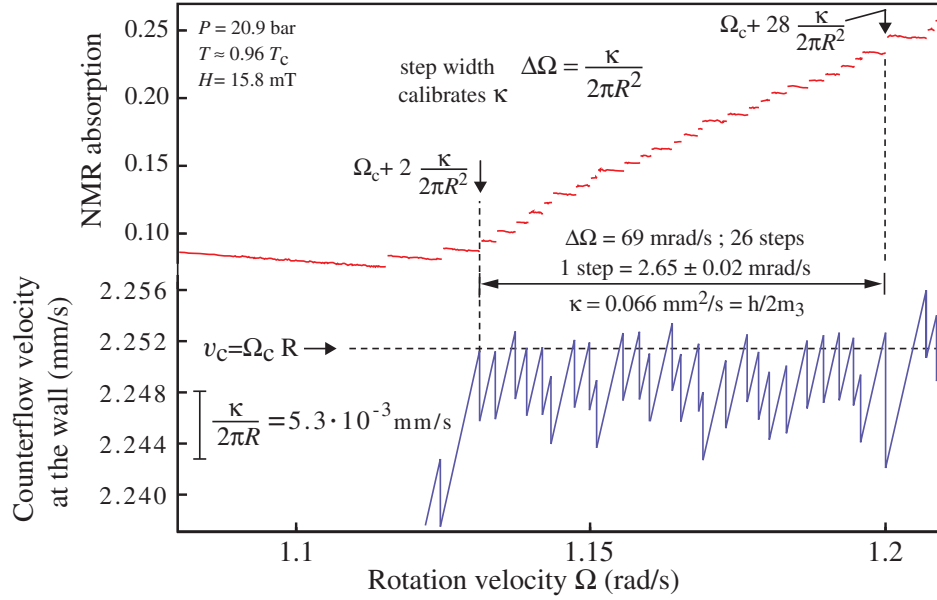


Figure 3. Measurement of single vortex formation as a function of the applied rotation velocity Ω at high temperatures in $^3\text{He-B}$ [45]. (*Top*) The vertical axis shows the NMR absorption in the Larmor region of the $^3\text{He-B}$ spectrum. Vortex formation starts with the first step-like increase, but the critical threshold at Ω_c is identified from the third step where the critical flow velocity in the bottom plot reaches a more stable value. (*Bottom*) Counterflow velocity at the cylinder wall $v = \Omega R - \kappa N/(2\pi R)$, where N is the number of steps already formed. The maximum possible value of counterflow for this sample container is defined by the horizontal dashed line, $v = v_c = \Omega_c R$.

site is occupied and Ω is increased to the critical value associated with the site, the pinned remanent loop will start to evolve.

In the most favorable case Ω_c arises from a combination of extrinsic and intrinsic reasons, if vortex formation takes place at a sharp surface asperity in the form of a pointed spike [45, 46]. At a very sharp spike the local velocity can exceed the average velocity at the wall by one to two orders in magnitude. Thus superfluidity will be broken first at this location when Ω is increased to Ω_c , and a small vortex loop is formed [47]. The loop then evolves to a rectilinear vortex line and reduces the counterflow velocity at the cylinder wall to a sub-critical value $v = \Omega_c R - \kappa/(2\pi R)$. If Ω is increased further by external means, vortex formation occurs recurrently at the same site every time when the counterflow reaches the critical value $v_c = \Omega_c R$. Here v_c is therefore the highest possible critical velocity for this container. An example of such vortex formation in single-quantum events as a function of Ω is illustrated by the staircase pattern in Fig. 3. This measurement has been performed in a container with $R = 2\text{ mm}$ [45]. A similar measurement with $^4\text{He-II}$ has been demonstrated only with flow through orifices of sub-micron size [7, 48].

An estimate of the intrinsic critical velocity, and of the energy barrier which inhibits the formation of an elementary vortex loop, can be obtained from the following simple

consideration [44]. The barrier is determined by the smallest possible vortex ring. Since the radius of such a ring cannot be smaller than the core radius (of the order of ξ), the energy of the smallest ring can be estimated from Eq. (2) as $E \sim \rho_s \kappa^2 \xi$. This gives $E/k_B T \sim (\xi/a)(T_F/T)$, where we have used $\rho_s \sim m/a^3$ for the superfluid density and $T_F = \hbar^2/2ma^2 k_B \sim 1 \text{ K}$ for the degeneracy temperature of the quantum Fermi liquid, with a as the interatomic distance. For $^3\text{He-B}$ we obtain $E/k_B T > 10^5$. This should be compared to a similar estimate $E/k_B T > 1$ for $^4\text{He-II}$, where the core size and the coherence length are $\xi \sim a$.

How to overcome such an energy barrier? The rate for thermal activation over the barrier is $\propto \exp(-E/k_B T)$, and thus the barrier is practically impenetrable by thermal activation or quantum tunneling at the appropriate temperatures for ^3He superfluids ($T \sim 1 \text{ mK}$) [44, 45]. Both mechanisms become effective only when the local velocity at the asperity reaches a value extremely close to the threshold where the energy barrier disappears, and the hydrodynamic instability of the flow occurs. This occurs at velocity of order $v_c \sim \kappa/\xi$. In $^3\text{He-B}$, this critical velocity for vortex formation is comparable to the Landau critical velocity for quasiparticle creation – the pair-breaking velocity $v_{pb} = \Delta/p_F \sim \kappa/\xi$, where Δ is the superfluid energy gap.

In contrast, in $^3\text{He-A}$ the smallest radius of a vortex loop and the core radius are determined by the characteristic length of orbital textures, which is typically of the dipolar length $\xi_D \gtrsim 10 \mu\text{m}$ and is several orders of magnitude larger than the coherence length ξ . Consequently, the critical velocity for A-phase vortex formation, $v_c \sim \kappa/\xi_D$, is considerably smaller [44] while the energy barrier is higher than in the B phase.

Therefore, in practical experimental conditions neither thermal activation or quantum tunneling are of importance. Instead, vortex formation takes place when the average counterflow velocity at the wall is increased to the point where the local velocity at the sharpest asperity reaches the critical value, the barrier vanishes, and the process thus becomes an instability. In principle, pair breaking and quasiparticle emission might occur already at a slightly lower velocity than when the barrier actually disappears, and this might finally trigger the hydrodynamic instability, which then results in vortex formation. The process might happen in the following manner: near the asperity the local velocity reaches the pair breaking value, the creation and emission of quasiparticles increases the density of the normal component, and as a result ρ_s decreases. Due to the conservation of current $\rho_s v_s$ the superfluid velocity then increases, enhancing the radiation of quasiparticles, which increases v_s further. The final result from the development of such a hydrodynamic instability will be vortex formation. However, whatever is the real mechanism of the instability generated by the flow in the vicinity of a protuberance, it limits the maximum counterflow velocity that can be achieved in a given sample container. With careful preparation of the surfaces, the critical velocity v_c has been raised up to about $0.1 - 0.4 v_{pb}$ in cylinders from fused quartz with $R \sim 3 \text{ mm}$.

The situation is quite different in $^4\text{He-II}$. Although the maximum possible superfluid velocity, the Landau value, is three orders of magnitude higher, the nucleation barrier height is $\sim 1 - 10 \text{ K}$ and comparable to the ambient temperature of $\sim 1 \text{ K}$. In the flow

through sub-micron-size orifices thermal activation has been found to be an important mechanism in vortex nucleation [49, 48] (at the lowest temperatures even quantum tunneling has been argued to exist [50, 51]). In contrast, in applications of bulk volume ^4He -II flow it is assumed that there always exist an abundance of remanent vortex loops pinned to walls [52] which start to expand in low applied flow.

In ^3He -B surface pinning is expected to be much less important than in ^4He -II because the vortex core radius is more than two orders of magnitude larger. In the best conditions in a clean quartz cylinder there are no *remanent* vortices and so far no clear evidence exists of pinning. However, *remnant* vortices of dynamic nature are observed. At low temperatures, where mutual friction dissipation becomes exponentially small, it may take hours for the last remnant vortex to annihilate at the container wall. If a remnant vortex loop happens to be around, it starts to evolve when flow is reapplied and may generate any number of new independent vortex loops. In fact, this situation is expected to prevail also in bulk ^4He -II over most of the experimentally accessible temperature range and thus even there no large source of pinned remanent vortices is needed to create large numbers of vortices and turbulent flow.

In ^3He -B we thus expect that the genuine intrinsic critical velocity is determined by the most effective instability, since the vortex formation barrier is impenetrable at all temperatures and velocities below a container specific critical value v_c . This feature has been utilized to study the different instabilities described in the later sections. The most usual case is vortex formation at constant temperature T and pressure P as a function of the externally applied flow $v_n - v_s$, as seen in Fig. 3. Here the criterion for vortex formation is the lowest critical velocity, in other words it is the vortex structure with the lowest v_c which is formed. If on the other hand one wants to establish the true equilibrium vortex structure, one has to slowly cool the sample at constant flow velocity below T_c . At T_c critical velocities vanish and the criterion for the selection becomes the lowest energy state. The equivalent of this procedure in superconductivity is known as field cooling.

Cooling under rotation has to be used in ^3He -A in order to stabilize and identify the single-quantum vortex (with $n = 1$) which at low velocities has a lower energy than the double-quantum vortex which, in turn, has a much lower critical velocity. Again, the large difference in critical velocities of these two vortex structures arises because of their different core structures. As distinct from the doubly quantized vortex, the singly quantized ^3He -A vortex has a hard vortex core with a radius comparable to the superfluid coherence length ξ (which lies hidden and embedded within the three orders of magnitude larger soft core of continuous structure [53]). As a result, its critical velocity $v_c \sim \kappa/\xi$ is close to the critical velocity of formation of the hard-core vortices in ^3He -B. The formation of the purely continuous texture of doubly-quantized ^3He -A vortex does not involve breaking the superfluid state anywhere but merely requires reorienting the degeneracy variables of the order parameter. That is why the corresponding critical velocity is much smaller, $v_c \sim \kappa/\xi_D$. These theoretical predictions have been tested in experiments in a rotating cylindrical container [54]. The measurements also indicated a

wide range of variation in the observed critical velocities of vortex formation, depending on the history of sample preparation. This variation was interpreted as resulting from the presence (or absence) of different types of planar defects, or solitons, in the A-phase order-parameter field [55]. Numerical calculations of flow instability for various different one-dimensional initial textures [56] provided semi-quantitative agreement with the measured variation.

The large difference between the critical velocities of formation of doubly quantized ^3He -A vortices and singly quantized vortices in ^3He -B allows us to create various different metastable states, when both phases are present in the rotating container.

2.4. Vortices and A-B interface in rotation

Having two ^3He superfluids which belong to the same order parameter manifold enables the construction of a unique situation which is not possible with other coherent quantum systems so far. With a profiled magnetic-field distribution it is possible to achieve the coexistence of ^3He -A and ^3He -B, and to stabilize an A-B phase boundary in the sample. What happens to such a superfluid two-phase sample in rotation? The substantial mismatch in the vortex properties of the two phases – their critical velocity, quantization of circulation, and vortex structure – raises the question how the vortices are going to behave at the A-B interface? In ^3He -A the critical velocity is low, while in ^3He -B it is an order of magnitude higher. This means that the A phase tends to be filled with essentially the equilibrium number of double-quantum vortex lines, while in the B phase there would at least initially be no vortices. Is such a situation stable, how is it going to evolve, and how are the single-quantum vortices of ^3He -B going to fit in this picture if they emerge later at higher velocities?

The left-hand side of Fig. 4 depicts the situation where the two-phase system is brought into rotation at constant temperature. When the rotation is started, A-phase double-quantum vortices are created at low critical velocity while no vortices are formed in the B phase. This expectation, confirmed by measurement [57], means that the A-phase vorticity is not able to cross the A-B interface and is accumulated on the A-phase side of the interface such that it coats the interface with a dense vortex layer. The layer is made up of a continuous texture of vorticity [58] and sustains the tangential discontinuity in the flow velocities of the superfluid fractions on the different sides of the A-B interface. Thus we have constructed a metastable state in which the two superfluids slide with respect to each other with a large shear-flow discontinuity, since the superfluid fraction in the A phase rotates solid-body-like while that in the B phase remains stationary in the inertial frame.

The minimum-energy state is shown on the right in Fig. 4. Here the vorticity is conserved on crossing the interface and both phases contain the equilibrium number of vortices at any given angular velocity of rotation. Accordingly, the number of double-quantum vortices in the A phase is one half of the number of singular singly-quantized B-phase vortices. On approaching the interface, the continuous A-phase vortex splits

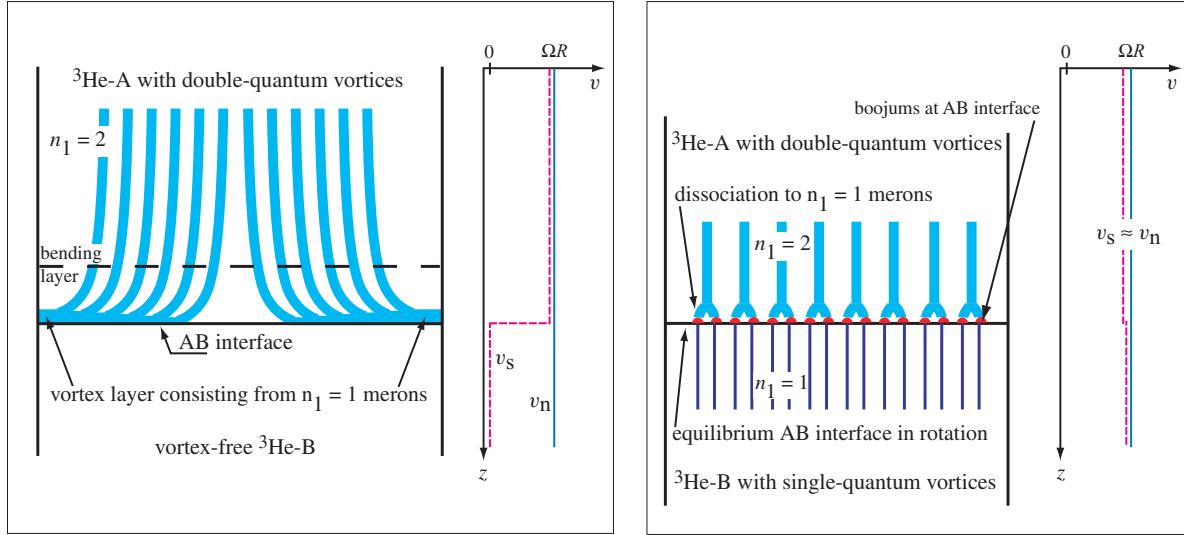


Figure 4. Sketches of the A-B interface in rotation. *Left:* In the A phase double-quantum vortex lines are formed at low rotation and we may assume it to be approximately in the equilibrium vortex state. At the A-B interface the double-quantum vortices curve over to the cylinder wall and cover the A-B interface as a vortex layer. This layer supports the discontinuity in the tangential velocities of the superfluid fractions at the A-B interface. The width of the A-B interface is on the order of the superfluid coherence length ξ while that of the vortex layer is three orders of magnitude larger, namely the dipolar healing length ξ_D . Thus in this metastable state below the critical velocity the continuous A-phase vorticity does not penetrate through the A-B interface, but gives rise to the unusual axial distribution in the flow velocities of the normal and superfluid components, $v_n(r) = \Omega r$ and $v_s(r)$, as shown on the right. *Right:* In equilibrium rotation, an A-phase double-quantum vortex with winding number $n = 2$, dissociates at the A-B interface into its 2π constituents, the circular and hyperbolic merons, each with $n = 1$. Each meron gives rise to a singular point defect, a boojum, on the A-B interface. The boojum is required as a termination point of a singular 2π ($n = 1$) B-phase vortex. Thus in the equilibrium state the continuous vorticity crosses the A-B interface, transforming to singular vorticity. However, neither point or line singularities are easily created in superfluid ^3He and therefore the vortex crossing takes place in a Kelvin-Helmholtz instability event.

into its two 2π constituents or merons. Each of the merons ends in a boojum on the A-B interface. The boojum is a point-like topological singularity at the A-B interface, the termination point of a singular B-phase vortex on the A-B interface. In practice singularities are not easily created in superfluid ^3He : like in the case of vortices the energy barrier is too high compared to ambient temperature (typically by 6 – 9 orders of magnitude). Therefore the equilibrium state is not obtained by increasing rotation at constant temperature and pressure [57]. Nor is it formed by cooling through T_c at constant rotation and pressure, which is the usual method to create the equilibrium state below a second-order phase transition. Here the first order A \rightarrow B transition also has to be traversed to form the A-B interface within the sample [59, 60]. The closest approximation to the equilibrium state is obtained by starting with the equilibrium

number of B-phase vortices in a single-phase sample at high rotation, with the barrier field at zero or at sufficiently low value. Next the barrier field is swept up (at constant Ω , T , and P), until A phase and the A-B interface is formed. In this case the equilibrium superfluid circulation is already trapped in the sample and cannot all escape. Finally, by reducing rotation to the point where vortices start to annihilate, one has reached the equilibrium vortex state. Because of the difficulties to nucleate point and line singularities, a different phenomenon occurs first while increasing the rotation of a two-phase sample. This is the superfluid Kelvin-Helmholtz instability, where the A-B interface becomes unstable in the presence of an excessively large discontinuity in the tangential superflow velocities (Sec. 3). A complex chain of events is released in which also vortices are tossed across the A-B interface from the A phase to the B-phase side.

2.5. Vortex dynamics and mutual friction

In $^3\text{He-B}$ and $^4\text{He-II}$, in the absence of vorticity, the superflow is potential and the superflow velocity $\mathbf{v}_s = \nabla\Phi$ is expressed in terms of the “flow potential” which is proportional to the phase of the superfluid wave function, $\Phi = (\kappa/2\pi)\varphi$. The superflow velocity \mathbf{v}_s obeys the Euler equation [61]:

$$\frac{\partial \mathbf{v}_s}{\partial t} + \nabla \tilde{\mu} = 0, \quad (6)$$

where $\tilde{\mu} = \mu + v_s^2/2$ and μ is the chemical potential. When quantized vortices (or continuous vorticity in $^3\text{He-A}$) are present, the superfluid velocity is no longer potential. The motion of a vortex leads to a phase-slip effect and modifies the r.h.s. of Eq. (6).

Vortex lines form a part of the superfluid component, but the normal component influences their movement through mutual friction which arises from the scattering of normal excitations from the vortex cores. In the zero-temperature limit, where the normal excitations vanish, the motion of a vortex line is governed by the Magnus force only, so that the vortex velocity coincides with the local superfluid velocity at the position of the vortex element. At non-zero temperatures the friction between the vortex and the normal component – the so-called mutual friction – causes a drag force on the vortex line and, as a result, the velocity $\mathbf{v}_L = d\mathbf{r}_L/dt$ of a vortex segment in the flow deviates from \mathbf{v}_s .

In the presence of vortices, the flow potential is not uniquely defined along the contours encircling the singular vortex lines. If the vortices do not overlap, the flow potential can be written as

$$\Phi = \sum_{\alpha=1}^N \Phi_{\alpha}(\mathbf{r} - \mathbf{r}_{\alpha}, t).$$

Here $\mathbf{r}_{\alpha}(s_{\alpha})$ are the coordinates of singular lines specified by a parameter s_{α} . If the positions of these lines also depend on time, $\mathbf{r}_{\alpha} = \mathbf{r}_{\alpha}(t)$, the time derivative of the superflow velocity becomes

$$\frac{\partial \mathbf{v}_s}{\partial t} = \frac{\partial}{\partial t} \nabla \Phi = \nabla \frac{\partial \Phi}{\partial t} - \sum_{\alpha} \left(\frac{\partial \mathbf{r}_{\alpha}}{\partial t} \nabla \right) \nabla \Phi_{\alpha}$$

$$= \nabla \left[\frac{\partial \Phi}{\partial t} - \sum_{\alpha} (\mathbf{v}_{\alpha} \cdot \nabla \Phi_{\alpha}) \right] + \sum_{\alpha} [\mathbf{v}_{\alpha} \times \boldsymbol{\omega}_{\alpha}]$$

Here $\partial/\partial t$ is the derivative only of the explicit t dependence of Φ and we put $\mathbf{v}_{\alpha} = \partial \mathbf{r}_{\alpha} / \partial t$. The vorticity of a single vortex is

$$\boldsymbol{\omega}_{\alpha} = \text{curl } \mathbf{v}_{s\alpha} = \text{curl } \nabla \Phi_{\alpha}$$

In $^3\text{He-B}$ and $^4\text{He-II}$ the vorticity from singular vortex lines is expressed as

$$\boldsymbol{\omega}_{\alpha} = \kappa_{\alpha} \int \delta(\mathbf{r} - \mathbf{r}_{\alpha}) d\mathbf{r}_{\alpha} \quad (7)$$

Here \mathbf{r}_{α} is the coordinate of the α -th vortex line and $\delta(\mathbf{r} - \mathbf{r}_{\alpha})$ is the three-dimensional δ -function, $d\mathbf{r}_{\alpha} = \hat{\mathbf{s}}_{\alpha} ds_{\alpha}$, $\hat{\mathbf{s}}_{\alpha}$ is the unit vector in the direction of the vortex line at the point \mathbf{r}_{α} , and ds_{α} is the arc length of the vortex line. The circulation of each vortex $\kappa_{\alpha} = n_{\alpha} \kappa$ may have n_{α} circulation quanta κ . For simplicity we consider here the case where all vortices are singly quantized, $n = 1$. Since the derivative

$$\frac{\partial \Phi}{\partial t} = \frac{\partial' \Phi}{\partial t} - \sum_{\alpha} (\mathbf{v}_{\alpha} \cdot \nabla \Phi_{\alpha})$$

is usually defined as the “superfluid chemical potential” $\mu_s = \partial \Phi / \partial t$ we have

$$\frac{\partial \mathbf{v}_s}{\partial t} + \nabla \tilde{\mu}_s = \sum_{\alpha} \mathbf{v}_{\alpha} \times \boldsymbol{\omega}_{\alpha} \quad (8)$$

Here $\tilde{\mu}_s = \tilde{\mu} - \mu_s$ is the renormalized chemical potential, which is the counterpart of the gauge-invariant scalar potential in the theory of nonstationary superconductivity [62].

The velocity of each vortex is determined up to its component perpendicular to the vortex line [24]:

$$\mathbf{v}_{\beta} = \hat{\mathbf{s}}_{\beta} \times (\mathbf{v}_s \times \hat{\mathbf{s}}_{\beta}) + \alpha \hat{\mathbf{s}}_{\beta} \times (\mathbf{v}_n - \mathbf{v}_s) - \alpha' \hat{\mathbf{s}}_{\beta} \times [\hat{\mathbf{s}}_{\beta} \times (\mathbf{v}_n - \mathbf{v}_s)] \quad (9)$$

Here $\alpha(T, P) > 0$ and $\alpha'(T, P) < 1$ are the temperature and pressure dependent dissipative and reactive mutual-friction parameters. As a result,

$$\frac{\partial \mathbf{v}_s}{\partial t} + \nabla \tilde{\mu}_s = \mathbf{v}_s \times \boldsymbol{\omega}_s + \mathbf{f}_{mf} \quad (10)$$

where

$$\boldsymbol{\omega}_s = \sum_{\beta} \boldsymbol{\omega}_{\beta} \quad (11)$$

is the total vorticity of the superfluid and \mathbf{f}_{mf} is the mutual-friction force [63]

$$\begin{aligned} \mathbf{f}_{mf} = & -\kappa \alpha \sum_{\beta} \int \delta(\mathbf{r} - \mathbf{r}_{\beta}) d\mathbf{r}_{\beta} \times [\hat{\mathbf{s}}_{\beta} \times (\mathbf{v}_n - \mathbf{v}_s)] \\ & + \alpha' [(\mathbf{v}_n - \mathbf{v}_s) \times \boldsymbol{\omega}_s] \end{aligned} \quad (12)$$

exerted by the normal component on a unit mass of superfluid via the vortex lines. The first term in \mathbf{f}_{mf} is the viscous component, with a negative projection on the relative velocity $\mathbf{v}_s - \mathbf{v}_n$,

$$\mathbf{f}_{mf} \cdot (\mathbf{v}_s - \mathbf{v}_n) = -(\mathbf{v}_s - \mathbf{v}_n)^2 \kappa \alpha \sum_{\beta} \int \delta(\mathbf{r} - \mathbf{r}_{\beta}) [1 - \cos^2 \gamma_{\beta}] ds_{\beta}. \quad (13)$$

Here γ_β is the angle between \mathbf{s}_β and $\mathbf{v}_s - \mathbf{v}_n$. Without the mutual friction force, Eq. (10) coincides with the Euler equation of the classical hydrodynamics of an ideal fluid

$$\frac{\partial \mathbf{v}}{\partial t} + \nabla \tilde{\mu} = \mathbf{v} \times \boldsymbol{\omega}. \quad (14)$$

For $^3\text{He-B}$, the mutual-friction parameters were calculated in Ref. [12, 13, 14] (for a theory review see [15]) and measured in Refs. [64, 65]. These parameters are discussed in terms of the chiral anomaly and the Callan-Harvey effect in relativistic quantum field theory in Ref. [5]. They both vanish at $T = 0$. With increasing temperature the dissipative mutual-friction parameter α increases so that above $0.6 T_c$ all dynamic processes are heavily overdamped in $^3\text{He-B}$. In $^3\text{He-A}$ α is expected to be in the overdamped regime at all currently accessible temperatures [13, 64, 66]. In contrast, in $^4\text{He-II}$ α is much smaller at all experimentally relevant temperatures, as seen in Fig. 5. The difference in the magnitudes of the mutual-friction parameters for superfluid ^3He and ^4He is so striking that the usual picture of $^4\text{He-II}$ vortices moving *with the superflow* fails for ^3He vortices which move *across the flow* in most of the accessible temperature range. In this respect, ^3He vortices resemble vortices in type-II superconductors which also perform viscous flow for most of the materials [15].

Since the equation of motion (9) for the trajectory of a vortex only depends on the two parameters α and α' , its solutions can be classified in terms of the dynamic parameter q defined as

$$q \equiv \frac{\alpha}{1 - \alpha'}. \quad (15)$$

This parameter has already been introduced in Section 1. According to both the theoretical predictions [14] and the experimental data for $^3\text{He-B}$ the parameter q depends exponentially on temperature in the low-temperature limit. The lower row of panels in Fig. 5 shows the inverse $q^{-1} = (1 - \alpha')/\alpha$ for $^3\text{He-B}$ and $^4\text{He-II}$. In superfluid dynamics q acquires an important function: it characterizes the relative influence of dissipation and plays the role of the Reynolds number (Sec. 4.3). A change in the characteristic solutions and a corresponding transition in the dynamics can be expected in the regime $q \sim 1$: this is located in the middle of the temperature range for $^3\text{He-B}$, but only a few μK below T_λ for $^4\text{He-II}$.

It is instructive to inspect some solutions of Eq. (9), as sketched in Fig. 6, for an ideal rotating cylinder where the rotation and cylinder axes coincide. We assume the experimentally important situation where the applied counterflow velocity dominates, *i.e.* we set in Eq. (9) $\mathbf{v}_n = \boldsymbol{\Omega} \times \mathbf{r}$ and $\mathbf{v}_s \approx 0$, and consider a large enough q so that the vortex dynamics is regular (instead of turbulent, see Sec. 4). The simplest case (a) is a rectilinear vortex line parallel to the rotation axis which is released in the flow from the cylinder wall. This might correspond to the situation in which a double-quantum vortex forms in $^3\text{He-A}$ when the cylinder is filled with a perfect global texture. In the cylindrically symmetric flow geometry the vortex will retain its rectilinear shape while it travels inward along a spiral which finally places the line in its equilibrium position along the axis of the cylinder. Another important case is (b) a vortex with a free end

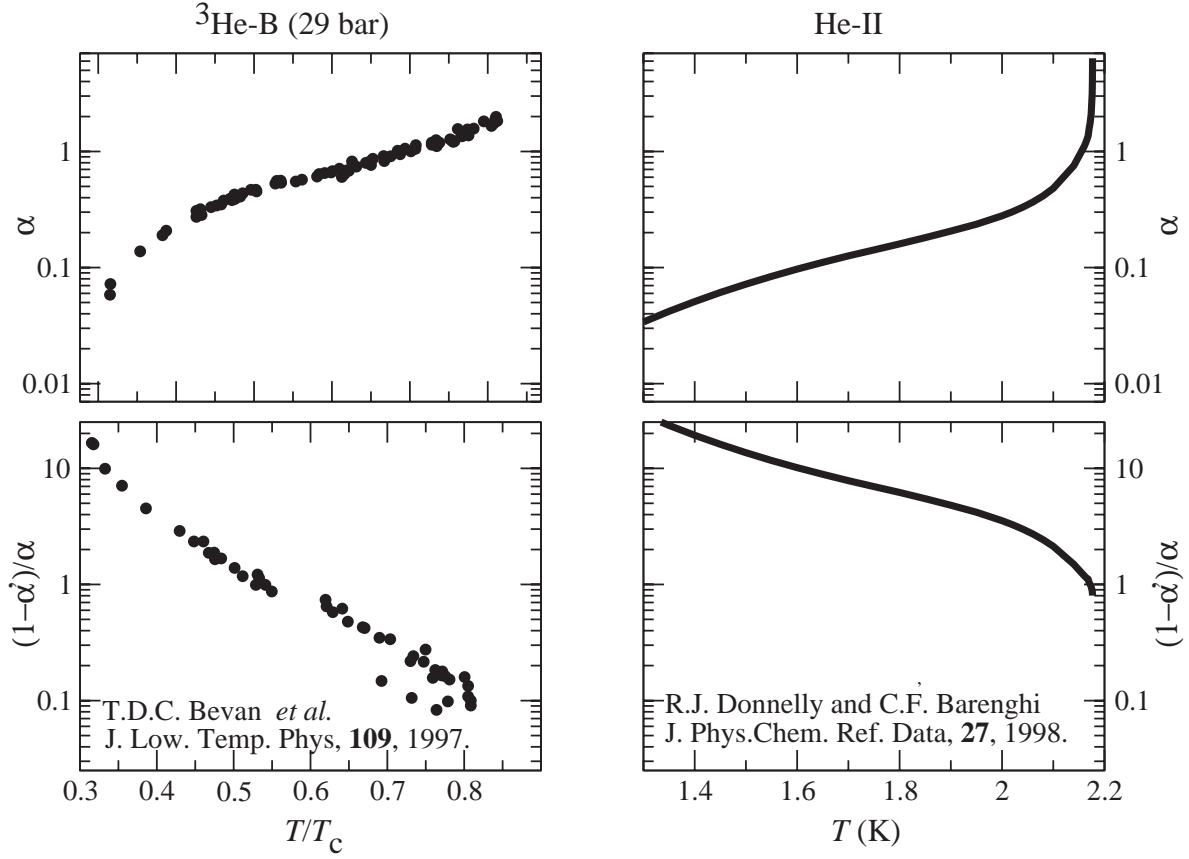


Figure 5. Mutual friction covers a different range of values in $^3\text{He-B}$ (left column of panels) and $^4\text{He-II}$ (right column). The top row of panels shows the dissipative mutual friction coefficient $\alpha(T)$ and the bottom row the dynamic parameter $q^{-1} = (1 - \alpha')/\alpha$. A transition in vortex dynamics is expected at $q \sim 1$. The data for $^3\text{He-B}$ is from Refs. [64, 65] and for $^4\text{He-II}$ from Ref. [67].

expanding in a long cylinder. The free end terminates perpendicular on the cylinder wall and describes a regular helix on the wall during its expanding motion. If we neglect the influence from its own curvature on the motion, then the curved section of the vortex remains within the same radial plane which rotates at the angular velocity $(1 - \alpha')\Omega$ around the cylinder axis, when viewed from the rotating frame. The trailing section of the vortex becomes aligned along the central axis and remains in rest there. An immediate extension of this example is case (d) where the vortex expands in a cylinder in the presence of a pre-existing central vortex cluster. The rectilinear trailing end of the vortex becomes now part of the vortex cluster and is incorporated as one of the vortices in the peripheral circle of lines. This section would prefer to be stationary in the rotating frame, it resides in a region of the sample cross section where the average counterflow velocity vanishes, and therefore it moves only with difficulty from one lattice site to the next in the outermost ring of vortex lines. The free end, on the other hand, expands along a spiral trajectory and leaves behind a helix which cannot relax instantaneously.

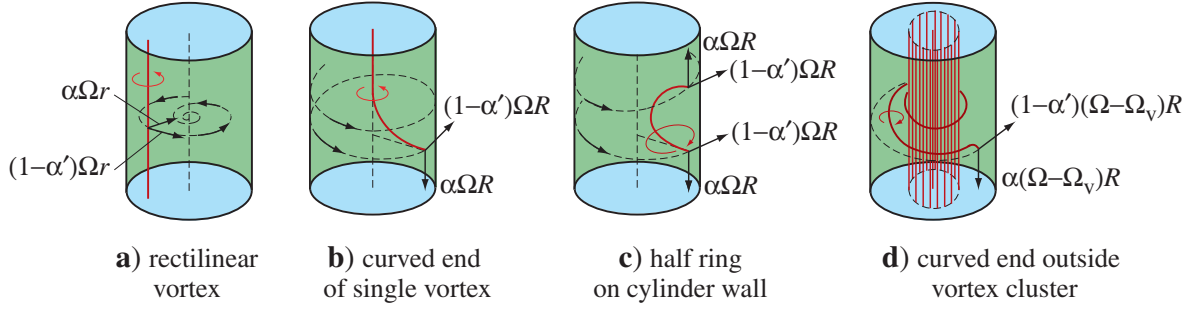


Figure 6. Sketches of vortex trajectories in an ideal rotating cylindrical superfluid sample, as viewed in the rotating frame. (a) A rectilinear vortex, which is released in the flow from the cylinder wall, travels along a spiral to its equilibrium location, to become aligned along the center axis of the cylinder. (b) In a long cylinder the propagating end of the vortex describes a spiral trajectory on the cylinder wall while it expands into the vortex-free section of the column. The trailing end is aligned along the central axis, the equilibrium location for the vortex. (c) An elementary vortex usually forms as a half ring on the cylinder wall. It expands both axially and radially. Assuming a half ring perpendicular to the azimuthally circulating applied flow and neglecting its self-induced velocity, the ring will remain during its expansion inside a radial plane which rotates around the cylinder axis with the angular velocity $(1 - \alpha')\Omega$ with respect to the cylinder walls. (d) If a central vortex cluster already exists in the cylinder (with $N = \pi R^2 2\Omega_v / \kappa$ rectilinear vortex lines), then the spiralling motion leaves behind a real helically wound vortex. At low temperatures, when the axial motion is slow, the helix becomes tightly wound and its loops are sufficiently aligned along the applied flow to suffer the Kelvin-wave instability.

To explore the hydrodynamic transition between regular and turbulent vortex dynamics at $q \sim 1$, we can ask the following question: how is the dynamic equation (10) modified for superfluids in the continuous limit, after averaging locally over vortex lines? This can be done even for tangled vortex states, if the lines are locally sufficiently parallel and their radius of curvature is much larger than the vortex core diameter. This would be the case, for instance, for rotating states with transient time-dependent disorder, since the rotating flow would rapidly polarize the component parallel to the rotation axis while the order in the transverse plane would be restored only later. In this case the averaging over nearby vortices on the r.h.s. of Eq. (10) gives

$$\frac{\partial \mathbf{v}_s}{\partial t} + \nabla \tilde{\mu} = \mathbf{v}_s \times \boldsymbol{\omega}_s - \alpha' (\mathbf{v}_s - \mathbf{v}_n) \times \boldsymbol{\omega}_s + \alpha \hat{\boldsymbol{\omega}}_s \times [\boldsymbol{\omega}_s \times (\mathbf{v}_s - \mathbf{v}_n)]. \quad (16)$$

This result is known as the coarse-grained hydrodynamic equation for the superflow velocity [68]. It will later be used to develop an analogue interpretation from the Navier-Stokes-based viscous hydrodynamics to superfluids [11].

2.6. Kelvin-wave instability of vortex lines

A quantized vortex can support helical Kelvin waves which become important in turbulent vortex dynamics. The Kelvin waves may lead to an instability which generally

develops at large flows. This instability can result in an increase in the number of individual vortex lines under an applied flow if the mutual friction is sufficiently small. It is the first step in the process by which more vortices can be generated from one or a few existing vortices so that bulk volume turbulence can switch on. The evolution towards the instability starts when a vortex becomes sufficiently aligned along the applied flow. A vortex line oriented parallel to the external flow is an unstable configuration, as demonstrated by Donnelly *et al.* by applying a thermal counterflow current parallel to rectilinear vortex lines in rotating $^4\text{He-II}$ [69]. Above a critical axial flow velocity rectilinear vortices became unstable and formed a turbulent tangle with varying axial polarization, depending on the axial counterflow velocity. The phenomenon was explained by Glaberson *et al.* [70, 71] in terms of the Kelvin-wave instability and was later reproduced also numerically by Tsubota *et al.* [72].

Consider small transverse deformations to an isolated vortex line, oriented along the z axis, in externally applied counterflow $\mathbf{v} = v \hat{\mathbf{z}}$ parallel to it. Parametrizing the position vector of an arbitrary element on the deformed vortex as

$$\mathbf{r}(z, t) = \zeta(z, t)\hat{\mathbf{x}} + \eta(z, t)\hat{\mathbf{y}} + z\hat{\mathbf{z}}, \quad (17)$$

we can write the unit tangent of the line as $\hat{\mathbf{s}}(z) \approx (\partial\zeta/\partial z)\hat{\mathbf{x}} + (\partial\eta/\partial z)\hat{\mathbf{y}} + \hat{\mathbf{z}}$ (to linear order in the small quantities ζ, η). The vortex curvature also gives rise to a self-induced contribution to the superfluid velocity at the vortex line. In the local approximation [24, 68]

$$\mathbf{v}_s^i = \tilde{\kappa} \frac{\partial \mathbf{r}}{\partial z} \times \frac{\partial^2 \mathbf{r}}{\partial z^2} \approx \tilde{\kappa} \left(-\frac{\partial^2 \eta}{\partial z^2} \hat{\mathbf{x}} + \frac{\partial^2 \zeta}{\partial z^2} \hat{\mathbf{y}} \right), \quad (18)$$

where $\tilde{\kappa} = (\kappa/4\pi) \ln(2\pi/k r_c)$. Inserting these to the equation of motion for the vortex line, Eq. (9), we find

$$\begin{aligned} \frac{\partial \zeta}{\partial t} &= -\tilde{\kappa} \frac{\partial^2 \eta}{\partial z^2} + \alpha \left(\tilde{\kappa} \frac{\partial^2 \zeta}{\partial z^2} + v \frac{\partial \eta}{\partial z} \right) + \alpha' \left(\tilde{\kappa} \frac{\partial^2 \eta}{\partial z^2} - v \frac{\partial \zeta}{\partial z} \right), \\ \frac{\partial \eta}{\partial t} &= \tilde{\kappa} \frac{\partial^2 \zeta}{\partial z^2} + \alpha \left(\tilde{\kappa} \frac{\partial^2 \eta}{\partial z^2} - v \frac{\partial \zeta}{\partial z} \right) - \alpha' \left(\tilde{\kappa} \frac{\partial^2 \zeta}{\partial z^2} + v \frac{\partial \eta}{\partial z} \right). \end{aligned} \quad (19)$$

The dispersion relation for wavelike disturbances $\propto \exp[-i(\omega t - kz)]$, *i.e.* Kelvin waves, can be found as

$$\omega = (1 - \alpha')\tilde{\kappa}k^2 - \alpha'kv - i\alpha(\tilde{\kappa}k^2 - kv). \quad (20)$$

With vanishing counterflow, $v = 0$, the dispersion relation simplifies to [73]

$$\omega = \tilde{\kappa}k^2(1 - \alpha' - i\alpha). \quad (21)$$

Here we again encounter the dynamic parameter $q = \alpha/(1 - \alpha')$ already introduced in Eq. (15) as the ratio of the imaginary and real parts of the dispersion [74]. The waves are always damped but at high temperatures, where $q > 1$, the waves are overdamped and do not propagate.

On the other hand, in the presence of externally applied flow the long-wavelength modes with $k < v/\tilde{\kappa}$ have $\text{Im}(\omega) > 0$, and exhibit exponential growth. In other words,

if an evolving vortex configuration at some time has long enough vortex-line sections oriented parallel to external flow, these will become unstable to exponentially growing helical deformations. Furthermore, if q is small enough, such expanding waves can then undergo reconnections, either with the walls of the container or with other vortex lines. This leads to a growing number and density of vortices and, ultimately, to the onset of turbulence, as discussed in Sec. 4.6.

3. Kelvin-Helmholtz instability in superfluids

3.1. Introduction

The Kelvin-Helmholtz shear flow instability is a well-known phenomenon of classical hydrodynamics which was first discussed by Lord Kelvin already in the 1860's. It occurs at the interface between two fluid layers which are in relative motion with respect to each other. For instance, at low differential flow velocity the interface between two stratified layers of different salinity or temperature is smooth in the ocean, but at some critical velocity waves are formed on the interface. Similarly, ripples do not form on the water surface on a lake at infinitesimal wind velocities, but at some finite critical value. The Kelvin-Helmholtz instability is thus a common phenomenon in nature around us. The condition for instability is derived in many textbooks on hydrodynamics [75, 76] in the limit of inviscid and incompressible fluids. In superfluids it was first observed for the A-B interface in rotation [57].

The A-B interface instability occurs between the two ^3He superfluids, $^3\text{He-A}$ and $^3\text{He-B}$, when the superfluid fractions in the two phases move with different velocities along the A-B interface (Fig. 4 *left*). This initial state is dissipationless while the state after the instability is not, as surface waves or ripplons form on the interface and their motion is highly damped. In conventional liquids and gases the mathematical description of the interfacial instability is inevitably only approximate: if viscosity is neglected, the initial non-dissipative states of the two liquid or gas layers sliding with respect to each other are not exact. The question then arises not only about the true value of the critical velocity, but more generally about the existence and nature of the instability. Superfluids are the only laboratory examples of cases where viscosity is totally absent, and the mathematical description of the instability can be presented analytically in a simple form. The initial state of the A-B interface with different tangential superflow velocities across the interface is in nondissipative thermodynamic equilibrium, until the threshold critical velocity of the hydrodynamic instability is reached. As a result – contrary to viscous normal fluids – the instability threshold is well defined. Experimentally it is manifested by the sudden formation of vortices in the initially vortex-free $^3\text{He-B}$ phase (Fig. 4 *right*) at a rotation velocity at which no vortices would yet be formed without the presence of the A-B interface.

3.2. Experimental setup

The Kelvin-Helmholtz experiments reported in Ref. [57] were conducted in a rotating nuclear demagnetization cryostat in which the liquid ^3He sample can be cooled below $0.3 T_c$ in rotation up to 4 rad/s. A schematic illustration of the sample setup is shown in Fig. 7. The sample is contained in a fused quartz tube of $R = 3$ mm radius. An aperture of $0.5 - 0.75$ mm diameter in the bottom end plate restricts the flow of vortices into the sample from the heat exchanger volume below. The quality of the sample-tube surface is of great importance. Surface defects serve as nucleation and pinning sites and are most detrimental to the measurements. Before use the container is treated with a HF solution, to etch away sharp protuberances, and then cleaned with solvents. The same quartz tube may display sizable variation in critical velocity and vortex formation properties depending on how it is cleaned between experiments, indicating that dust particles, dirt, frozen gas, etc. serve as nucleation and pinning sites. Most measurements were performed using a sample tube which allowed vortex-free rotation up to the maximum rotation velocity of the cryostat.

Two independent continuous-wave NMR spectrometers are used for monitoring the sample. Their detector coils are located close to both ends of the sample volume. Three separate superconducting solenoidal magnets, all with their fields oriented along the rotation axis, are needed in the experiment. Two magnets are required for the homogenous NMR fields and one as a "barrier magnet" around the central section of the tube for stabilizing $^3\text{He-A}$. The barrier magnet provides fields up to 0.6 T which is sufficient to stabilize the A phase at all temperatures and pressures. In the inhomogeneous barrier field $H(z)$ the equilibrium position z_0 of the A-B interface is determined by the equation $H(z_0) = H_{AB}(T)$, where $H_{AB}(T)$ is the first-order phase transition line between the A and B phases in the (H, T) plane (Fig. 8 *left*).

Various configurations of A and B phases can be stabilized and trapped in the sample tube. (i) At zero or low barrier fields the B phase might occupy the whole sample volume. In this *all-B configuration* the two spectrometers probe the same volume. The time difference between the two NMR readings can then be used to study the propagation of vortices along the column. (ii) At barrier fields above $H_{AB}(T, P)$, the equilibrium transition field between the A and B phases, the A phase is stabilized in the center of the barrier magnet. In this *BAB configuration* the top and bottom sections of the sample are disconnected: vortex lines generated in one of the B-phase sections do not pass to the other across the A phase region. (iii) At pressures above 21 bar, $^3\text{He-A}$ is stable also at zero magnetic field from T_c down to $T_{AB}(P)$. At high temperatures the entire sample volume is then filled with A phase (*all-A configuration*). When the temperature is lowered somewhat below the equilibrium $A \rightarrow B$ transition, B phase nucleates in the heat-exchanger volume and expands into the lower section of the sample (at about $0.75 T_c$). If the barrier field is sufficiently high to stabilize the A phase, the advancement of the B phase is stopped by the stable A phase and an A-B interface is formed. Since the A phase in the top section can supercool quite substantially [77],

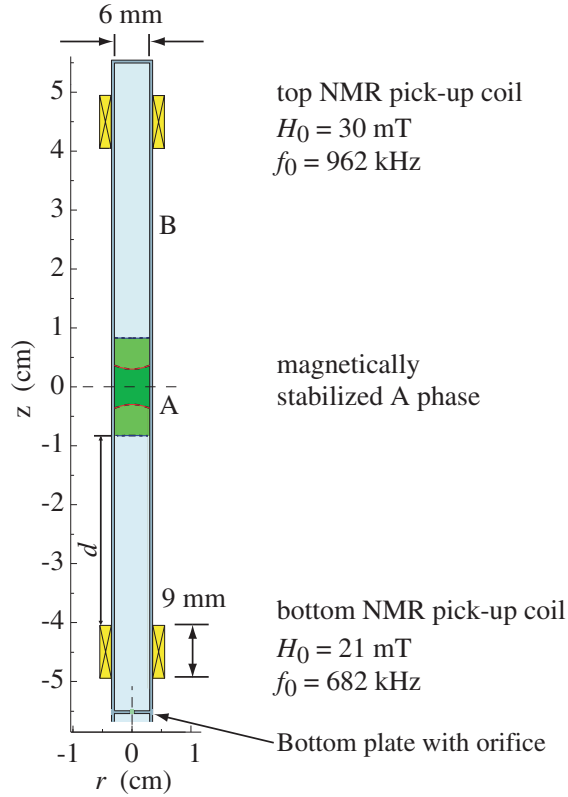


Figure 7. Two-phase superfluid ^3He sample for measurements on the Kelvin-Helmholtz instability. The sample volume is 6 mm in diameter and 11 cm long. A small orifice of 0.5 – 0.75 mm in diameter in the center of the bottom end plate separates the sample from the rest of the liquid ^3He volume. The ^3He below the orifice is needed to establish thermal contact to the refrigerator. NMR pick-up coils are located at both ends of the sample tube. They are circular coils with their symmetry axis transverse to the tube axis. Two solenoidal superconducting magnets provide the homogenous axially oriented polarizing fields for NMR. A third barrier magnet creates the field to stabilize ^3He -A in the center section of the long sample. Two examples of the A phase region (shaded) are shown at $0.55 T_c$: at the current of $I_b = 8$ A in the barrier solenoid the A phase extends further in the column and the two A-B boundaries are almost flat, while at $I_b = 4$ A the A phase region is short and the A-B boundaries are concave.

the sample remains in the *BA configuration*. Thus the barrier field isolates the top from an $A \rightarrow B$ transition in the lower section. Eventually, at a low enough temperature, B phase also forms independently at the top. Since the ultimate supercooling of ^3He -A depends on the surface properties, the $A \rightarrow B$ transition also serves as a measure of the quality of the quartz walls. At best the top was supercooled to $0.52 T_c$ at 29 bar (when the equilibrium transition is at $T_{AB} = 0.85 T_c$). The BA configuration was most important in the early stages of measurements on the A-B interface instability, since the top spectrometer is then recording the vortex number in the A phase and the bottom spectrometer in the B phase. To understand what happens in the two-phase sample when rotation is started, and to correlate in real time the events on both sides of the

A-B interface, simultaneous recordings of vortex numbers in both phases are needed.

It turned out that in rotation ^3He -A is in solid-body-like rotational flow, practically locked to co-rotation with the container, owing to the low critical velocity of vortex formation. In contrast, in ^3He -B the superfluid component is in the vortex-free Landau state and stationary in the laboratory frame. This non-dissipative initial state becomes possible through the formation of an A-phase vortex layer which covers the A-B interface and provides the discontinuity in the tangential flow velocities (Fig. 4 *left*). The tangential discontinuity is ideal – there is no viscosity in the motion of the two superfluids so that this state can persist for ever, until at some critical threshold velocity the Kelvin-Helmholtz instability occurs and some vortices penetrate across the A-B interface into the vortex-free B phase (Fig. 4 *right*).

3.3. Kelvin-Helmholtz instability in classical hydrodynamics

The Kelvin–Helmholtz (KH) instability is one of the many interfacial instabilities in the hydrodynamics of liquids, gases, charged plasma, and even granular materials. It refers to the dynamic instability of an interface with discontinuous tangential flow velocities and can loosely be defined as the instability of a vortex sheet. Many natural phenomena have been attributed to this instability. The most familiar ones are the generation of capillary waves on the surface of water, first analyzed by Lord Kelvin [78], and the flapping of sails and flags, first discussed by Lord Rayleigh [79].

Many of the leading ideas in the theory of interfacial instabilities in hydrodynamics were originally inspired by considerations about ideal inviscid flow. The corrugation instability of the interface between two ideal liquids, with different mass densities ρ_1 and ρ_2 , occurs in the gravitational field at the critical differential flow velocity [78]

$$(\mathbf{U}_1 - \mathbf{U}_2)^4 = 4\sigma g \frac{(\rho_1 - \rho_2)(\rho_1 + \rho_2)^2}{\rho_1^2 \rho_2^2} , \quad (22)$$

where σ is the surface tension of the interface, and g is the gravitational acceleration. To separate the gravitational and inertial properties of the liquids, we rewrite the threshold velocity in the form

$$\frac{\rho_1 \rho_2}{\rho_1 + \rho_2} (\mathbf{U}_1 - \mathbf{U}_2)^2 = 2\sqrt{\sigma F} . \quad (23)$$

Here F is the external field stabilizing the position of the interface, which in the case of a gravitational field is

$$F = g(\rho_1 - \rho_2) , \quad (24)$$

but can in general originate from some other source. The surface mode of ripples, or capillary waves, which is first excited has the wave number corresponding to the inverse ‘capillary length’

$$k_0 = \sqrt{F/\sigma} . \quad (25)$$

However, ordinary fluids are not ideal and the correspondence between this theory and experiment is not satisfactory. One reason for this is that the initial state cannot

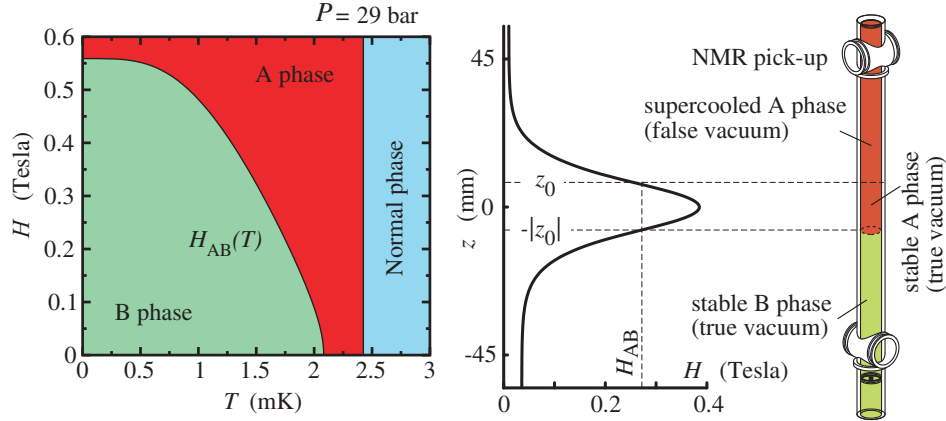


Figure 8. Magnetic stabilization of $^3\text{He-A}$ in the experimental setup of Fig. 7 [57]. (Right) Sample container and the axially oriented magnetic field distribution along the sample in the BA configuration (with a barrier-magnet current $I_b = 4.0\text{ A}$). The barrier field maintains the A phase in stable state in the middle section of the sample where $H(z) > H_{AB}(T)$. In the top, where $H(z) < H_{AB}(T)$, the A phase persists in meta-stable state. Thus only one A-B interface exists at the lower location $z = -|z_0|$, where $H(z_0) = H_{AB}(T)$. When the temperature T or the current I_b is varied, the axial location $z_0(T, I_b)$ of the A-B interface is changed and also the field gradient dH/dz in which the interface resides. The restoring force acting on the A-B interface in Eq. (26) depends on the field gradient dH/dz and therefore on the axial field profile of the barrier magnet. (Left) Magnetic phase diagram in the (H, T) plane where $H_{AB}(T)$ marks the first-order phase transition line between the A and B phases (at constant pressure $P = 29.0\text{ bar}$). The upper plane at $z_0(T, I_b)$ separates the section in the middle, where $^3\text{He-A}$ is the true vacuum state, from the section in the top, where $^3\text{He-A}$ is the false vacuum. The false vacuum persists down to a container dependent minimum temperature.

be properly prepared – the shear-flow discontinuity is never an equilibrium state in a viscous fluid, since it is not a solution of the Navier-Stokes equation. Like with idealized models in the zero-temperature limit in general, it is not apparent whether the notion of ‘instability’ can be properly extended from the inviscid case to finite viscosities [80].

In superfluids the criterion for the instability can be formulated in the absence of viscosity, and the tangential discontinuity at the interface between $^3\text{He-A}$ and $^3\text{He-B}$ is a stable state. These two superfluid phases have different magnetic properties and their interface is stabilized by the gradient in the applied magnetic field $H(z)$ (Fig. 8). In the region where $H(z) > H_{AB}(T)$ the A-phase has lower magnetic energy, while in the neighboring region $H(z) < H_{AB}(T)$ the B-phase is favored. In this case the gradient in the magnetic energy densities of the two liquids provides the restoring force F in Eq. (24):

$$F = \frac{1}{2} \frac{d}{dz} [(\chi_A - \chi_B)H^2] . \quad (26)$$

Here $\chi_A > \chi_B$ are the magnetic susceptibilities of the A and B phases, respectively. One might expect that by substituting this interfacial restoring force F into Eq. (23), and

using the superfluid densities of the A and B phases instead of the total density, the critical velocity for the KH instability of the A-B interface could be obtained. However, it turns out that a proper extension of the KH instability to superfluids incorporates the criterion in Eq. (23) only as a particular limiting case, while in general the physics of the instability is rather different from the ideal inviscid model. A different but well-determined criterion is obtained for the instability condition in terms of the velocities and densities of the superfluid fractions.

3.4. Modification of Kelvin-Helmholtz instability in superfluids

The criterion for the KH instability of ideal fluids in Eq. (23) depends only on the relative velocity across the interface. In practice there always exists a preferred reference frame imposed by the environment. In the superfluid case this is the frame fixed to the container. At $T \neq 0$ the normal component provides the coupling to the reference frame: in the state of thermodynamic equilibrium the normal component moves together with the container walls, *i.e.* $\mathbf{v}_n = 0$ in the frame of the container. Owing to this interaction of the A-B interface with its environment the measured instability occurs at a lower differential flow velocity, before the classical criterion in Eq. (23) is reached. Moreover, it even occurs in the case when the two superfluids move with the same velocity. However, this does not imply that the renormalized instability criterion would depend on the interaction with the normal component – in fact, it is still determined only by thermodynamics. Waves are formed on the interface when the free energy of a corrugation becomes negative in the reference frame of the environment and the A-B interface becomes thermodynamically unstable, *i.e.* when it becomes possible to reduce the energy via the normal component and its interaction with walls. The instability condition Eq. (23) of the ideal inviscid fluid is restored if the interaction with the environment is not effective. This would occur, for example, during rapid rotational acceleration at very low temperatures when the instability caused by the interaction with the environment does not have enough time to develop.

The free energy of the disturbed A-B interface $\zeta(x, y)$ in the reference frame of the container contains the surface tension energy, which corresponds to the potential energy in the ‘gravity’ field, and the kinetic energy of the two liquids [81]:

$$\mathcal{F}\{\zeta\} = \frac{1}{2} \int dx dy \left[F\zeta^2 + \sigma(\nabla\zeta)^2 + \int_{-h_B}^{\zeta} dz \rho_{sB} \mathbf{v}_{sB}^2 + \int_{\zeta}^{h_A} dz \rho_{sA} \mathbf{v}_{sA}^2 \right]. \quad (27)$$

Here we take into account that in thermal equilibrium the normal component is at rest in the container frame, $\mathbf{v}_{nA} = \mathbf{v}_{nB} = 0$, and only the superflow contributes to the kinetic energy. The heights of the A and B phase layers are denoted with h_A and h_B . For simplicity we ignore the anisotropy in A phase and approximate the superfluid-density tensor with a scalar. We write the superfluid velocities as $\mathbf{v}_{sB}(\mathbf{r}) = \mathbf{U}_B + \delta\mathbf{v}_{sB}(\mathbf{r})$ and $\mathbf{v}_{sA}(\mathbf{r}) = \mathbf{U}_A + \delta\mathbf{v}_{sA}(\mathbf{r})$, where \mathbf{U}_B and \mathbf{U}_A are the velocities at an undisturbed flat interface. Using $\nabla \times \mathbf{v}_s = \nabla \cdot \mathbf{v}_s = 0$, and the boundary conditions at the interface,

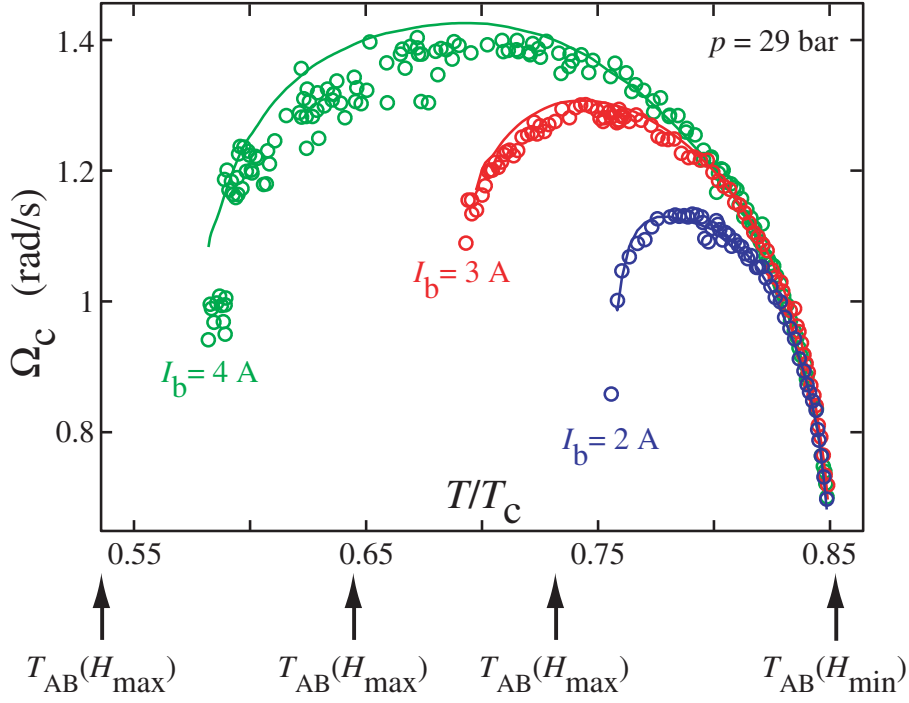


Figure 9. A-B interface instability as a function of temperature. The measured critical velocity $\Omega_c = U_B/R$ is plotted at three different fixed currents I_b in the barrier magnet [57]. When T is changed at constant I_b , the equilibrium position z_0 of the interface in the field gradient dH/dz of the barrier magnet changes. This causes a change in the restoring force in Eq. (26). Therefore the critical velocity of the instability tends to zero when z_0 approaches either the minimum (at high temperatures) or maximum (at low temperatures) value of the barrier field and $dH/dz \rightarrow 0$ (see Fig. 8). The temperatures at which $dH/dz \rightarrow 0$ are marked with vertical arrows below the figure. The solid curves represent the instability criterion in Eq. (30), when $U_B = \Omega R$ and $U_A = v_{nA} = v_{nB} = 0$. No fitting parameters are used.

$\hat{\mathbf{s}} \cdot \mathbf{v}_{sA} = \hat{\mathbf{s}} \cdot \mathbf{v}_{sB} = 0$, one obtains the free energy of a surface mode as (for details see Ref. [82] where also the anisotropy of the tensor ρ_{sA}^{ij} is taken into account)

$$\mathcal{F}(\zeta_k) \propto a^2 [F + k^2 \sigma - k (\rho_A^{\text{eff}} U_A^2 + \rho_B^{\text{eff}} U_B^2)] . \quad (28)$$

Here k is the wave vector along x for a surface corrugation amplitude of the form $\zeta(x) = a \sin kx$, and

$$\rho_A^{\text{eff}} = \frac{\rho_{sA}}{\tanh(kh_A)} , \quad \rho_B^{\text{eff}} = \frac{\rho_{sB}}{\tanh(kh_B)} . \quad (29)$$

In the relevant experimental conditions we are always in the ‘deep water’ limit, $kh_A \gg 1$, $kh_B \gg 1$. The free energy becomes negative for the first time for the critical ripplon wave number $k_0 = (F/\sigma)^{1/2}$ when

$$\frac{1}{2} (\rho_{sB} U_B^2 + \rho_{sA} U_A^2) = \sqrt{\sigma F} . \quad (30)$$

A comparison of Eq. (30) to the measured critical rotation velocity Ω_c of the first KH instability event is shown in Fig. 9. The curves have not been fitted; they have been

drawn using accepted values from the literature for the various quantities (for details see Ref. [57]). Such a remarkable agreement for a complicated phenomenon can only be achieved in superfluid ^3He !

We thus conclude that, even under perfectly inviscid conditions, in superfluids the critical velocity for the KH instability is not given by the classical result for ideal fluids. The new criterion for the instability in Eq. (30) has at first glance paradoxical consequences. The instability is not determined by the relative velocity $\mathbf{v}_{sA} - \mathbf{v}_{sB}$; in fact, the instability would occur even if the two superfluid velocities were equal. The instability would also occur for only a single superfluid with a free surface. These new features arise from the two-fluid nature of the superfluid. Therefore, the instability threshold is determined by the velocities $\mathbf{v}_{si} - \mathbf{v}_n$ of each superfluid i with respect to the reference frame of the walls and thus with respect to the normal fractions which in thermodynamic equilibrium move together with the walls. Accordingly, the free surface of a superfluid – the interface between the superfluid and the vacuum – becomes unstable when the superfluid velocity exceeds the critical value in the reference frame of the normal fraction [8, 9]. With many (i) superfluid fractions in the same liquid, such as the neutron and proton superfluids in a neutron star [83], the threshold is determined by some combination of the superfluid velocities $\mathbf{v}_{si} - \mathbf{v}_n$ [10].

3.5. Kelvin-Helmholtz instability in the low-temperature limit

On approaching the zero-temperature limit the density of normal excitations rarefies, the coupling with the container walls becomes weaker, and the superfluid density becomes the total density: $\rho_{sA} \rightarrow \rho_A$ and $\rho_{sB} \rightarrow \rho_B$. How is the superfluid going to react to the environment under these conditions? Let us compare the result in Eq. (30) with the ideal classical condition in Eq. (23) in the limit when $T \rightarrow 0$. The classical instability condition reads

$$\frac{\rho_A \rho_B}{\rho_A + \rho_B} (\mathbf{U}_B - \mathbf{U}_A)^2 = 2\sqrt{\sigma F}, \quad (31)$$

while the superfluid instability occurs when

$$\frac{1}{2} (\rho_A U_A^2 + \rho_B U_B^2) = \sqrt{\sigma F}. \quad (32)$$

In the experiment the A-phase superfluid component is approximately stationary in the container frame, $U_A \approx 0$, and the densities of the two liquids are practically equal, $\rho_A \approx \rho_B = \rho$. Then the B-phase critical velocity at the instability is $U_B^2 = 4\sqrt{\sigma F}/\rho$ according to the classical criterion, while from Eq. (30) we obtain a result which is smaller by a factor of $\sqrt{2}$, *i.e.* $U_B^2 = 2\sqrt{\sigma F}/\rho$.

The difference is imposed by the interaction with the environment [5]. To understand this, we repeat the derivation of the classical KH instability [84] with one important modification. We add to the equation of motion of the A-B interface a friction force which arises when the interface moves with respect to the environment, *i.e.* with

respect to the normal component. In the reference frame of the container it has the form

$$F_{\text{friction}} = -\Gamma \partial_t \zeta . \quad (33)$$

In the low- T limit, the friction between the A-B interface and the normal component arises from the Andreev scattering of ballistic quasiparticles from the interface. In this regime the parameter $\Gamma \propto T^3$ [85, 86, 87]. For simplicity, we choose a situation when both fluids move along the x direction, and consider surface waves (ripplons) of the form $\zeta(x, t) = a \sin(kx - \omega t)$ in the container frame. The classical dispersion relation for ripplon motion is then modified by the presence of the friction term to

$$\rho_A \left(\frac{\omega}{k} - U_A \right)^2 + \rho_B \left(\frac{\omega}{k} - U_B \right)^2 = \frac{F + k^2 \sigma}{k} - i\Gamma \frac{\omega}{k} , \quad (34)$$

modifying the nature of the instability. We rewrite the above equation as follows:

$$\begin{aligned} \frac{\omega}{k} &= \frac{\rho_A U_A + \rho_B U_B}{\rho_A + \rho_B} \\ &\pm \frac{1}{\sqrt{\rho_A + \rho_B}} \sqrt{\frac{F + k^2 \sigma}{k} - i\Gamma \frac{\omega}{k} - \frac{\rho_A \rho_B}{\rho_A + \rho_B} (U_A - U_B)^2} . \end{aligned} \quad (35)$$

If $\Gamma = 0$, this reduces to the classical dispersion relation and the instability occurs when the expression under the square root becomes negative. The ripplon spectrum then acquires an imaginary part with both plus and minus signs. Thus at the threshold velocity of Eq. (31) the perturbation grows exponentially in time. A sketch of the imaginary and real parts of the frequency of the critical ripplon mode (with $k = k_0$) is shown in Fig. 10.

In the case of the superfluid instability we have to consider the influence of the term with the friction parameter Γ in Eq. 35. When the imaginary part $\text{Im } \omega(k)$ crosses zero as a function of U_B , the attenuation of the ripplon modes is transformed to amplification. This occurs first for ripplons with the wave vector given by Eq. (25). While the instability condition Eq. (32) does not depend on the friction parameter Γ , the slope of the imaginary part is proportional to Γ . Therefore, when Γ is strictly zero and the connection with the reference frame vanishes, the interface instability starts to develop when the classical KH criterion in Eq. (31) is reached. In the limit $T \rightarrow 0$ and $\Gamma \rightarrow 0$, the experimental result is expected to depend on how the observation time compares to the time needed for the interface to become coupled to the environment, and for the superfluid instability to develop at the lower critical velocity. With sufficiently rapid rotational acceleration the classical KH instability might then be reached. Unfortunately at present no experimental verification exists on these predictions.

The real part of the ripplon frequency also crosses zero at the same velocity than the imaginary part. Above the threshold the real part of the ripplon spectrum, and thus its energy in the container frame, becomes negative. This creates a connection to the physics of black holes [88]. In general relativity the region where a particle has negative energy is called the ergoregion. In the ‘shallow water’ limit $kh \ll 1$, when the spectrum

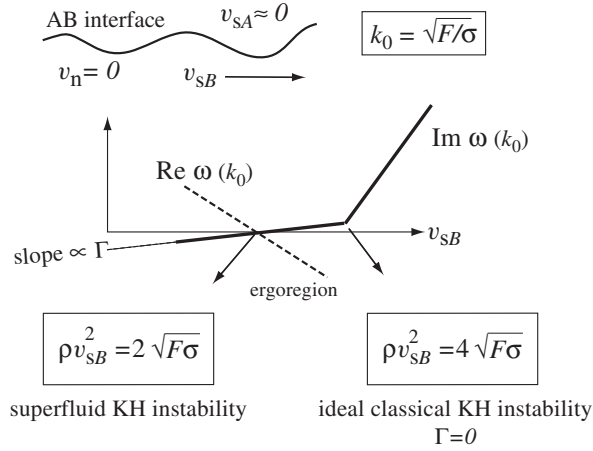


Figure 10. Sketch of the imaginary and real parts of the frequency $\omega(k)$ of the critical ripplon (when $k = k_0$) at the interface between $^3\text{He-A}$ and $^3\text{He-B}$. The diagram is constructed in the rotating frame with $v_{sA} \approx v_{nA} = v_{nB} = 0$ and $\rho_A \approx \rho_B = \rho$ on approaching the limit $T \rightarrow 0$, and considering only incremental changes from the critical conditons. At the superfluid instability, the imaginary part $\text{Im } \omega(k)$ crosses zero as a function of v_{sB} and the attenuation of riplons transforms to amplification. Simultaneously the real part $\text{Re } \omega(k)$ also crosses zero. The region where $\text{Re } \omega < 0$ and where the ripplon has negative energy is called ergoregion. The slope of the imaginary part is proportional to the friction parameter Γ . If Γ is strictly zero, and thus the connection with the environment is lost, the surface instability occurs at the value of v_{sB} larger by a factor $\sqrt{2}$ – at the corner point which is part of the branch obeying the ideal classical KH criterion of Eq. (23).

of riplons becomes ‘relativistic’, an exact analogy with the relativistic quantum field in the presence of the black- or white-hole horizons emerges [89].

It is also possible here to identify a similarity with the Kelvin-wave instability of an isolated vortex line in applied flow. In the $T \rightarrow 0$ limit, when both $\alpha \rightarrow 0$ and $\alpha' \rightarrow 0$, the instability of a vortex line in externally applied superflow towards the formation of Kelvin waves resembles the A-B interface instability. For the unstable modes in Fig. 10 with $\text{Im } \omega > 0$, the real part of the spectrum is negative, $\text{Re } \omega < 0$. Similarly, for a vortex of finite length L the wave-number is constrained from above, $k < k_0 = 2\pi/L$, and the instability forms at a critical velocity $v_c \sim \tilde{\kappa}k_0$. This v_c does not depend on the friction parameter α , whose role is to provide the dissipation from the interaction between the vortex and the environment (*i.e.* the normal component).

To conclude, we have found that the central property of the superfluid KH instability is that the instability condition does not depend on the relative velocity of the superfluids, but on the velocity of each of the superfluids with respect to the environment. The instability occurs even if the two fluids have equal densities, $\rho_A = \rho_B$, and move with the same velocity, $U_A = U_B$. This situation resembles that of a flag flapping in wind. It was originally discussed with the view of the KH instability of ideal fluids by Lord Rayleigh [79]. One might assume the instability to be that of a

passive deformable membrane between two distinct parallel streams having the same density and velocity, as in the superfluid KH example: the flag being represented by the A-B interface, and the flagpole which pins the flag serving as the reference frame fixed to the environment so that the Galilean invariance is violated. However, the correct explanation of the flapping flag requires the presence of friction (for recent developments see *e.g.* Ref. [90]).

In the study of coherent quantum systems the special case of a free surface is of great interest. Obviously the instability occurs even if the two superfluids are on the same side of the interface, *i.e.* with a free surface over a pool of two or more interpenetrating superfluid components, such as a dilute solution of superfluid ^3He in superfluid ^4He or the neutron and proton superfluids in a neutron star [10]. The instability exists even in the case of a single superfluid below the free surface under the relative flow of the normal and superfluid components, as has been pointed out by Korshunov [9]. He also derived two criteria for the instability, depending on the coupling to the environment. In this case the frame-fixing parameter which regulates the interaction with the environment is the viscosity η of the normal component of the liquid. For $\eta \neq 0$ the critical counterflow velocity $v = v_s - v_n$ for the onset of the surface instability is independent of η , but does not coincide with the ideal classical result which is obtained when viscosity is neglected ($\eta = 0$):

$$v^2(\eta \neq 0) = \frac{2}{\rho_s} \sqrt{\sigma F} = \frac{\rho_n}{\rho} v^2(\eta = 0) . \quad (36)$$

In laser-cooled rotating atom clouds in the Bose-Einstein-condensed state the instability of the free surface is the generic vortex formation process [91, 92]. Another case of vortex formation via surface instability is the interface between the normal and superfluid states of the same fluid, which are flowing at different velocities. Such a situation has been discussed extensively for rotating $^3\text{He-B}$ which is irradiated with thermal neutrons [3, 93].

Finally, it is worth noting that these ideas might find applications when studying the instability of quantum vacuum beyond the event horizon, or the ergoregion of the black hole [5]. At the superfluid KH instability the ergoregion develops on the A-B interface, as the energy of the surface waves becomes negative. Such ripplons are excitations of the A-B interface and provide a connection to the presently popular idea in cosmology proposing that the matter in our Universe resides on hypersurfaces (membranes or simply branes) in a multidimensional space. Branes can be represented by topological defects, such as domain walls or strings, and by interfaces between different quantum vacua. In superfluid ^3He , the brane is represented by the A-B interface between the two quantum vacua, $^3\text{He-A}$ and $^3\text{He-B}$. With the A-B interface instability, it might then be possible to model the instability of the quantum vacuum in the brane world. The latter occurs in the ergoregion owing to the interaction between the matter on the branes (represented by ripplons) and the matter in higher-dimensional space (represented by quasiparticles in the bulk superfluids).

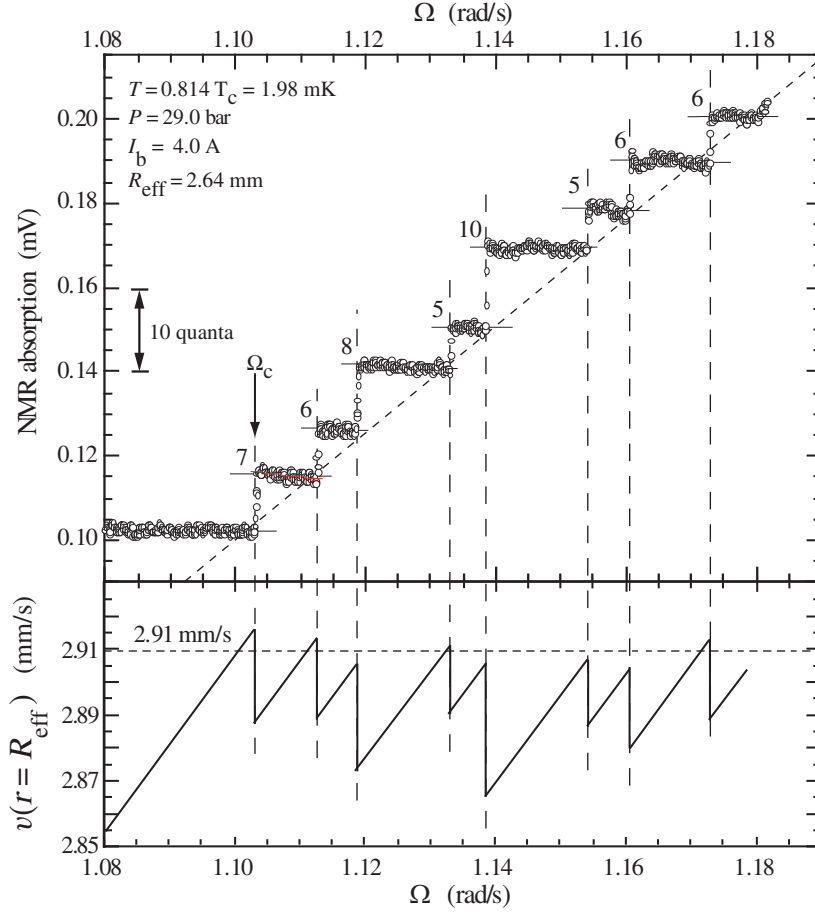


Figure 11. Measurement of the superfluid KH instability of the A-B interface. (Top) A step-like increase in absorption is observed in the Larmor region of the NMR line shape when the rotation velocity Ω is slowly increased and the critical value of counterflow velocity v_c is reached. The KH instability occurs repeatedly in the form of different independent events as a function of Ω . A random number of ΔN rectilinear vortex lines are formed in each event in the B-phase section of the sample (see Fig. 7). (Bottom) At the instability the critical counterflow velocity $v_c(R_{\text{eff}})$ is abruptly reduced by $\kappa\Delta N/(2\pi R)$ to a sub-critical level. The constant critical counterflow velocity v_c gives rise to the dashed lines in each panel. $R_{\text{eff}} \lesssim R$ is the effective radius at which the instability occurs (see Refs. [94, 58] for details.)

3.6. Measurement of A-B interface instability

The superfluid KH instability of the A-B interface is a new physical phenomenon with wide-ranging ramifications, as discussed in Secs. 3.1 – 3.5. It also provides a whole new set of tools for further measurements on vortex dynamics. The standard KH measurement is that of the critical rotation velocity Ω_c shown in Fig. 11. Here the NMR absorption plotted on the vertical scale monitors the number of rectilinear vortices in the B phase while the rotation velocity Ω on the horizontal axis is slowly increased. Temperature T and barrier current I_b are kept constant during the measurement. The first discontinuous jump in NMR absorption marks Ω_c . This is the rotation velocity at

which the first vortices are formed in the initially vortex-free B phase. If Ω is increased further, the instability occurs repeatedly at the same value of critical counterflow velocity $\mathbf{v}(r \approx R) = \mathbf{v}_n(R) - \mathbf{v}_s(R)$ (denoted with dashed lines in both panels). Thus the staircase-like pattern of NMR absorption is composed of steps of different height and can be calibrated to provide the exact number of vortices which is transferred across the A-B interface in each single instability event. Their number ΔN is denoted next to each instability event. We see that ΔN is a small random number, which after many similar measurements is found to be between 3 — 30 with an average of ~ 10 [94]. The measurement in Fig. 11 is performed at high temperatures where each of the ΔN vortex loops rapidly develops into a rectilinear B-phase vortex line, after they have been tossed as a tight bundle across the A-B interface. From such measurements at different temperatures, Ω_c has been collected to provide the curves at different values of I_b seen in Fig. 9.

In the measurement of Fig. 11 the sample might be in either the BA or BAB configurations. In the setup of Fig. 7 the magnetic field distribution along the vertical axis is almost symmetric with respect to the middle of the sample. Also the end plates of the sample cylinder and the NMR pick-up coils are at the same distance from the A-B interfaces in both B-phase sections. As a result the measured values of Ω_c in the top and bottom B-phase sections are identical in the BAB configuration.

A schematic illustration is shown in Fig. 12 of the process in which the ΔN vortex loops might be transferred across the A-B interface. When the thermodynamic instability threshold is reached while increasing Ω , surface waves with wave vector $k_0 = \sqrt{F/\sigma}$ begin to form on the A-B interface. At this stage the ΔN vortices correspond to the A-phase circulation quanta which reside in one of the corrugations of the wave where it is about to become the deepest and most dominant trough. In the lower row of diagrams in Fig. 12 the possible sequence of events is depicted which might then take place for this trough. The interface motion is highly damped, it moves much faster than the vortices, and thus the trough is rapidly smoothed out after the vortex bundle has traveled below the equilibrium level of the A-B interface and the counterflow velocity at the interface has dropped below the critical value. In this way the superfluid circulation is left behind in the B phase.

A further illustration of the KH measurement and its agreement with Eq. (30) is shown in Fig. 13. This plot is generated by measuring Ω_c as in Fig. 11 and by collecting data from measurements at different barrier fields, but at constant temperature. The result demonstrates the dependence on the restoring force acting on the A-B interface. When the field in the barrier magnet is changed the A-B interface moves such that it always remains in the equilibrium transition field H_{AB} . Depending on the location of the phase boundary within the magnet, the gradient of the field dH/dz varies according to the field profile of the barrier solenoid. The curve starts at low barrier fields approximately from the point where the maximum field inside the barrier magnet equals the equilibrium field $H_{AB}(T, P)$. This is in the region of the axial field profile of the barrier solenoid where dH/dz is close to maximum and where it changes rapidly with

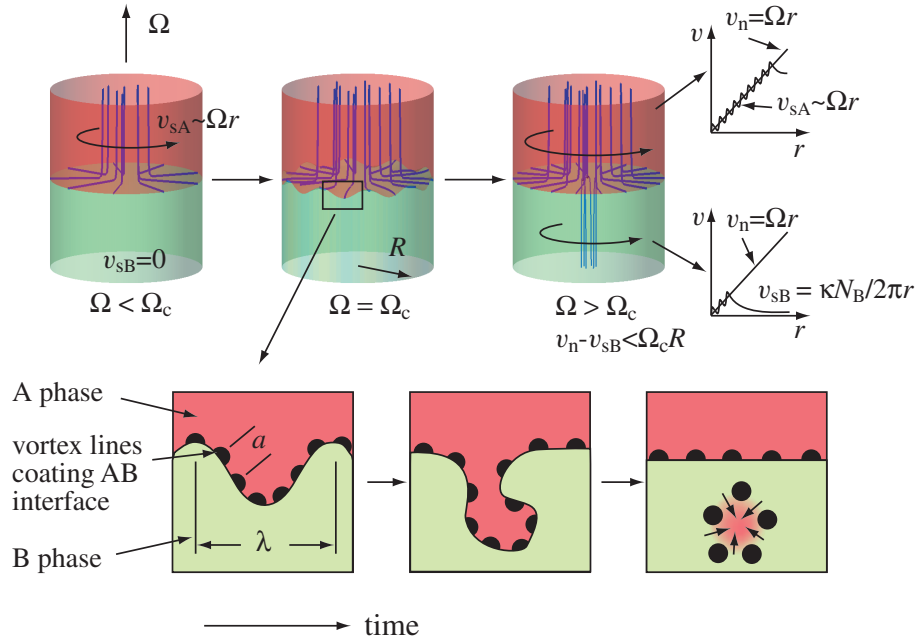


Figure 12. Schematic illustration of how a KH instability event might evolve on the A-B interface. (*Top row*) Initially when rotation is increased, vortices form at a low critical velocity in the A phase section while none are formed in B phase. At the critical B-phase counterflow velocity the A-B interface becomes unstable towards wave formation, ΔN vortex loops end up on the B-phase side of the interface, and then develop to rectilinear vortex lines. The end result from the instability is that the vortex lines, which pass through the A-B interface, wind up the B-phase superflow velocity and the boundary settles down. In the upper right corner the velocities are sketched of the normal (v_n) and superfluid (v_{SA} , v_{SB}) components in the two phases. They are shown here in the laboratory frame as a function of r in the situation after the instability event (see also Fig. 2). (*Bottom row*) A schematic illustration of how the vortex injection might happen. When the boundary becomes unstable, waves form on the interface. A small number of vortex lines becomes trapped in the deepest corrugation which expands to the B-phase side (where $H < H_{AB}(T)$ and A phase is unstable). The corrugation becomes separated and the A phase shrinks away but the circulation is left behind.

z . When the current I_b is increased, the location of the A-B interface moves further from the magnet center and to lower values in the dH/dz profile of the magnet. Therefore the slope of the curve in Fig. 13 decreases with I_b . With this measurement one can examine what is the geometry in which the A-B interface first forms at low barrier current and how much magnetic hysteresis is involved [95].

With a given barrier magnet the KH instability is restricted to the range of velocities allowed by Eq. (30). With the barrier magnet of the setup in Fig. 7 the critical velocities Ω_c are in the range 0.7 – 1.6 rad/s, as seen in Figs. 9 and 13. However, vortex loop injection into vortex-free B-phase flow can be performed at higher rotation velocities using the following procedure: The barrier field is initially reduced well below the equilibrium value $H_{AB}(T, P)$ of the field needed to stabilize A phase. Thus there is

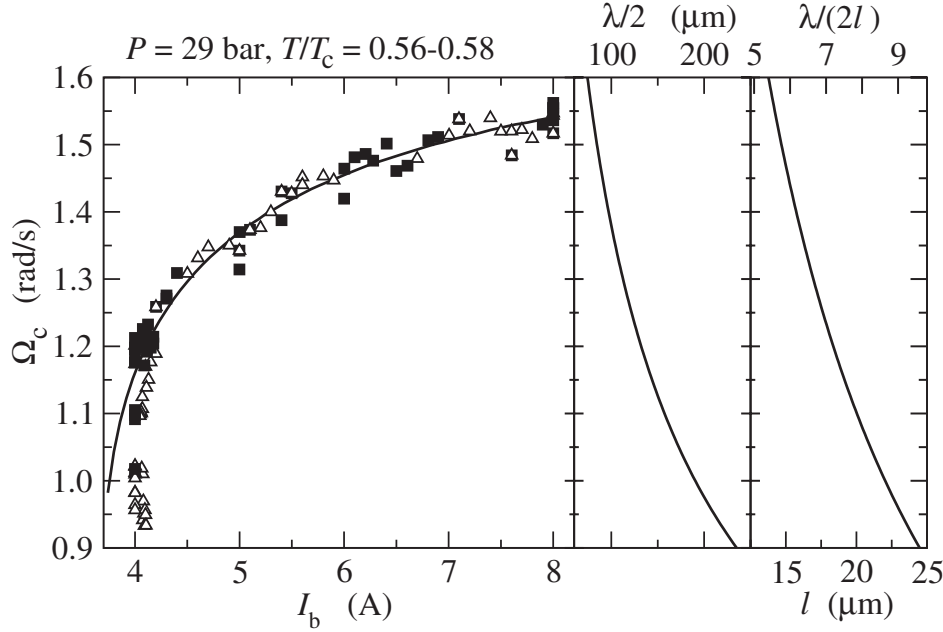


Figure 13. A-B interface instability as a function of the restoring force at constant temperature. (*Left*) Measured critical rotation velocity Ω_c of the first KH instability event as a function of the current I_b in the barrier magnet. These measurements are conducted in the temperature regime of the hydrodynamic transition between regular and turbulent vortex dynamics: (Δ) open symbols mark events in which only a small number of ΔN new vortices are formed in the B-phase section; (\blacksquare) filled symbols denote events in which a turbulent burst increases the B-phase vortex number to N_{eq} . The solid curve represents Eq. (30) without fitted parameters. (*Middle*) Half of the calculated ripplon wavelength λ at the instability according to Eq. (25). (*Right*) The bottom axis gives the separation between vortex quanta on the A-B phase boundary on the A-phase side, calculated from the number of vortices in the A-phase section (when these are distributed evenly in single-quantum units along the outer sample circumference $r = R$). The top axis gives the number of single-quantum units expected in one trough ($\lambda/2$) of the surface wave. This number $\lambda/2l$ agrees with the measured average for $\Delta N \approx 10$ (see Ref. [94] for details).

no A phase in the sample volume. The rotation velocity is then increased to the desired value above the critical velocity Ω_c of KH instability. In this all-B-configuration the vortex free state can be maintained up to the velocity at which vortex formation from other sources starts. Next the barrier field is ramped up. A phase then forms in a sudden hysteretic transition at a magnetic field which exceeds the equilibrium value H_{AB} . Because of this superheated transition, the A phase and its vortices form rapidly within a larger volume. In such a highly non-equilibrium transition a large number of vortices is suddenly transferred into the B phase (if $\Omega > \Omega_c$). The A-B interface then settles down, when the B-phase superflow velocity has been reduced below the critical value. Thus in this process the final state at high temperatures above the turbulent regime is close to that expected from Eq. (30). This injection technique is useful for

studying the propagation of a large number of vortices at velocities above Ω_c at any temperature where the A-B interface exist.

The KH shear-flow instability provides a convenient mechanism for precise vortex injection into initially vortex-free applied flow. This is its principal application in the dynamical measurements which are described in the next sections. Its critical velocity is predictable and can be tuned externally. Also with the KH instability it becomes possible to inject a bundle of vortex loops as an externally triggered event: the rotation velocity can be stabilized as close as within $\Delta\Omega \sim 0.01 \text{ rad/s}$ below the threshold Ω_c and then suddenly increased by 0.02 rad/s to start the KH event. Such reliability of the KH instability as a vortex injection technique allows new measurements on the dynamic evolution of vortex lines in applied flow. The prime example is the determination of the vortex flight time, a measurement of the velocity at which a vortex propagates into vortex-free applied counterflow in a rotating column (Fig. 6b). However more importantly, the KH instability provided the arguments for identifying the hydrodynamic transition from regular to turbulent vortex dynamics which occurs on cooling below $\sim 0.6 T_c$, *i.e.* it allowed to distinguish a new phenomenon from other sources of uncontrolled vortex formation.

4. Transition from regular to turbulent dynamics

4.1. Introduction

At high temperatures above $0.6 T_c$ the dynamical behavior of vortices in $^3\text{He-B}$ is regular, *i.e.* their number does not increase during a time-dependent process, as can be seen in Figs. 3 and 11 from the measured constancy of the critical velocity. Some time ago it was recognized that at lower temperatures single-vortex processes are not observed in large applied flow [44]; instead, a large number of vortices is suddenly formed so that the final state in rotation appears to include close to the equilibrium number of vortex lines. More recently, a consistent explanation of this phenomenon has been presented [11]. On the basis of the measurements of the Kelvin-Helmholtz instability, it is now understood that mutual friction divides the dynamics in $^3\text{He-B}$ into a high-temperature regime with regular vortex-number conserving motion, and a low-temperature regime where superfluid turbulence becomes possible. This hydrodynamic transition is unusually abrupt as a function of temperature, as seen in Fig. 14. This is the reason why it was first mistakenly interpreted to signal a strongly temperature-dependent new critical velocity in Ref. [44]. The applied flow velocity, the counterflow velocity $\mathbf{v}_n - \mathbf{v}_s$, is an important factor in this transition: at low velocity a single vortex has been observed to be in stable precessing motion for an entire day at temperatures down to below $0.2 T_c$ [96]. A similar result has been verified for $^4\text{He-II}$ [97]. With increasing flow velocity the vortex undergoes an instability towards the formation of Kelvin waves, which may or may not lead to a rapid multiplication in the number of vortex lines. The fate of the instability depends on the parameter q of the mutual friction.

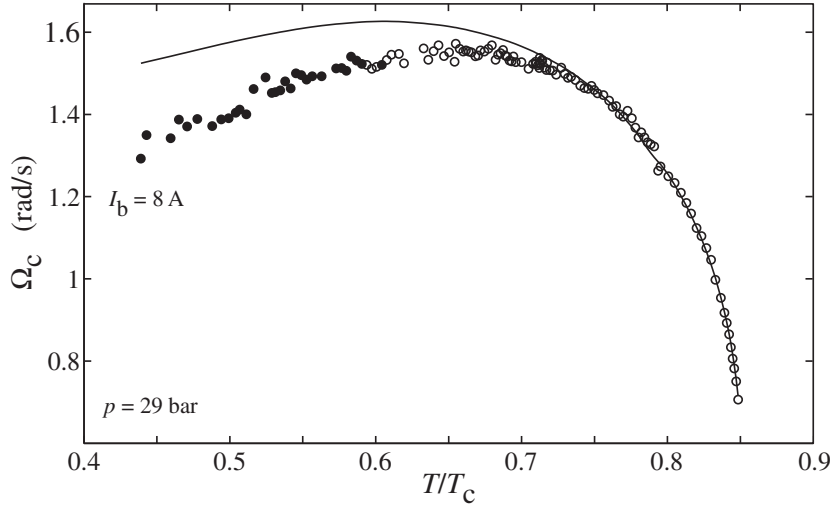


Figure 14. Critical rotation velocity $\Omega_c = v_c/R$ of the first KH instability event at high barrier field, when the A-phase section is stable down to $T \rightarrow 0$, or $H_b > H_{AB}(T = 0)$. The data points have been classified according to the nature of the dynamic evolution after injection: (\circ), regular vortex number conserving; (\bullet), turbulent burst. A transition in the dynamics is seen to take place at about $0.59 T_c$, with little overlap of open and filled symbols in the transition regime. The solid curve denotes the calculated dependence from Eq. (30) without fitting parameters. In the absence of more appropriate parameter values, mainly isotropic zero-field values have been used which do not seem to provide perfect agreement at high barrier field (here $I_b = 8.0$ A).

The transition from regular to turbulent dynamics as a function of mutual-friction dissipation is a new phenomenon. It has not been observed in $^4\text{He-II}$; in this case the transition is expected only a few tens of μK below T_λ , where ρ_s is vanishingly small and the superfluid state very different from that further below T_λ . In $^3\text{He-B}$ the transition is in the middle of the experimentally accessible temperature range where the superfluid properties are continuous and well developed. Here the transition can be observed in one experiment by scanning temperature from the superconductor-like dynamics at high vortex damping to superfluid ^4He -like turbulence at low damping. This shows that superfluid dynamics can be varied and that the traditional ^4He -like superfluidity is just one limiting case on this spectrum. The opposite extreme is superfluid $^3\text{He-A}$ where sufficiently low temperatures to reach turbulence are probably not experimentally realistic.

In this section we first describe how the transition appears in the KH measurements. We then proceed with some models for its explanation.

4.2. Regular vs turbulent dynamics in Kelvin-Helmholtz measurements

Fig. 14 shows the KH critical velocity measured as a function of temperature. Here the data points have been classified according to whether the final state after the first

critical event only includes the vortices generated in the KH event itself (open symbols), or if it incorporates almost the equilibrium number of vortices (filled symbols). A sharp division line, with little overlap of open and filled data points, is seen to divide the plot into two regimes as a function of temperature: at high temperatures only the KH vortices are generated while at low temperatures the equilibrium vortex state is obtained after the instability event. The KH critical velocity as a function of temperature is a continuous smooth curve across this division line and continues to follow the calculated dependence. The same features are illustrated in Fig. 13 which is measured at the temperature of the division line. A surprising and characteristic property of these plots is that there are essentially no data points with an arbitrary intermediate number of vortices, not even in the transition regime.

The conclusion from these measurements is that at temperatures below the division line a short turbulent burst follows the KH event, after the closely packed bundle of vortex loops has arrived across the A-B interface into the vortex-free B-phase flow (Fig. 12). The turbulent burst generates the vortices needed to reach almost the equilibrium number of vortices for the B-phase flow. The propagation and dynamic state of these vortices, when they move along the long rotating sample, is discussed in Sec. 5. A compelling argument for the interpretation in terms of a turbulent burst is the continuity of the KH critical velocity across the division line – it is unrealistic to assume that the nature of the instability would so suddenly change entirely. The KH instability is one example of the injection of vortex seed loops in externally applied flow. Other examples are examined in Sec. 4.6. However, since the KH instability was originally the most convincing case of vortex injection and of the turbulent burst, with very particular properties, we want to describe them here in more detail.

Figure 15 shows a close-up of the transition region as a function of temperature. The number of vortex lines N is plotted, normalized by the equilibrium number N_{eq} , after a single event of KH injection. At high temperatures the injection leads always to a small number of rectilinear lines, as expected for the KH instability (Fig. 11). Below $0.6 T_c$ the number of lines, after the system has settled down, is very different: the injection results in the almost complete removal of the counterflow. The two regimes are here separated by an abrupt transition at $T_0 \approx 0.58 T_c$ which has a narrow width of $\Delta T_0 \approx 0.04 T_c$. We attribute this sudden change in the final state as the fingerprint of a brief burst of turbulence which multiplies the vortex number close to N_{eq} . Here with KH injection the turbulent burst occurs at the injection site at a distance of 30 mm from the closest end of the detection coil. Thus there is no direct NMR signal which would identify the burst itself, only the propagating vortex state after it has traveled from the A-B interface to the detection coil. This means that the turbulent burst is short in duration and localized to some section of sample length adjacent to the A-B interface.

In the transition regime the turbulent burst may not be triggered by the first vortex injection event. Instead, a turbulent burst can be preceded by one or more KH injection events which do not lead to vortex multiplication. However, once turbulence

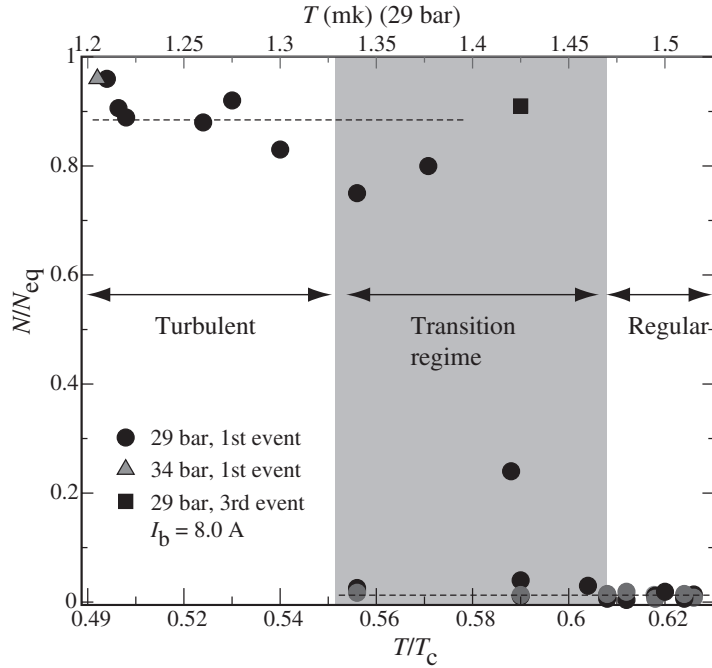


Figure 15. The number of rectilinear vortex lines N after KH injection, normalized to the equilibrium number of lines N_{eq} , plotted as a function of temperature. At around $0.58 T_c$, a sharp transition in the number of lines is observed. At high temperatures the injection results in only a few lines, but at low temperatures the equilibrium number of lines is observed [94].

sets in, it generates the equilibrium number of lines in almost all the cases. Those events where turbulent vortex multiplication terminates before the number of lines reaches the equilibrium value are rare.

The transition from Fig. 15 is shown as a phase diagram in Fig. 16, plotted in terms of the counterflow velocity $v = \Omega_c R$ and temperature T . In this diagram each data point represents a KH injection measurement, accumulated with different settings of the externally controlled parameters, so that as wide variation as possible for the critical rotation velocity Ω_c and temperature T is obtained. Each marker in Fig. 16 thus indicates a KH injection event into vortex-free counterflow with some parameter values which are not of interest in this context. What we are interested in here is the division in filled and open symbols: events followed by a turbulent burst are again marked with filled symbols (■) while events which only lead to a few rectilinear lines are marked with open symbols (□). The transition occurs at about $0.59 T_c$; at higher temperatures no injection events lead to vortex multiplication while at lower temperatures all injections lead to the equilibrium vortex state. The striking new conclusion from this plot is that the phase boundary between turbulence at low temperatures and regular dynamics at high temperatures is vertical, *i.e.* independent of the counterflow velocity.

Plots similar to Fig. 16 were also measured at 34 and 10 bar pressures [98]. In Fig. 17 all the results are summarized. We assume that the transition is velocity independent

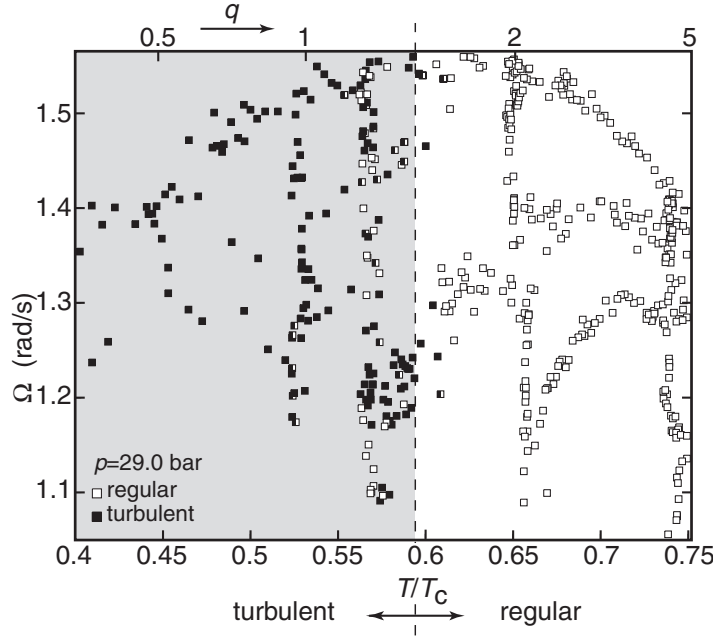


Figure 16. Temperature-velocity phase diagram of turbulence. Each marker in the plot represents the result from a measurement where rotation is increased from zero to the critical velocity Ω_c of the A-B interface instability. The cases where turbulence is observed after the instability are marked with black symbols (■) and the regular cases with a white symbol (□) [11]. The horizontal top axis gives the temperature dependent and velocity independent dynamic parameter $q = \alpha/(1 - \alpha')$. From this we conclude that the phase boundary is primarily determined by its mutual friction dependence.

in the measured range of velocities, and compile the data to show the probability of the transition between regular and turbulent cases as a function of temperature. The fitted Gaussian distributions give a narrow half-width of $\sigma \approx 0.03 T_c$ at all pressures, centered around a transition temperature in the range $0.52 - 0.59 T_c$. Mutual friction data is available at 10 and 29 bar pressures [64]. At 10 bar the transition occurs at $q = 0.6$ and at 29 bar $q = 1.3$, where the parameter q is introduced in Eq. (15). This shows that the transition moves to higher q value with increasing pressure. Measurements were also carried out at zero pressure where the transition was found to be below $0.45 T_c$ at low rotation velocities of $0.5 - 0.7$ rad/s.

To conclude, the measurements indicate that the phase boundary between turbulent and regular vortex dynamics is foremost a function of temperature and thus of mutual friction, such that it occurs when the dynamic parameter q is of order unity. Also the width of the transition, which is unusually narrow for hydrodynamic transitions, points to the exponential temperature dependence of mutual friction.

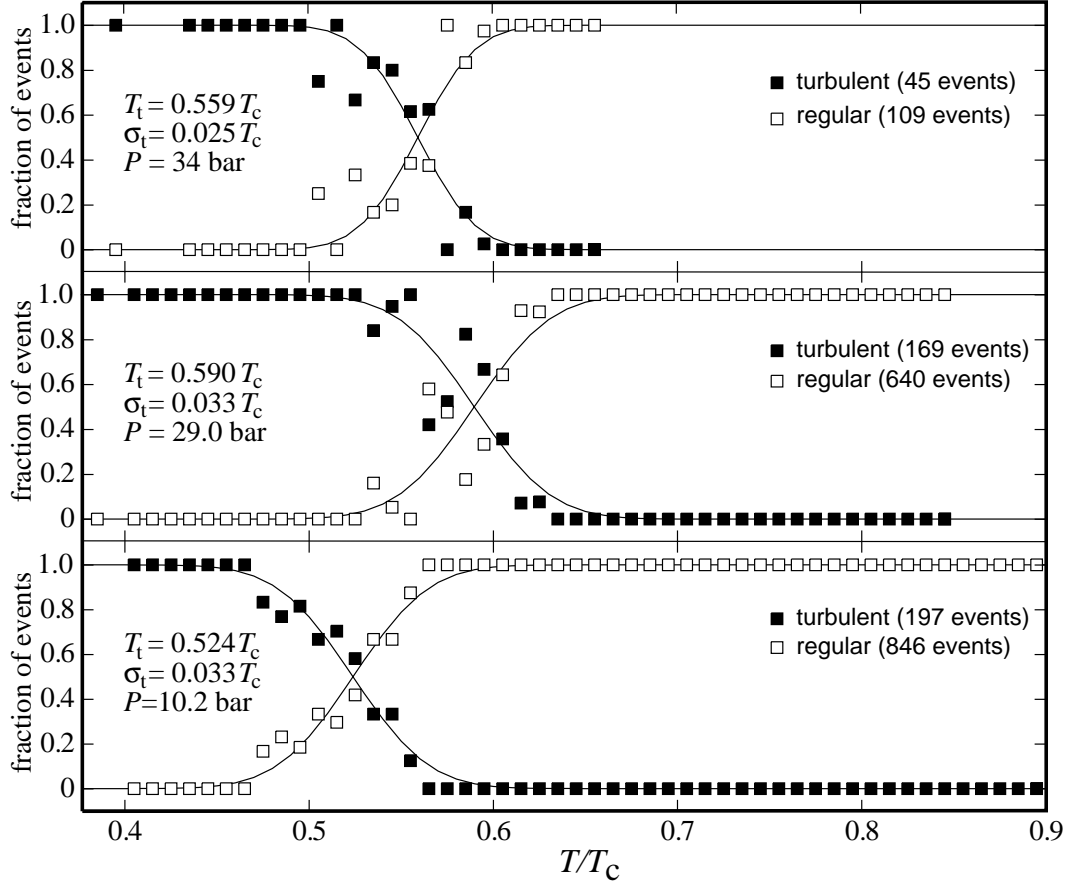


Figure 17. Transition between regular and turbulent vortex dynamics at different pressures. The transition is assumed velocity independent and the events are categorized according to their temperature [98]. The transition temperature increases with pressure, but the half width of its distribution is approximately $\sigma \approx 0.03 T_c$ at all pressures.

4.3. Classical and superfluid turbulence

Since classical and quantum turbulence share some common features, we begin with some basic concepts from classical turbulence by inspecting the properties of the different terms in the Navier-Stokes equation [84]

$$\frac{\partial \mathbf{v}}{\partial t} + \nabla \tilde{\mu} = \mathbf{v} \times \boldsymbol{\omega} + \nu \nabla^2 \mathbf{v} . \quad (37)$$

Here ν is the kinematic viscosity (viscosity η /density ρ), $\boldsymbol{\omega} = \nabla \times \mathbf{v}$ is the vorticity in the inertial (laboratory) reference frame. Turbulence is governed by the interplay of the two terms on the r.h.s. of this equation, the inertial (first) term and the viscous (second) term.

The transition to turbulence is determined by the Reynolds number $\text{Re} = LU/\nu$, formed from the characteristic values for the three quantities describing the flow: its velocity U , the geometric size of the system L , and the kinematic viscosity ν . For small

Reynolds numbers, the viscous term $-\nu k^2 \mathbf{v}_\mathbf{k}$ for the perturbation with a wave vector \mathbf{k} , stabilizes laminar flow. In contrast, at large $\text{Re} \gg 1$ the inertial term in Eq. (37) dominates, and laminar flow becomes increasingly unstable against the formation of a disorganized flow of eddies. In the most carefully prepared experiments laminar flow has been maintained in a circular pipe up to $\text{Re} \sim 10^5$ [99]. However, the higher the Reynolds number the smaller the disturbance needed to trigger turbulence [100]. The evolution of turbulence is governed by the Kolmogorov energy cascade: the kinetic energy of the flow is transferred to smaller and smaller length scales, via the decay and break up into ever smaller vortex loops along the so-called the Richardson cascade [101], until a length scale is reached where the energy can be dissipated by viscosity.

In superfluids turbulence acquires new features. First, the superfluid consists of two inter-penetrating components: the frictionless superfluid and the viscous normal fractions. The total density $\rho = \rho_n + \rho_s$ is the sum of the densities of these two components. The normal component behaves like a regular viscous fluid while the superfluid component is an ideal superfluid. At the superfluid transition the density of the superfluid component vanishes, but increases with decreasing temperature, until in the $T \rightarrow 0$ limit the normal component vanishes. Secondly, the vorticity of the superfluid component is quantized as discussed in Section 2.1. If both the normal and superfluid components are able to move, the turbulent state bears more resemblance to the turbulence of classical viscous liquids. This is often the case in superfluid $^4\text{He-II}$ [1]. In superfluid ^3He , however, the normal component is so viscous that it is essentially immobile. The flow is then carried by the superfluid component which contains a large number of quantized vortices. Here a new class of turbulent flow becomes possible: *one-component superfluid turbulence*. It is this state of turbulent flow that we consider in what follows.

Because of its large viscosity, for instance in rotation the normal component of $^3\text{He-B}$ moves together with the container. As a result, Eq. (10) takes the following form in the frame where the normal component is locally at rest ($\mathbf{v}_n = 0$):

$$\frac{\partial \mathbf{v}_s}{\partial t} + \nabla \tilde{\mu}_s = (1 - \alpha') \mathbf{v}_s \times \boldsymbol{\omega}_s + \mathbf{f}_{visc}, \quad (38)$$

where

$$\mathbf{f}_{visc} = \alpha \sum_{\beta} \int \delta(\mathbf{r} - \mathbf{r}_{\beta}) d\mathbf{r}_{\beta} \times (\hat{\mathbf{s}}_{\beta} \times \mathbf{v}_s)$$

is the viscous part of the mutual friction force.

The first inertial term on the r.h.s. drives the flow instability towards turbulence in the same way as the inertial term in the Euler equation does for potential flow in classical hydrodynamics [84]. The second dissipative term on the r.h.s. of Eq. (38) corresponds to the second dissipative term in the Navier-Stokes equation (37). It tends to stabilize the flow, since it leads to energy dissipation

$$\frac{\partial}{\partial t} \frac{v_s^2}{2} = \mathbf{v}_s \cdot \mathbf{f}_{visc}, \quad (39)$$

where $\mathbf{v}_s \cdot \mathbf{f}_{visc} < 0$ according to Eq. (13). The fundamental difference between the dissipative terms in classical and superfluid dynamics is that in superfluids this term has the same scaling dependence on velocity and vorticity $f_{visc} \sim \alpha \omega_s v_s$ as the inertial term. This is a consequence of the two-fluid dynamics, where the vortices provide the mechanism of momentum and energy transfer between the two components of the fluid. Thus the effective Reynolds number – being defined as the ratio of the inertial and dissipative terms in the relevant hydrodynamic equation – has to be changed. In superfluids, it is the ratio of the two terms on the r.h.s. of Eq. (38):

$$\Re = (1 - \alpha')/\alpha = 1/q. \quad (40)$$

According to this definition, and in analogy with classical hydrodynamics, turbulence in superfluids is expected when $1/q \gtrsim 1$ and laminar (regular) flow when $1/q \lesssim 1$. As distinct from viscous liquids, this condition is independent of extrinsic quantities such as the counterflow velocity or the characteristic dimension R of the sample. The temperature dependence of \Re for $^3\text{He-B}$ and He-II is explicitly shown in Fig. 5.

The above dimensional arguments on the transition between regular and turbulent vortex dynamics are in agreement with the results in Fig. 16, where the boundary between the laminar and turbulent regimes was also found to be at $q \sim 1$. Thus the velocity independent parameter $\Re = 1/q$, which controls the transition to turbulent flow in superfluids, plays the same role as the velocity dependent Reynolds number $\text{Re} = UR/\nu$ in classical hydrodynamics.

These considerations are valid provided that the superflow velocity is high enough to sustain vortices, *i.e.* exceeds the Feynman critical velocity (see Section 2.3), which is easily satisfied in $^3\text{He-B}$. With the Feynman criterion, one can define another dimensionless parameter, the “superfluid Reynolds number”

$$\text{Re}_s = U_s R / \kappa, \quad (41)$$

where U_s is the mean superfluid velocity with respect to the normal component, *i.e.* the counterflow velocity. If the condition $\text{Re}_s \gtrsim 1$ is fulfilled up to a logarithmic prefactor $\ln(R/\xi)$, it becomes energetically favorable to add a vortex line in the bulk flow.

4.4. Onset of turbulent burst

In KH injection a tight bundle of many small vortex loops (of size $\sim 400 \mu\text{m}$) are transferred across the A-B interface into vortex-free B-phase flow. How is a turbulent burst started after the injection? In this section we discuss the initial phase of vortex multiplication in applied flow using a simple phenomenological model constructed in the spirit of the Vinen model equation for superfluid turbulence [102].

To characterize the initial conditions we need two numbers: the intrinsic velocity independent $\Re = 1/q$ in Eq. (40) and the “superfluid Reynolds number” Re_s in Eq. (41). We assume $\text{Re}_s \gg 1$ which corresponds to the typical situation in $^3\text{He-B}$ when a large number of vortices is energetically allowed in the container. If a large energy barrier prevents vortex nucleation, then vortices are not necessarily created even at

high $\text{Re}_s \gg 1$ and the superfluid remains in a state of vortex-free counterflow. At velocities well below the intrinsic critical velocity of vortex formation (see Section 2.3), $v_c \sim \kappa/\xi$ [44], superfluid turbulence can be initiated if quantized vortices are injected by some extrinsic means into the flow. In the rotating sample turbulence develops in a sudden burst when the initial vortices start to multiply and form a vortex tangle in the bulk volume.

We start with an initial configuration containing many (essentially more than one) randomly oriented vortex loops, which might have been either injected or created by some other precursor process from a set of few vortices. An example of the precursor can be the Kelvin-wave instability discussed in Section 2.6. We show that the initial array of entangled vortices is unstable towards a burst-like multiplication of vorticity provided the mutual friction is low enough. We assume that vortex multiplication occurs within a certain region in the fluid where the number of vortices is large. The multiplication region can exist near the location of the seed loops and/or near the walls of the rotating container, where both the counterflow velocity and the number of vortices, increased effectively by the image vortices, are largest. A vortex tangle created in the multiplication region next penetrates into the rest volume of the fluid.

Since the superfluid vorticity is quantized, the formation of new vortices during the onset becomes the key issue. We consider this process, taking mutual friction into account, and derive an equation for the evolution of the density of entangled vortex loops during the initial stages of the transition to turbulence. The multiplication of seed vortices can be studied with Eq. (38). Taking the curl of both sides in Eq. (38) we obtain the equation for the superfluid vorticity

$$\frac{\partial \boldsymbol{\omega}_s}{\partial t} = (1 - \alpha') [\nabla \times (\mathbf{v}_s \times \boldsymbol{\omega}_s)] + \nabla \times \mathbf{f}_{visc} . \quad (42)$$

Here we assume that the vorticity produced by turbulence is much larger than the angular velocity $\omega_s \gg \Omega$, *i.e.* the vortex density is much higher than that in equilibrium. This allows us to neglect $\nabla \times \mathbf{v}_n = 2\boldsymbol{\Omega}$ as compared to $\boldsymbol{\omega}_s$.

Let us now average Eq. (42) over randomly oriented vortex loops with dimensions spread over an interval around a characteristic size ℓ . In a state of entangled vortex loops, their three-dimensional density is $n_v \sim \ell^{-3}$ while the vortex-loop length per unit volume [102] (two-dimensional vortex density) is $L = \ell n_v = \ell^{-2} = n_v^{2/3}$. After averaging Eq. (42) only its scalar value is meaningful, as any of its components to a specific direction vanishes. Let us express the two terms on the r.h.s. of Eq. (42) in terms of the vortex density L , keeping in mind that the velocity produced by the vortex tangle is of the order of $\tilde{\kappa}/\ell$, while its vorticity is $\omega_s \sim \tilde{\kappa}/\ell^2 \sim \tilde{\kappa}L$ where $\tilde{\kappa} = (\kappa/4\pi) \ln(\ell/\xi)$.

Regarding the onset of turbulence, the reactive coefficient α' in Eq. (42) simply renormalizes the inertial term of conventional hydrodynamics [the first term in r.h.s. of Eq. (37)] that drives the instability towards turbulent vortex formation. Therefore, the vortex density *increases* due to the first term in Eq. (42) according to

$$\dot{L}_+ = A(1 - \alpha')v_s L^{3/2} = A(1 - \alpha')(U - v_0)L^{3/2} \quad (43)$$

where $A \sim 1$ is a constant. The superfluid velocity in Eq. (43) is assumed to be $v_s = U - v_0$ where U is the counterflow velocity, and $v_0 \sim \tilde{\kappa}/\ell$ is the self-induced velocity for a vortex loop of length ℓ and core radius ξ . The kinetic energy of the superfluid grows due to the increase in the loop density. The energy is taken from the external source at the length scale R with the rate $dE/dt \sim E_L \dot{L}_+$ where E_L is the energy of the vortex per unit length.

Vortex multiplication saturates when the loop density reaches a value such that $U = v_0 \sim \tilde{\kappa}L^{1/2}$. If the density happens to become larger, it will decrease towards $L_{sat} \sim (U/\tilde{\kappa})^2$ while the kinetic energy is returned back to the external source. In other words, saturation is reached when the “turbulent superfluid Reynolds number” $\text{Re}_s^{(\text{turb})} = U\ell/\tilde{\kappa}$ is of the order of unity. The condition $\text{Re}_s \gg 1$ ensures the separation of scales $\ell \ll R$ that is required for the formation of a vortex tangle. The vorticity at saturation $\omega_{sat} \sim \tilde{\kappa}/\ell_{sat}^2 \sim \text{Re}_s \Omega$ is much larger than the equilibrium vorticity 2Ω . Note that the scale $L_{sat} \sim \ell_{sat}^{-2}$ coincides with the wavelength threshold $k \sim \ell_{sat}^{-1}$ for the Kelvin-wave instability discussed in Sec. 2.6.

The second (dissipative) term in Eq. (42) acts to stabilize the vortex-free flow thus *reducing* the vortex density in a way similar to that in normal fluids. Estimating the dissipative term as $f_{visc} \sim \alpha\omega_s v_s$ we find the rate of vortex density decrease

$$\dot{L}_- = -B\alpha(U - v_0)L^{3/2} \quad (44)$$

where $B \sim 1$ is a constant. In contrast to normal fluids, the dissipative term has the same scaling dependence as the driving term Eq. (43).

The multiplication of vortex loops described by Eq. (43) can be understood in terms of vortex collisions and interconnections. Such processes were indeed seen in numerical simulations on quantized vortices [11, 103, 104]. Reconnections of vortices accompanied by the formation of a vortex tangle in normal fluids were considered recently in Refs. [105, 106]. Each reconnection of quantized vortices takes place over a microscopic time of the order of the quasiparticle collision time, much shorter than the times involved in hydrodynamic processes. It is accompanied by a small dissipation within a volume of the order of ξ^3 . We consider these processes as instantaneous and neglect the corresponding dissipation. The rate of increase in the vortex loop density should be quadratic in n_v , and thus $\dot{n}_+ = Av_r n_v^2 \ell^2$. Here v_r is the relative velocity of the vortex loops, ℓ^2 is the loop cross section, and the constant $A \sim 1$ describes the “efficiency” of the vortex multiplication due to pair collisions. Using the definition of L the vortex multiplication rate becomes $\dot{L}_+ \sim v_r L^{3/2}$. The vortex velocity is determined through the mutual friction parameters α and α' such that $\mathbf{v}_L = (1 - \alpha')\mathbf{v}_s - \alpha \hat{\boldsymbol{\omega}}_s \times \mathbf{v}_s$. After averaging over randomly oriented vortex loops the last term vanishes, resulting in the average relative velocity of loops v_r proportional to the longitudinal component of \mathbf{v}_L , $v_r \sim (1 - \alpha')v_s$. The rate \dot{L}_+ thus agrees with Eq. (43).

The effect of the second viscous term on the r.h.s. of Eq. (42) is to decrease the loop density in the multiplication region by inflating the loops due to counterflow, and extracting them from the multiplication region into the bulk where the counterflow is

smaller. The viscous component of the mutual-friction force leads to variation in the vortex loop length $\dot{\ell} \sim 2\pi v_L \sim \alpha v_s \sim \alpha(U - v_0)$. Finally, for the rate of vortex-loop density variation due to the viscous component one obtains Eq. (44). The length increases while the density decreases as long as the saturation is not reached, $U - v_0 > 0$. If the saturation is exceeded, $v_0 > U$, the density increases since the loops shrink due to the friction. Accordingly, the vortex loops are extracted from the region of their multiplication into the bulk before the saturation $U > v_0$, and they are extracted out of the bulk fluid if $U < v_0$.

As we see, both inertial and viscous mutual friction terms, Eqs. (43) and (44), have the same dependence on the vortex density, *i.e.* on the vortex length scale. The total variation of the loop density in the multiplication region is the sum of the two processes, $\dot{L} = \dot{L}_+ + \dot{L}_-$. Putting $v_0 = \tilde{\kappa}/\ell = \tilde{\kappa}L^{1/2}$ we obtain

$$(1 - \alpha')^{-1} \dot{L} = (q_c - q) (UL^{3/2} - \tilde{\kappa}L^2) . \quad (45)$$

Here the critical value $q_c = A/B$ is generally of order unity.

Equation (45) resembles the Vinen equation [102] for superfluid turbulence in superfluid ^4He . However, the difference is that the coefficient $q_c - q$ can now have either positive or negative sign depending on the mutual-friction parameters. As a result, two limits can now be distinguished.

In the low-viscosity regime, which is typical for $^4\text{He-II}$, $q_c - q > 0$. In this regime, the rate of multiplication is faster, and the number of created vortex loops is large: each new vortex loop serves as a source for producing more vortices. As a result, an avalanche-like multiplication takes place, which leads to the formation of a turbulent vortex tangle. As the number of vortex loops grows, the self-induced velocity increases and finally the saturated density L_{sat} is reached.

In $^3\text{He-B}$ the opposite regime is possible, with $q_c - q < 0$. In this viscosity-dominated regime the rate of extraction of vortex loops exceeds the rate of multiplication; there is no time for vortices to multiply since all the seed and newly created vortices are immediately wiped away into the bulk fluid. The number of vortices in the final state is essentially equal to the number of initial vortices, and the turbulent state is not formed. The corresponding stable solution to Eq. (45) is $L \rightarrow 0$. Equation (45) also has another point of attraction, $L \rightarrow \infty$. This would correspond to a decay of initially created vortex tangle in a situation without net counterflow: the vortex loops shrink due to the viscous mutual-friction force.

One can see that the condition of instability for an entangled vortex array $q \lesssim 1$ is essentially the same as the condition for the propagation of underdamped Kelvin waves along an isolated vortex line, established in Section 2.6. This indicates that the mutual-friction low-viscosity threshold $q \lesssim 1$ is not just an accidental value of one of the parameters, but may be of a much more general and fundamental importance for the superfluid dynamics; however, its role remains yet to be fully investigated.

To justify our assumption that the normal component does not participate in superfluid turbulence we compare the viscous force $\eta_n k^2 v_n$ in the Navier-Stokes equation

(37) and the mutual friction force of Eq. (12) exerted on the normal component $F_{mf} \sim \alpha \rho_s \omega_s (v_s - v_n)$. Here $\eta_n = \rho_n \nu$ is the normal dynamic viscosity, and k is the wave vector of the velocity field. Variations of v_n are smaller than those of v_s when $\nu k^2 \gg (\rho_s/\rho_n) \alpha \omega_s$. We estimate $k^2 \sim \ell^{-2}$ and $\omega_s \sim \kappa/\ell^2$ in terms of the vortex-line density. The condition becomes

$$\nu/\kappa \gg (\rho_s/\rho_n) \alpha .$$

On the left-hand side of this inequality we find a new parameter, the ratio of the kinematic viscosity and the circulation quantum ν/κ , which is characteristic for the particular superfluid. For ^3He at $T = 0.5T_c$ we have $\nu = \eta_n/\rho_n \sim 0.4 \text{ cm}^2/\text{s}$ and $\kappa = 0.066 \text{ mm}^2/\text{s}$, so that $\nu/\kappa \sim 10^3$. The inequality is then well satisfied since $\rho_s/\rho_n \sim 1$ and $\alpha \sim 0.5$ for $T = 0.5T_c$. Therefore, the normal component remains at rest in the container frame. Note that in ^4He the situation can be qualitatively different, with the normal component being involved in the motion due to its much smaller viscosity.

The overall evolution of the vortex density can be seen as an interplay of two processes. The first is the turbulent instability in the multiplication region governed by Eq. (43). The second process is the expansion of vortex loops from the multiplication region into the bulk due to the viscous part of the mutual friction force. Equation (44) taken with the *opposite* sign gives thus the rate of vortex-loop-density flow *into the bulk*. In this form, it exactly coincides with the Vinen equation [102] as derived by Schwarz [103], and applies to bulk superfluid turbulence which is continuously sustained by an external source – such as the grid turbulence considered in Refs. [102, 103]. Therefore, the rate at which vortices are supplied into the bulk from the region where they are generated is

$$\dot{L}_{\text{bulk}} = +B\alpha(U - v_0)L^{3/2} = B\alpha(UL^{3/2} - \tilde{\kappa}L^2) . \quad (46)$$

If the supply continues long enough the vortex density in the bulk also saturates at $L_{\text{sat}} = (U/\tilde{\kappa})^2$. The solution [107] describing the relaxation towards saturation for a constant U has the characteristic rate $\tau_b^{-1} = \alpha U^2/2\kappa$. This time increases with decreasing temperature as the parameter α decreases.

4.5. Energy cascades in developed superfluid turbulence

In the previous section we discussed the onset of superfluid turbulence leading to a state which is characterized by a single scale $\ell = \tilde{\kappa}/U$ at which saturation occurs. We call such a single-parameter state the Vinen regime of superfluid turbulence. This turbulent state is very different from the turbulence in classical liquid, where the energy spectrum obeys the celebrated Kolmogorov-Obukhov 5/3-law

$$E_k = C\varepsilon_k^{2/3} k^{-5/3} . \quad (47)$$

Here E_k is the one-dimensional density of the turbulent kinetic energy in the k -space, defined such the the total energy density (in the physical space) E is given by

$$E \equiv \frac{1}{2} \langle |\mathbf{v}|^2 \rangle = \int dk E_k , \quad (48)$$

and ε_k is the energy flux in k -space, which is constant in the inertial range of k where the viscous dissipation can be neglected, $\varepsilon_k = \varepsilon$.

Here we study what is the outcome of the turbulent instability in a superfluid in some regions of Reynolds parameters $\Re = 1/q$ and Re_s . We show that, for big Reynolds number $\Re \gg 1$, the turbulent instability leads to a state of developed turbulence which is closer to its classical analogue: It exhibits a Richardson-like cascade [108] and is thus different from the Vinen turbulent state.

As a starting point we utilize the coarse-grained hydrodynamic equation for the dynamics of the superfluid with distributed vortices in Eq. (16) or, after taking the curl,

$$\frac{\partial \boldsymbol{\omega}_s}{\partial t} = (1 - \alpha') \nabla \times (\mathbf{v}_s \times \boldsymbol{\omega}_s) + \alpha \nabla \times [\hat{\boldsymbol{\omega}}_s \times (\boldsymbol{\omega}_s \times \mathbf{v}_s)] . \quad (49)$$

As we have seen, turbulence develops only if the friction is relatively small compared to the inertial term, *i.e.* when q is below unity. Here we discuss the regime of well developed turbulence which occurs at $\Re = 1/q \gg 1$ when the inertial term is strongly dominating. In this limit, $q \approx \alpha$ while both $\alpha' \ll 1$ and $\alpha \ll 1$. We show that the well developed turbulence can have an analog of Richardson-Kolmogorov cascade, which is modified due to the nonlinear mutual-friction dissipation.

The main difference of this cascade from that in classical liquid is that the dissipation of energy due to mutual friction in Eq.(39) occurs at all scales, and thus the energy flux ε_k must be essentially k -dependent. From Eq.(39) it follows that the energy losses due to dissipation are

$$\frac{\partial E_k}{\partial t} = -\Gamma E_k \quad , \quad \Gamma \sim q\omega_0 \quad , \quad (50)$$

where $\omega_0 = \langle |\boldsymbol{\omega}_s| \rangle$ is the average vorticity. In the steady-state turbulence, these energy losses must be compensated by the energy exchange between different k in the cascade, $\partial \varepsilon_k / \partial k = -\Gamma E_k$. Using the relation between the energy E_k and the energy flux in momentum space ε_k in Eq.(47), which follows from general dimensional reasoning in the spirit of Kolmogorov, one obtains the following balance equation for the flux ε_k :

$$\frac{\partial \varepsilon_k}{\partial k} = -\Gamma \varepsilon_k^{2/3} k^{-5/3} . \quad (51)$$

Such an energy budget equation has been used in [109, 110, 111]; the more complicated version with second derivative [112, 113] was used for superfluid turbulence by Vinen [114]. In the absence of dissipation, *i.e.* at $\Gamma = 0$, Eq. (51) immediately produces the solution with the constant energy flux, $\varepsilon_k = \varepsilon$. Then Eq. (47) turns into Kolmogorov-Obukhov 5/3-law for $E_k \sim \varepsilon^{2/3} k^{-5/3}$.

Equation (51) must be supplemented by a boundary condition: a fixed energy influx into the turbulent system from the large length scale of order of container size, $\varepsilon_{k=1/R} = U^3/R$, where U is the counterflow velocity at this scale. A general solution of Eq. (51) gives the following energy spectrum:

$$E_k = \frac{U^2}{k(kR)^{2/3}} \left[1 + \frac{\gamma}{(kR)^{2/3}} - \gamma \right]^2 , \quad (52)$$

where the dimensionless parameter

$$\gamma = \Gamma R/U = q\omega_0 R/U, \quad (53)$$

and the mean vorticity is expressed through the energy spectrum,

$$\omega_0^2 = \langle |\omega| \rangle^2 \simeq \int_{1/R}^{k_*} dk k^2 E_k. \quad (54)$$

The ultraviolet cut-off k_* in Eq.(54) is determined by the microscopic scale at which the circulation in the k_* -eddy reaches the circulation quantum κ : $v_{k_*}/k_* = \kappa$, and thus the coarse-grained dynamics is no longer applicable. Since $k^2 v_k^2 = E_k$, the cut-off is determined by the spectrum and, as a result, we obtain a closed system of equations which can be analyzed for different regions of the Reynolds parameters, $\Re = 1/q$ and $\text{Re}_s = RU/\kappa$.

Let us consider the turbulent state that corresponds to $q \ll 1$ and $q^2 \text{Re}_s \gg 1$. In this case the parameter γ is close to unity, $1 - \gamma \sim (q^2 \text{Re}_s)^{-1/3} \ll 1$, and the solution (52) has the form

$$E_k \simeq \frac{U^2}{R^2 k^{5/3}} \left[\frac{1}{k^{2/3}} + \frac{1}{k_{cr}^{2/3}} \right]^2. \quad (55)$$

where k_{cr} marks the crossover between the Kolmogorov law at $k > k_{cr}$ to the steeper law $E_k \propto k^{-3}$ at $k < k_{cr}$. Three important scales – the scale $k \sim 1/R$ at which pumping occurs, the crossover scale k_{cr} and the microscopic (quantum) cut-off scale k_* – are well separated in this regime:

$$k_* \sim k_{cr} q^{-3/2} \gg k_{cr} \sim \frac{1}{R} (\text{Re}_s q^2)^{-1/2} \gg \frac{1}{R}. \quad (56)$$

At $q^2 \text{Re}_s \sim 1$ one has $k_{cr} = 1/R$, *i.e.* the region of the k^{-3} spectrum shrinks. Here two scenarios are possible. In the first one the mutual friction is unessential and thus is unable to compensate the Kolmogorov cascade. When the intervortex distance scale is reached the Kolmogorov energy cascade is then transformed to the Kelvin-wave cascade [1] for the isolated vortices. In the second scenario the turbulent state is completely reconstructed and the Vinen state considered in Refs. [102, 103] emerges. This state contains a single scale $\ell = \kappa/U$, and thus no cascade. A possible phase diagram of the turbulent states is shown in Fig. 18. The connection of this phase diagram with the flow states observed in various experiments on superfluid ^4He -II and ^3He -B is discussed in Ref. [115].

These phenomena found in ^3He -B added a new twist to the general theory of turbulence in superfluids which was developed earlier by Vinen [116, 1] and which was based on numerous experiments in superfluid ^4He -II where the first signs of turbulence were observed already in the 1950's [102]. The new theory based on ^3He -B experiments incorporates two Reynolds parameters (the velocity-dependent UR/κ , and the velocity-independent q). It suggests different types of developed superfluid turbulence in different regions of Reynolds parameters, and allows to derive deviations from the classical Kolmogorov-Obukhov scaling law $E(k) \sim k^{-5/3}$.

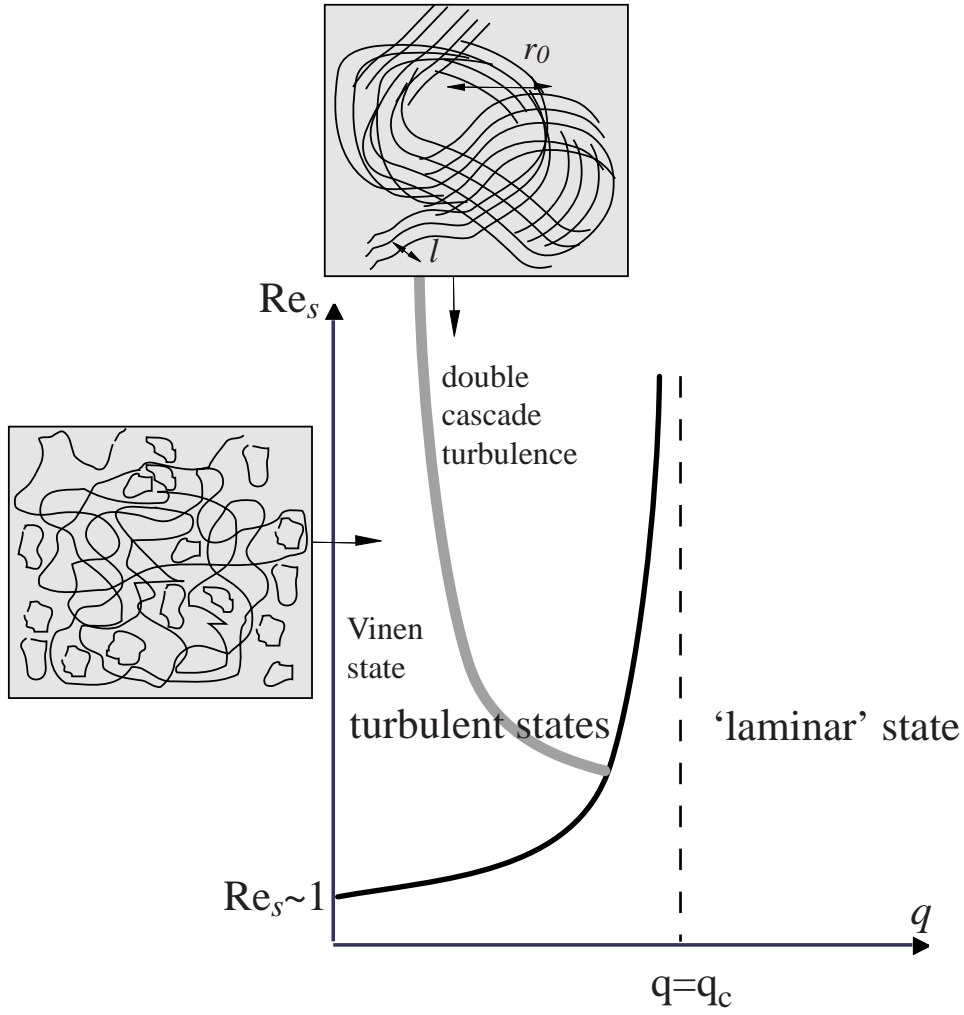


Figure 18. Possible phase diagram of dynamical vortex states in the (Re_s, q) plane. At large flow velocity $\text{Re}_s \gg 1$, *i.e.* well above the Feynman critical velocity, the boundary between turbulent and ‘laminar’ vortex flow approaches the vertical axis $q = q_c \sim 1$. The thick line marks the crossover between two regimes of superfluid turbulence occurring at small q : (i) The developed turbulence of the classical type, which is characterized by two Richardson-type cascades provided by the mutual friction. The Kolmogorov-Obukhov law $E_k \propto k^{-5/3}$ coexists with the $E_k \propto k^{-3}$ law. (ii) The quantum turbulence of the Vinen type at even smaller q , which is characterized by a single length scale $l = \kappa/U$.

The extension of these ideas to the more general case when both the normal and the superfluid components may be turbulent has been done in Ref. [117] on the basis of two-fluid hydrodynamics. The results of this analysis are applicable to superfluid ^4He , where the viscosity of the normal component is much lower than in ^3He , and also in ^4He - ^3He mixtures where, due to presence of ^3He quasiparticles, mutual friction at low temperature is still expected to be significantly higher than in pure superfluid ^4He .

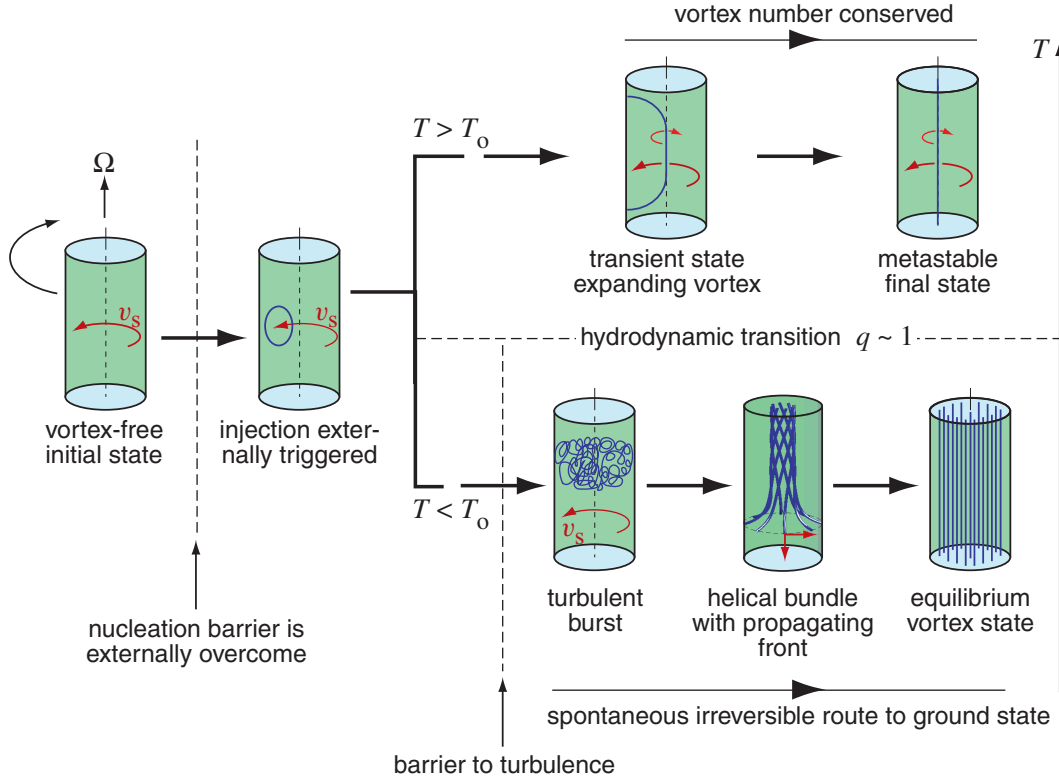


Figure 19. Principle of vortex injection measurements. Different techniques have been explored to inject vortex seed loops in rotating vortex-free flow. One can then as a function of temperature study the evolution of the seeds. Two regimes are found: (1) at high temperatures the vortex number stays constant while (2) at low temperatures a turbulent burst increases the vortex number close to that in the equilibrium vortex state. The exact onset temperature T_0 of turbulence has been found to be sensitive to the details of the injection process. This indicates that the energy barriers of the different processes, which destabilize the seed loops and lead to their turbulent multiplication, depend in addition to temperature also on the number, configuration, and density of the loops.

4.6. Injection of seed vortex loops in applied flow

Why do quantized vortices undergo in applied flow a transition from an organized structure to a disordered tangle? One answer can be given by inspecting the experiment in Fig. 19. Here vortex-free flow is generated by subjecting the superfluid sample to uniform rotation. As long as the resulting maximum counterflow velocity in the sample remains below the limit of spontaneous vortex formation at $v = v_c = \Omega_c R$, the vortex-free state persists. By injecting vortex seed loops in the applied flow the energy barrier for the nucleation of vortices can be externally bypassed. We can then watch as an externally triggered event what happens next. At high temperatures damping is large, vortices cannot flex and support Kelvin waves. There is simply no mechanism for quantized vortices to multiply, to create more new vortices, and to form the equilibrium vortex state with a large number of rectilinear vortex lines.

Below a sudden onset temperature T_0 the situation changes radically: dissipation in vortex motion has dropped to a level where Kelvin wave excitations are not over-damped and helical waves with large amplitude can be formed in flow oriented parallel to the vortex core. The formation of new vortices in dynamic processes becomes possible and suddenly the superfluid can reduce its overall energy state and reach equilibrium.

The injection of vortex seed loops in applied flow is a new feature in turbulence studies which has only become possible in $^3\text{He-B}$ where vortex-free flow can be achieved at sufficiently high flow velocity. With the aid of seed loop injection one can study different instabilities in the vortex dynamics which lead to vortex multiplication. When the number of the vortex lines becomes large enough, the further development of vorticity becomes the collective phenomenon, which can be described either in terms of the Vinen-type theory in Sec. 4.4, the developing superfluid turbulence in Sec. 4.5, or the regular (deterministic) propagation of the vortex front in Sec. 5.

One may expect that the more vortex loops are injected into rotating liquid, the closer is the system to the collective state, and the more universal is the transition to turbulence. In the opposite limit of small number of the injected loops the transition to turbulence becomes less and less universal and more and more irregular being dependent on such details as the number of the injected vortex loops, their shape, location, size, their mutual interaction and interaction of vortices with walls of container, the surface roughness and pinning. This dependence can be investigated using different mechanisms of injections. We explored the following mechanisms.

Magnetically driven $B \rightarrow A$ transition: The most massive number of seed vortices is created by sweeping up the barrier field H_b in the setup of Fig. 7. The field sweep is conducted in rotation at constant temperature, when the entire sample is in B phase and vortex free. When the field reaches some slightly hysteretic value above $H_{AB}(T, P)$ over a short section in the middle of the long sample, then the A phase, its vortices, and two A-B interfaces are all formed essentially simultaneously. A detailed explanation how this happens has not been worked out, but depending on whether the rotation velocity Ω exceeds the critical KH velocity $\Omega_{cKH}(T, P)$ or not, all or only some A phase vortices leak into the B-phase sections. Presumably, if $\Omega > \Omega_{cKH}$, the A-B interface is not stable while it is formed until the difference in counterflow velocity across the interface is very low and practically all vortices cross the A-B interface. In the regime $\Omega < \Omega_{cKH}$, the relative number of those vortices crossing the interface has not been firmly established. In both cases the end result is that a large number of vortices is suddenly injected at the same moment in both B-phase sections which lie outside the barrier field.

Kelvin-Helmholtz instability: The Kelvin-Helmholtz instability of the A-B interface, discussed in Secs. 4.2 and 3.6, is so far the most effective, well-controlled and reproducible of the available vortex-injection mechanisms. The injection is carried out at constant external conditions while the rotation velocity Ω is suddenly incrementally increased by $\Delta\Omega \approx 0.05 \text{ rad/s}$ across the critical value $\Omega_{cKH}(T, P)$. At temperatures above T_0 such an injection generates a limited number of vortices in the B phase and consequently the staircase pattern in Fig. 11 can be displayed by triggering multiple

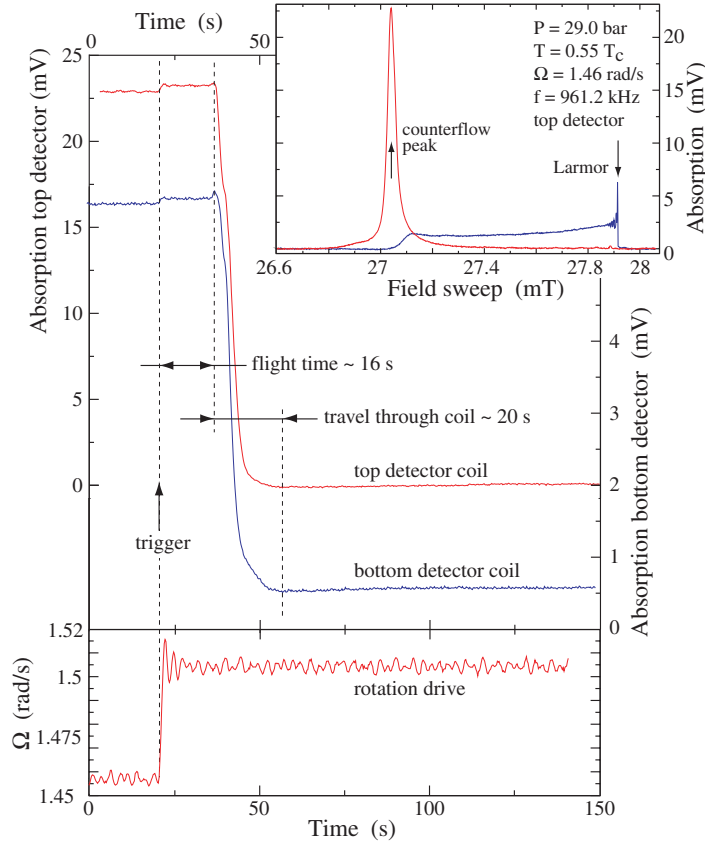


Figure 20. NMR measurement of KH instability in the turbulent temperature regime. (*Top right panel*) NMR absorption line shapes in $^3\text{He-B}$. The initial state displays a large maximum which is shifted from the Larmor position by a temperature dependent amount. The height of this counterflow peak is roughly proportional to the counterflow velocity. The final equilibrium vortex state has a flat distribution of absorption. At fixed temperature the integrated absorption under the two line shapes is equal. (*Main panel*) Counterflow peak height measured as a function of time, when the KH instability is triggered in the setup of Fig. 7 (with $I_b = 8.0$ A). The seed loop injection at the A-B interface is followed by a turbulent burst, rapid polarization, and the forming of a propagating vortex cluster. After a temperature dependent flight time the front of the cluster reaches the closer end of the detector coil. While the front travels through the coil, the peak height decreases and reaches zero when the rear of the front leaves the far end of the detector coil. Since the measuring setup in Fig. 7 is symmetric, the top and bottom detector coils display identical responses. (*Bottom panel*) Externally controlled trigger for KH injection. The rotation drive is suddenly increased by $\Delta\Omega \approx 0.05$ rad/s so that Ω jumps above the critical velocity of $\Omega_{\text{cKH}} = 1.48$ rad/s. This is signalled as an incremental increase in the counterflow peak heights of both signals in the main panel.

instability events. Below T_0 the staircase pattern is not obtained, since already the very first injection sends the sample in the equilibrium state and removes essentially all applied counterflow. The measured signature from the injection in the turbulent temperature regime is shown in Fig. 20. The radical difference from Fig. 11 is evident:

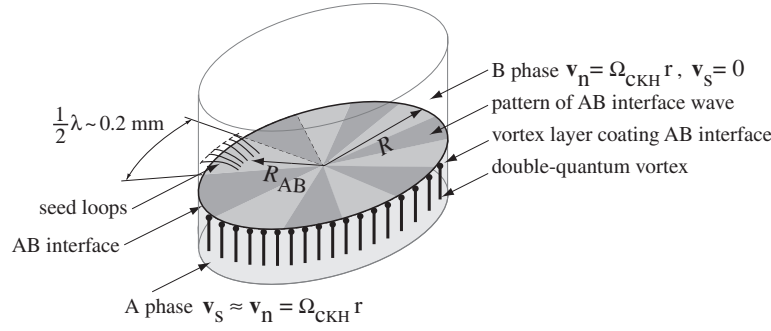


Figure 21. Initial vortex loop configuration on the B phase side of the A-B interface, following a KH instability in a rotating cylinder. A section of the cylindrical two-phase sample is shown. Roughly the equilibrium number of double-quantum vortices exists on the A phase side. The B phase is vortex free, except for the seed loops. At the A-B interface the A-phase vortices curve into a surface layer which coats the A-B interface on the A-phase side. In this layer the vortices run radially out to the cylinder wall [58]. In the KH instability the vortices in the deepest trough of the interface wave are tossed on the B-phase side. These become the seed vortex loops in the B-phase flow. They are oriented radially in the cylinder and extend from the A-B interface at $R_{AB} \approx 2.6 \text{ mm}$ to the cylinder wall at $R = 3 \text{ mm}$. Originally the vortex quanta are roughly aligned parallel at an inter-vortex spacing of $\sim 3 \xi_D \approx 60 \mu\text{m}$. In the turbulent temperature regime these loops are rapidly destabilized by Kelvin wave excitations, owing to the applied flow $\mathbf{v} = \mathbf{v}_n - \mathbf{v}_s = \boldsymbol{\Omega} \times \mathbf{r}$ and the interactions between the loops.

The dynamic formation of new vortices in a turbulent burst increases the vortex number immediately to N_{eq} .

The evolution following a triggered injection event can be monitored by recording the NMR absorption height as a function of time either at the location of the counterflow peak, as is done in Fig. 20 to measure the removal of the macroscopic counterflow, or in the region of the Larmor edge, as is done in Fig. 11 to exhibit a signal which is generated more directly by the vortices. In both regions the NMR line shape arises from the interplay of vortex-free counterflow and of vortices via their orientational influence on the order parameter texture, as explained in the Appendix.

The principal new information in Fig. 20 is related to the motion of the vortices after the turbulent burst. From the time interval between the trigger and the first response from the propagating vortex front one can measure the longitudinal velocity of the vortices [118]. It is found to be approximately $v_z = \alpha \Omega R$. The time interval during which the macroscopic counterflow disappears from the coil is a convolution of the moving vortex front with certain width through a detector coil of given length. We define the width of the front as that part of the propagating vortex structure where both the number of vortices and their polarization increase from zero to the final full values, which closely correspond to that of the equilibrium vortex state number $N_{\text{eq}} \approx 2\pi R^2 \Omega / \kappa$. These features are related to the structure of the front and the helical vortex cluster behind it. They will be discussed in Sec. 5. We note here that the response in Fig. 20

is deterministic and fully reproducible from one measurement to the next, in spite of the fact that it involves a short-lived stochastic turbulent burst. The reproducibility is attributed to the well-behaved value of the KH critical rotation velocity $\Omega_{\text{cKH}}(T, P)$ plus to the fact that the propagation of the cluster along the rotating column is a deterministic process and one which controls the slow time scale in Fig. 20.

KH injection produces the highest onset temperature T_o . The reason is interpreted to be the configuration in which the seed vortices end up on the B-phase side of the interface: As sketched in Fig. 21, they form a tight bundle of roughly parallel vortex loops with an inter-vortex spacing of $\sim 3\xi_D$ (Fig. 21). Here many curved seed vortices are packed close together. In the applied B-phase flow they start interacting and become unstable, if the amplitudes of Kelvin wave excitations are not critically damped at $T < T_o$. This leads instantaneously to a turbulent burst below T_o .

Neutron absorption: The nuclear capture reaction of a thermal neutron by a ^3He nucleus provides an externally controllable mechanism for vortex line injection in vortex-free flow of ^3He -B [3]. A thermal neutron incident on liquid ^3He has a short mean absorption length of only $\sim 0.1\mu\text{m}$ before it suffers the capture reaction $n+^3\text{He} \rightarrow p+^3\text{H}+764\text{keV}$. The reaction energy is released in the form of the kinetic energy of the two reaction products. It is dissipated by them in ionizations within a volume of radius $\lesssim 50\mu\text{m}$ around the reaction site. As a result, roughly this volume of the fluid, which we call the neutron bubble, is locally heated above T_c . Within microseconds it cools back to the ambient bath temperature, but a random vortex tangle is left behind [119]. In the absence of flow the vortex loops in the tangle shrink and disappear, but in vortex-free rotation the largest loops with proper orientation and polarization are extracted from the tangle and expand to vortices of the bulk fluid.

The extraction of rings from the tangle is governed by the magnitude of the applied vortex-free flow velocity v according to the well-known formula for the equilibrium state of a vortex ring: A ring of radius r is in stable state at the flow velocity

$$v(r) = \frac{\kappa}{4\pi r} \ln \frac{r}{\xi}. \quad (57)$$

A ring with larger radius than $r(v)$ will expand in the flow while a smaller will contract. Therefore a minimum threshold velocity v_{cn} exists at which the first vortex ring can be extracted from the tangle. This velocity corresponds to the maximum possible ring size, which has the radius R_b of the neutron bubble: $r(v_{\text{cn}}) \sim R_b$. At larger flow velocities smaller rings can be pulled from the tangle. Simultaneously the number of such smaller rings can be larger than one, since several smaller rings can fit within the neutron bubble. Again there exists a minimum threshold velocity v_{cni} which is required in order to extract i rings of equal size from the bubble. Their number i is obtained from a volume argument, *i.e.* according to how many spheres of radius $r(v)$ can fit inside the neutron bubble without overlap: $i \approx (R_b/r(v))^3$. Using Eq. (57) we then obtain $v_{\text{cni}} \sim i^{1/3} v_{\text{cn}}$. A better experimental and theoretical justification of these features can be found in Ref. [3].

Thus a neutron absorption event can be used to inject vortex rings in the rotating

flow. The number and size of these rings depends on the local velocity of flow. Since the mean absorption length is only $\sim 100\ \mu\text{m}$ and the flow velocity increases with radius as $v = \Omega r$, all rings will initially be located in the vicinity of the outer wall at a well-defined flow velocity $v = \Omega R$. In this situation neutron absorption becomes an externally controllable injection method. However, because of the random tangle from which the injected rings originate, vortex formation from a neutron absorption event is by nature a stochastic process. This means that at a flow velocity $\Omega R \gtrsim v_{\text{cni}}$ the number of rings obtained from a given neutron absorption event can be anything from zero up to the maximum limit i . At high temperatures $T > T_o$, each extracted ring evolves independently to a rectilinear vortex line. These can be individually counted in similar fashion as in Fig. 11.

In the turbulent temperature regime either no vortices are obtained or, if even one ring is extracted from the tangle, the event leads to dynamic vortex formation and a turbulent burst. By choosing the value of the applied flow velocity ΩR in relation to the threshold velocity v_{cni} measured at $T > T_o$, we can study the onset T_o as a function of the number of rings i which are left over from a single neutron absorption event. Of particular interest is to check whether with $\Omega R \gtrsim v_{\text{cn}}$ a single vortex ring can lead to a turbulent burst. In practice, because of the small size of the neutron bubble, $R_b \lesssim 50\ \mu\text{m}$, the applied flow velocity for vortex injection via a neutron absorption event has to be relatively high: $\Omega_{\text{cn}} = v_{\text{cn}}/R \gtrsim 1.4\ \text{rad/s}$.

There are also other types of “injection”, where a small number of vortices are involved. Vortex multiplication can, for example, be initiated by a remnant vortex from a preceding experimental run (which has not had sufficient time to reach the container wall and annihilate there), or curved vortex loops which might be present due to the misalignment between the rotation axis and the symmetry axis of the cylinder. However, the common feature of all the results of experiments with different injection mechanisms is that the vortex multiplication and the onset of the turbulence are governed by the parameter q , though the critical value q_c may depend on the mechanism of the injection.

It was also found both from experiments and numerical simulations that, at low q , injecting even a single vortex loop into the external flow can lead to turbulence. Based on the simulations it seems that in the single-vortex regime, where the vortex-vortex interactions can be neglected, the most important scenario for generating a new vortex seems to involve a reconnection with a wall. This is illustrated in Fig. 22, which shows a vortex ring interacting with a plane boundary. Reconnection with the boundary induces helical Kelvin waves on the vortex that due to finite temperature are damped in the absence of external flow. However, under applied counterflow a Kelvin wave with correct helicity and proper orientation may begin to expand. This expanding loop can then reconnect again with the boundary, leading to the generation of a new loop [120].

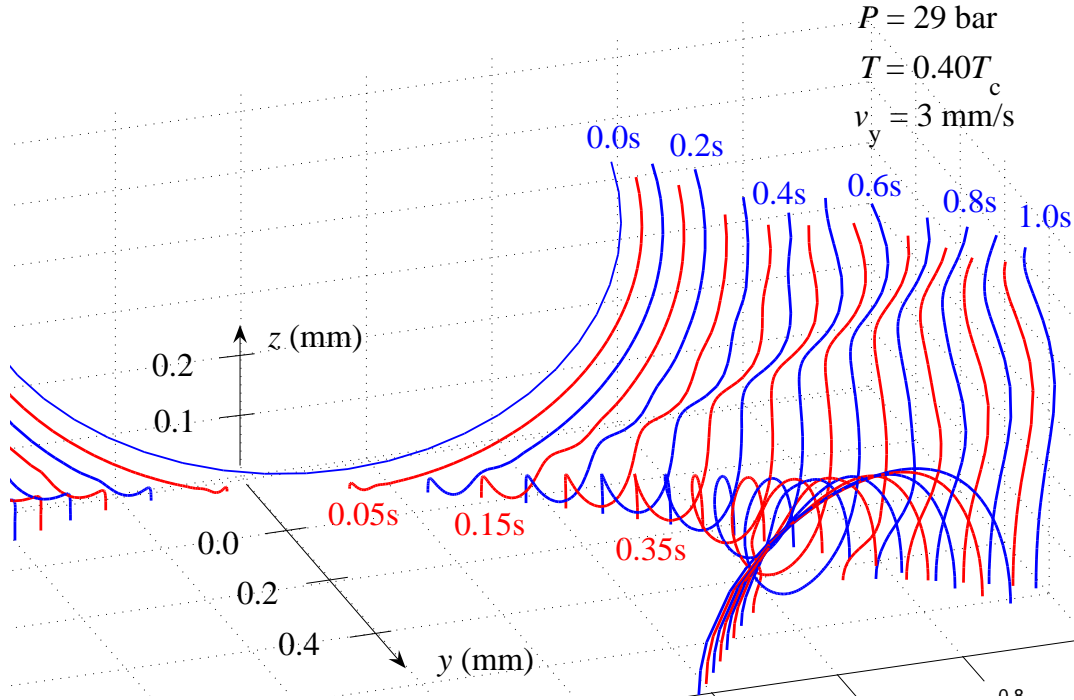


Figure 22. Principle of the boundary induced instability. A vortex ring with radius of 0.5 mm reconnecting with the plane under constant external normal fluid velocity. Initially the center of the ring is 0.5 mm above the boundary and the plane of the ring is slightly tilted (angle of $\pi/10$) around the normal of the plane and also towards the plane. Temperature $T = 0.40T_c$ ($q = 0.21$) and the normal fluid velocity $v_n = 3$ mm/s along y-direction. Reconnection creates kinks on the vortex and the other one on the right has the correct orientation and helicity and therefore it starts to grow under external flow. The kink grows and reconnects to the boundary creating a new vortex.

5. Propagating vortex front and twisted vortex state

5.1. Introduction

In the rotating container, the multiplication of vortices injected into the initial Landau vortex-free state and the following superfluid vortex turbulence are transient phenomena which finally lead to the establishment of the stable equilibrium vortex state which imitates the solid-body rotation of the superfluid component. In the geometry of a long cylinder, the propagation of vorticity from the region where the vortex multiplication first takes place to the metastable Landau state acquires new features.

Consider a long rotating superfluid column initially in a metastable vortex-free state of high kinetic energy: the superfluid component at rest, and the normal component in solid-body rotation. If then close to the equilibrium number of vortices is suddenly created locally in one part of the sample, how does the vorticity spread over the rest of the sample to reach stable equilibrium? In other words, how is the initially stationary superfluid component dragged into rotation? To shed light on this new hydrodynamic

problem, we discuss here an experiment where vortex propagation in superfluid $^3\text{He-B}$ is studied by monitoring the NMR signal as a function of time, at a location which is far away from the injection site.

As already discussed in the preceding chapter, the dynamics of the quantized vortex lines in $^3\text{He-B}$ is strongly influenced by the strength of the mutual-friction force imposed by the normal component. This force actually drives the injected vortices along the rotating superfluid column, and is responsible for dissipating the excess kinetic energy stored in the initial metastable rotating state. Moreover, as the frictional damping decreases below a threshold value attained at the temperature of approximately $0.6 T_c$, vortex motion was observed to undergo a transition from vortex-number conserving to turbulent.

With this in mind, it initially came as a surprise that neither our numerical simulations or experimental work show any evidence of turbulent behavior. In fact, even under the conditions of fairly low damping (at the temperature of $\approx 0.4 T_c$), the injected vorticity does not spread in the form of an incoherent tangle. Instead, the vortices propagate along the sample in a nearly time-invariant configuration lead by a narrow *vortex front*. Moreover, the propagating line vortices turn out to form a *helically twisted* configuration [121]. This novel dynamic state of topological defects arises as a consequence of the motion of the vortex front which, in addition to the axial propagation, also has an azimuthal component with respect to the frame of the container. The twisted vortex state can be identified through its associated superfluid velocity field which has a component along the rotation axis and leaves a clear fingerprint to the NMR signals. Both of these new features, vortex front and twisted vorticity, are also exhibited by numerical simulations.

5.2. Basic features of the NMR response from propagating vortices

We begin by examining the NMR signals from the vortex-injection experiment with the Kelvin-Helmholtz technique (discussed in Sec. 4.6) in some more detail. As described in the previous section, vortex injection into originally vortex-free flow at low enough temperatures leads to a turbulent burst, where the number of vortex lines locally increases close to N_{eq} in a rapid fashion. After the burst the created vortices begin to propagate along the rotating superfluid column, gradually replacing the sample volume in the metastable vortex-free state of large rotational counterflow with vorticity. Figure 23 shows the measured NMR signals as a function of time, as recorded by a spectrometer located at a distance of ~ 4 cm from the injection site (A-B phase boundary).

The NMR data in Fig. 23 consists of the absorption time traces at two different frequencies, corresponding to two distinct maxima in the full NMR lineshape. The relative amount of absorption concentrated at these peaks is a useful measure of azimuthal counterflow and, consequently, of local superfluid vorticity: if the counterflow is small, an absorption peak forms near the Larmor frequency, whereas in situations with

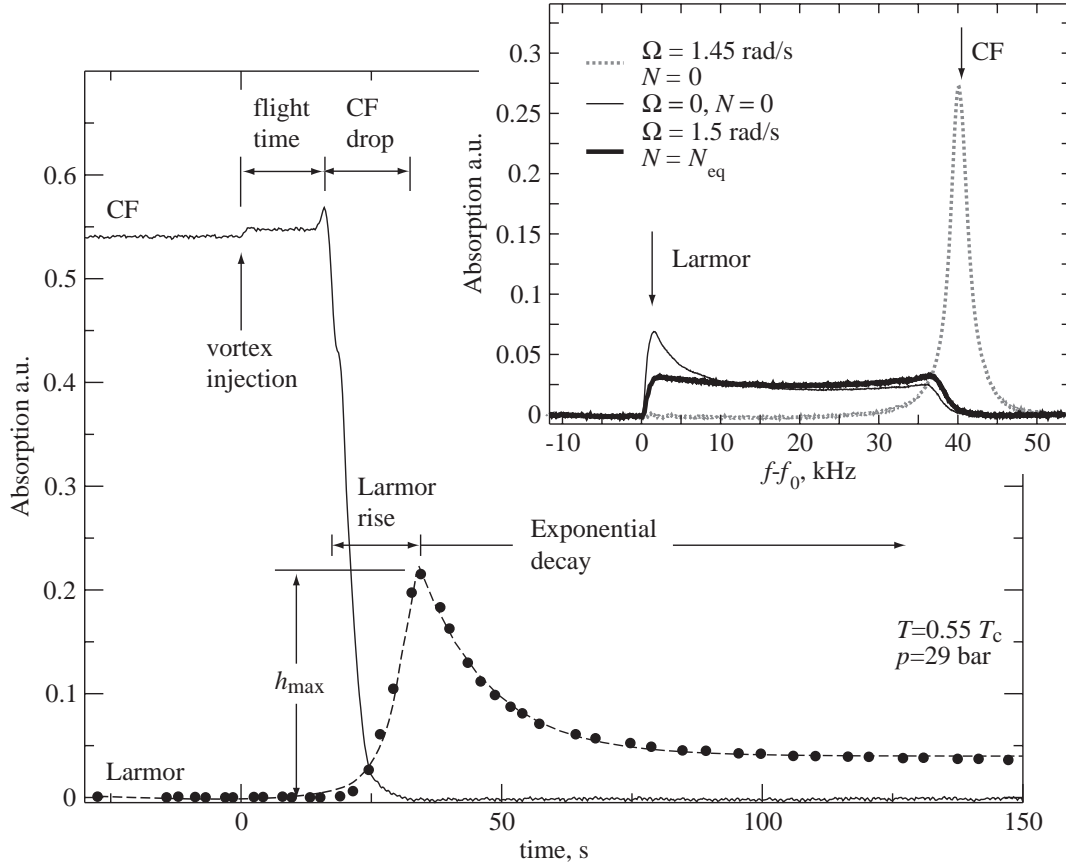


Figure 23. The measured sequence of NMR absorption signals after KH injection of vortex loops into vortex-free flow. The time sequence shows two different measurement traces: absorption at the counterflow peak (CF) and absorption at a maximum close to the Larmor edge of the NMR signal (Larmor). The corresponding frequency shifts are pointed out with arrows in the NMR absorption spectra in the insert. The Larmor signal is recorded with the bottom spectrometer and the CF signal with the top spectrometer so that they are not exactly comparable in amplitudes. Here the amplitudes are normalized such that the integral over the absorption spectrum is unity. The spectra in the insert are measured with the bottom spectrometer as a function of the NMR field which here has been converted to frequency shift. The Larmor region is recorded by sweeping the NMR field linearly back and forth in a narrow interval and by plotting out the peak height of the maximum. The NMR field of this maximum is not exactly constant during the time when the Larmor absorption is time dependent (\bullet). The CF signal is recorded at fixed NMR field. In this example vortex free rotation is first established at 1.45 rad/s. Vortex injection is triggered by a small increase of 0.05 rad/s in the rotation speed. The increased flow is seen as a small step increase in the CF signal. At the injection moment a few vortex loops cross the phase boundary, undergo a burst of turbulence, and start to move towards the detectors at both ends of the sample volume. No change in the signal is seen until the vortex front reaches the closest end of the detector coil. This is the flight time. Once the vorticity reaches the coil the CF signal reduces rapidly indicating the removal of azimuthal counterflow. Following this, the Larmor signal rises to a maximum h_{\max} and then decays exponentially.

large counterflow most of the absorption collects at another, slightly higher frequency, and defines the so-called counterflow peak (see the insert of Fig. 23). In other words, the heights of the Larmor peak and the counterflow peak (marked CF in the figure) are recorded as a function of time in the experiment. Actually, in the precise setup shown in Fig. 7 the two peaks are being monitored by two independent spectrometers located near the opposite ends of the cylindrical sample. Even though the NMR traces then refer to different, disconnected sets of propagating vortices, they are expected to show similar behavior due to the symmetry of the setup (the distances separating the NMR coil from the phase boundary are identical for both halves).

In the beginning of the experiment, the B-phase volume contains no vortices and is in a state of high counterflow at $\Omega = 1.45$ rad/s: a large CF signal is then visible, whereas in the Larmor region there is very little absorption. At time $t = 0$, the angular velocity is suddenly increased to 1.5 rad/s (seen as a small increase in the CF peak height), above the KH critical velocity which is set between 1.45 and 1.5 rad/s with the barrier magnetic field. At this moment, vortices are injected into the B phase and, after a short period of turbulent vortex multiplication, begin to propagate towards the NMR coils. After a temperature-dependent flight time (approximately 20 s in the conditions of the experiment shown in Fig. 23) the vortices arrive at the coils, which is signalled by a rapid decrease in the measured azimuthal counterflow (the disappearance of the CF signal). Simultaneously, the peak height of the Larmor signal increases, reaches a maximum, and then slowly relaxes to the value corresponding to the equilibrium NMR spectrum from rectilinear vortex lines.

Two interesting conclusions can be immediately drawn from the data in Fig. 23. First, the fact that after the vorticity arrives at the NMR coil the counterflow signal drops rapidly from its initial maximum value to essentially zero clearly indicates that the propagating vortices form a relatively narrow front, which separates the vortex-free region from the region occupied by vortices. Similar behavior is observed also in numerical simulations of propagating vortices, as shown below in Sec. 5.6.

Another interesting feature has to do with the Larmor signal, and its non-monotonic time dependence. The transient overshoot of the Larmor-peak height appreciably above the equilibrium-state value is especially noteworthy. Such a response cannot be obtained with any of the metastable vortex configurations consisting entirely of rectilinear lines. Instead, we argue that this is a fingerprint of the helical twisting acquired by the propagating vortices. In the following, we discuss this aspect in more detail and demonstrate how both numerically calculated NMR spectra for twisted vorticity and detailed simulations of vortex motion support this interpretation.

5.3. Formation of a helically twisted vortex cluster

In order to understand the new NMR features discussed above it is instructive to begin by studying the motion of a single vortex loop in rotating flow. Consider the instantaneous velocity of the vortex-line element at the point where the line connects

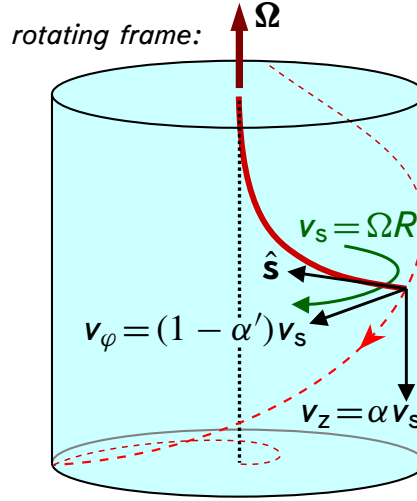


Figure 24. The motion of a single vortex loop in a rotating cylinder. If viewed in the frame rotating with the container, the end of the loop that connects to the side wall moves with a velocity that has both an azimuthal as well as an axial component. Therefore, the plane of the loop rotates while the vortex expands in the rotating flow.

to the cylindrical side wall. In the rotating frame, the normal velocity at the element vanishes, while the local superfluid velocity is $\mathbf{v}_s = -\Omega R \hat{\phi}$ (here we ignore the small self-induced contribution from the curvature of the loop). From Eq. (9), one then finds the velocity of the element as

$$\mathbf{v}_L = -(1 - \alpha')\Omega R \hat{\phi} - \alpha\Omega R \hat{z}, \quad (58)$$

i.e. the vortex end has both azimuthal and vertical velocity components, see Fig. 24. From this, we immediately find that the expansion time, or the “time of flight” which is required for the single curved vortex to advance an axial distance d along the rotating column, is $d/(\alpha\Omega R)$. Combined with this, the azimuthal velocity gives rise to a spiralling motion where the plane of the loop is constantly turning during its expansion.

Consider next the situation with a large number of loops (close to N_{eq}) like that in Fig. 24: one end connecting to the top plate, and the other to the side wall. The local superfluid velocity at any element on one of these loops is then modified by the contribution induced by the other vortices. In particular, the vortex segments at the top plate would be expected to have $\mathbf{v}_s \approx \mathbf{v}_n$, and be in solid-body rotation with the container. Hence the azimuthal counterflow experienced by the vortex elements changes from zero to $\sim \Omega r$ over the volume occupied by vortices. On the other hand, both numerical simulations and experimental data (see below for more details) indicate that the flight times for a cluster of vortices remains almost unchanged (not differing by more than 10-15 %) from the single-vortex value. The combined effect of these two motions is to drive the vortex cluster into a helically twisted configuration, as shown schematically in Fig. 25. Estimating $(1 - \alpha')\Omega$ as the angular velocity of azimuthal motion, and taking $\alpha\Omega R$ for the axial velocity, we arrive at the approximate value $k \sim (qR)^{-1}$ for the wave number of this distribution.

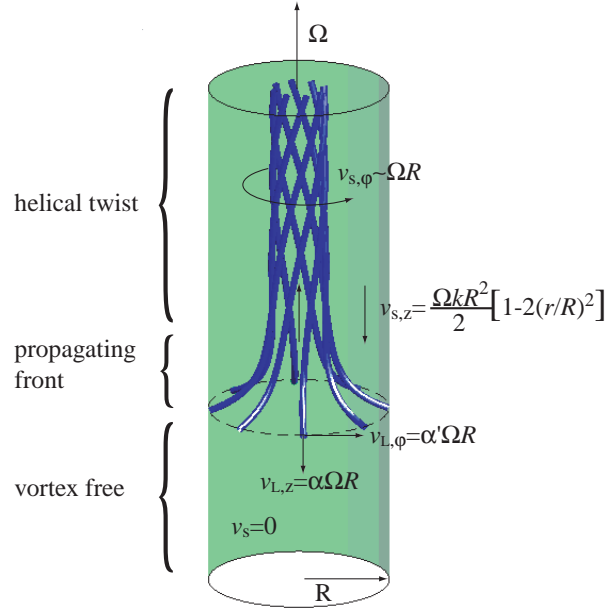


Figure 25. The vortex front propagates along the rotating column into the vortex free counterflow with the velocity $v_{L,z} = \alpha \Omega R$. In the NMR signal the front is seen as a disappearance of the counterflow signal and as an increase in the signal in the Larmor region of the spectrum. Behind the front the number of vortex lines is close to equilibrium and the superfluid mimics, in azimuthal direction, solid body rotation. Since the lines at the cylinder wall also move in the azimuthal direction with the velocity $v_{L,\phi} = \alpha' \Omega R$ the front leaves behind a helical twist. The twist gives rise to superflow in the z -direction $v_{s,z}$ such that at the center of the cylinder there is an upward flow and close to the wall a downward flow (the case in the figure where the front propagates down). The helical twist with its z -directional flow is seen as an overshoot of the signal in the Larmor region of the spectrum and the relaxation of the twist is seen as the exponential decay. The velocities in this figure are marked as viewed from the inertial laboratory frame.

For a more extended discussion of the formation and general properties of the twisted vortex state see Ref. [121]. Most importantly, however, the helical structure implies superflow in the axial direction which, as we now proceed to discuss, explains the peculiar excess NMR absorption near the Larmor frequency observed in the experiments.

5.4. Superflow field of the twisted cluster: model of uniform twisting

We will now construct a theoretical model for the superfluid-velocity profile connected with the twisted vortex state. This is achieved by noting that the equation of motion for superfluid hydrodynamics, Eq. (16), allows for stationary ($\partial \mathbf{v}_s / \partial t = 0$) solutions corresponding to twisted vorticity. The simplest one of these is translationally invariant along the axial (z) direction, of the form

$$\mathbf{v}_s = v_\phi(r) \hat{\phi} + v_z(r) \hat{z}, \quad (59)$$

and corresponds to a situation where the wave vector k of the twisting is independent of the radial coordinate r , or

$$\frac{\omega_\phi}{\omega_z} = kr. \quad (60)$$

Here $\boldsymbol{\omega}_s = \omega_\phi \hat{\boldsymbol{\phi}} + \omega_z \hat{\mathbf{z}}$ is the local coarse-grained superfluid vorticity. The condition (60) simply means that in the case of uniform twisting the azimuthal tilt of the vortices has to increase with the radial distance from the cylinder axis. In addition, we impose a further condition for \mathbf{v}_s by requiring that the mutual-friction-induced force on the vortices vanishes, *i.e.*

$$\boldsymbol{\omega}_s \times (\mathbf{v}_s - \mathbf{v}_n) = 0, \quad (61)$$

meaning that the vortices are aligned parallel to the counterflow. An equivalent condition would be to require that radial vortex motion is absent: $v_{L,r} = 0$ from Eq. (9). Under these requirements, the superfluid velocity field can be solved as

$$\begin{aligned} v_\phi(r) &= \frac{\Omega r + (kr)v_0}{1 + (kr)^2}, \\ v_z(r) &= \frac{v_0 - (kr)\Omega r}{1 + (kr)^2}. \end{aligned} \quad (62)$$

The parameter v_0 is fixed to the value $v_0 = (\Omega/k)\{(kR)^2/\ln[1 + (kR)^2] - 1\}$ by further requiring that the net flow through a cross section of the cylinder vanishes.

The NMR response corresponding to a twisted vortex state having a flow profile like that in Eq. (62) can be roughly understood in terms of the following simple arguments. The local resonance frequency depends on the orientation of the B phase order parameter which, in turn, is affected by the magnitude – and orientation – of the local counterflow velocity. This can be described in terms of a free-energy contribution which has the form $-[\hat{\mathbf{l}}_B \cdot (\mathbf{v}_n - \mathbf{v}_s)]^2$, where $\hat{\mathbf{l}}_B = [-\hat{\mathbf{z}} + 5(\hat{\mathbf{z}} \cdot \hat{\mathbf{n}})\hat{\mathbf{n}} + \sqrt{15}(\hat{\mathbf{z}} \times \hat{\mathbf{n}})]/4$ is the orbital anisotropy axis (in the presence of an axial magnetic field) corresponding to the order-parameter vector $\hat{\mathbf{n}}$. Therefore, counterflow along the cylinder axis should have a tendency to favour the orientation $\hat{\mathbf{l}}_B \parallel \hat{\mathbf{n}} \parallel \hat{\mathbf{z}}$. This in turn corresponds to additional NMR absorption at the Larmor frequency, as observed in the experiments. As shown below in Sec. 5.5, these arguments are supported by more detailed investigations on the order-parameter textures associated with flow profiles having the form of Eq. (62).

5.5. Further experimental results on twisted vorticity

Next we turn to some more detailed experimental investigations on the propagating vortices and twisted vortex state. First, Fig. 26 shows the measured results on the flight time of propagating vortices as a function of temperature. In the experiments, the Kelvin-Helmholtz instability is triggered and the time t_{flight} needed for the vortex lines to reach the pick-up coil (a known distance d away) is recorded. The data has been

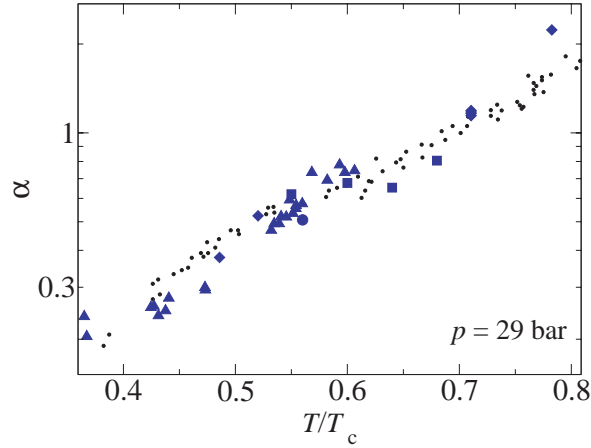


Figure 26. The dissipative mutual friction coefficient α , plotted on a logarithmic scale as a function of temperature. It is determined from the axial flight time, assuming $v_{L,z} = \alpha\Omega R$, regardless of the number of vortex lines in the front. We use flight time data from our measurements to extract $\alpha = d/(t_{\text{flight}}\Omega R)$ where d is the distance the vortex lines have travelled, and compare this with the data from Ref. [64] (●). The different types of symbols correspond to different methods of determining the flight time (for details see [118]). The data marked (▲) is measured using the method explained in Fig. 23. Since the agreement in α values between these two sets of data is well within the accuracy of both measurements we conclude that the model for the flight time is justified.

presented in terms of the mutual-friction parameter α , as extracted from the relation $\alpha = d/(t_{\text{flight}}\Omega R)$, which is based on the assumption that the vortices propagate with axial speed $\alpha\Omega R$. The degree of validity of this assumption can be assessed by comparing to the previously published data of $\alpha(T)$ from Ref. [64].

Because of the previously discussed division to laminar and turbulent regimes of vortex dynamics, slightly different experimental procedures were followed in order to achieve as similar initial conditions for the measurements as possible. In the low-temperature (low damping) regime, $T \lesssim 0.6T_c$, any vortex injection always initiates turbulent vortex formation, where close to the equilibrium number of vortices ($N \approx N_{\text{eq}}$) is rapidly created. However, a different procedure is needed in the laminar regime at temperatures above $0.6T_c$, where such multiplication does not occur. Close to the equilibrium number of vortices can then be secured with the Kelvin-Helmholtz method by first rotating the sample at high $\Omega \sim 2.5$ rad/s (well above the KH critical velocity) entirely in the B phase before switching on the barrier field that creates the A-phase region in the middle of the cell. When the A phase is then formed, the A-B interfaces go immediately unstable, transferring a large amount of vortices into the surrounding B phase.

As already mentioned above, the most prominent new feature of the twisted vortex state is the extra NMR absorption in the vicinity of the Larmor frequency. A quantitative measure of this effect is the maximum peak height of the resonance

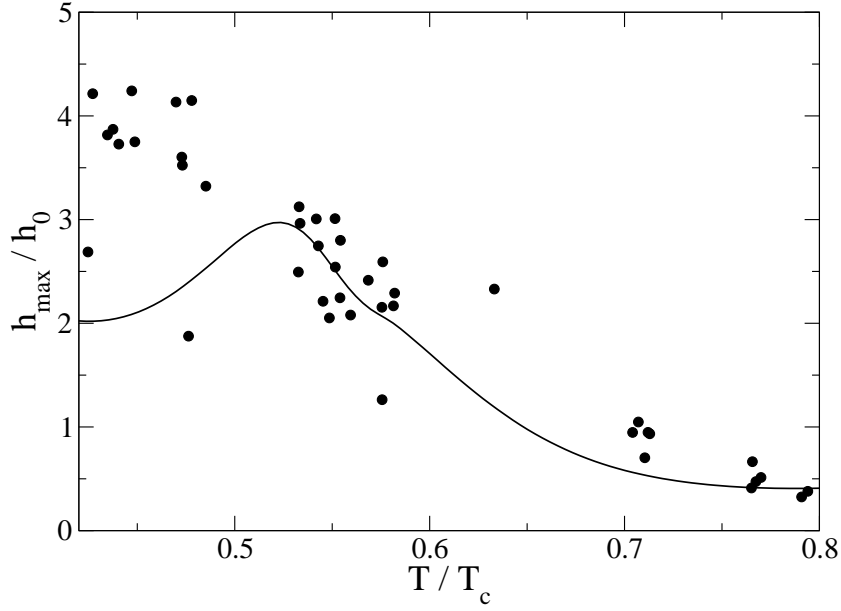


Figure 27. The amplitude of the maximum Larmor overshoot h_{\max} , divided by the maximum h_0 of the absorption spectrum without rotation $\Omega = 0$, plotted as a function of temperature. The solid line shows the corresponding quantity from numerically calculated NMR absorption spectra, using the uniform-twist model with $kR = 1/q$.

line during the transient time evolution, represented with the symbol h_{\max} in Fig. 23. Figure 27 shows the dependence of this maximum peak height on temperature, as normalized to the peak height h_0 of the NMR spectrum measured without rotation ($\Omega = 0$). The solid line in the figure represents the corresponding quantity obtained from numerically calculated NMR lineshapes. In these calculations, the equilibrium order-parameter distributions were determined by minimizing the textural free energy in the presence of superflow having the form of the uniform-twist model, Eq. (62). The wave vector of the twist was chosen as $k = 1/(qR)$ (see discussion in Sec. 5.3). Towards low temperatures the temperature dependence of the Larmor overshoot is seen to reflect the exponential growth of $q^{-1}(T)$: the twisting is tighter, leading to an increased superfluid velocity in the axial direction, and hence to excess absorption near the Larmor frequency. Furthermore, the dependence of the overshoot on the angular velocity Ω is presented in Fig. 28.

Taking into account the fact that the calculations performed to obtain the theoretical curves in Figs. 27 and 28 contain no adjustable parameter, the agreement between experiment and theory should be considered as remarkably good. In particular, the clearly identifiable fingerprint of the measured NMR signals during vortex propagation – large excess absorption near the Larmor frequency – can be explained by assuming that the propagating vortices form a helically twisted cluster. Therefore, these studies constitute the first experimental observation of a new dynamical state of topological defects in a superfluid system. In the following section we will

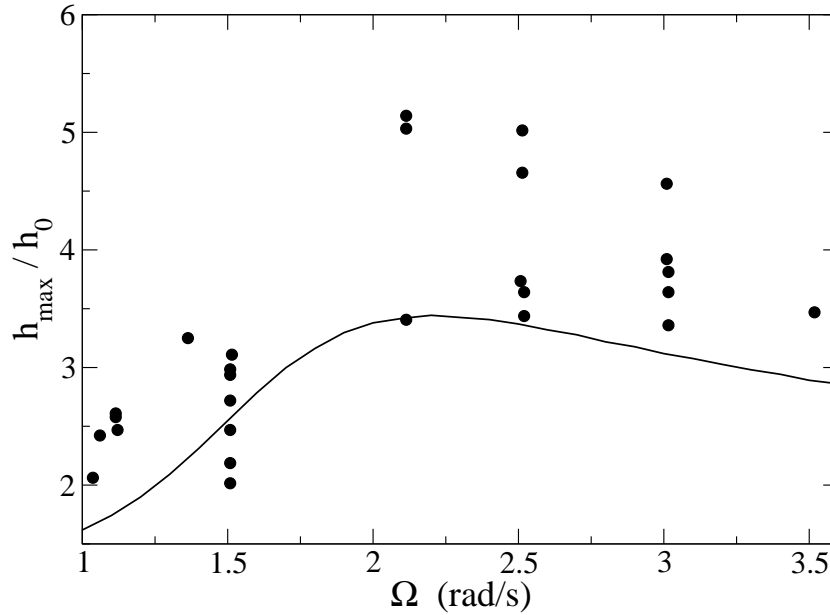


Figure 28. The amplitude of the maximum overshoot divided by the maximum of the $\Omega = 0$ spectrum as a function of Ω . The solid line is the theoretical prediction of the uniform-twist model with $kR = 1/q$.

describe detailed numerical simulations on the propagation of vortices; they will provide additional justification both for the formation of the vortex front, as well as the helical twisting of the vortices.

5.6. Propagating vortex front in simulations

Our numerical simulations were performed using the vortex filament model where vortices are considered as simple linear objects. The local superfluid velocity at individual vortex segments was calculated from a Biot-Savart integral, and a discretized Laplace equation was solved to take into account boundary effects in the geometry of a finite cylinder; for details see Refs. [122, 103].

First, consider a single expanding vortex straightening in rotation. Ignoring the vortex curvature, the endpoint on the outer cell (radially oriented) will propagate along the cylinder with the speed $\alpha\Omega R$ and rotate with angular velocity $\alpha'\Omega$ (in the laboratory frame). The self-induced superfluid velocity of the vortex (together with the boundary contribution due to the image field) is mainly along \mathbf{v}_n and reduces the counterflow velocity. This does not affect the axial propagation speed substantially if the rotation velocity is large, but at low Ω the difference is easily observable, and a somewhat slower propagation speed is realized. Similarly, the self-induced velocity tends to speed up the azimuthal rotation of the vortex. This is especially visible at low temperatures where α' is small and the self-induced velocity gives the main contribution to the rotation. A smaller cylinder radius would enhance these effects further.

Similar behavior is also observed with several expanding vortices. In this case it

is easier to observe that the parts near the rotation axis are in solid body rotation. The differences in the rotation velocities between the parts in the bundle and on the outer cell (which are rotating more slowly) results in a twisted vortex configuration. In simulations a clear homogeneous twist can be observed when the number of vortices is much less than the equilibrium number. At high temperatures the twisting is barely visible but gets tighter as the temperature decreases. The wave vector of the twist is approximately given by $1/q = (1 - \alpha')/\alpha$. At very low temperatures the ordered structure partially breaks and vortex multiplication may start. The breakup is mainly because the curvature along the vortex becomes so large that the small coupling with the normal component at the region with small counterflow is not enough to keep the bundle together. In principle the axial flow caused by the twist is also increasing and can, in principle, cause the development of Kelvin waves. However, the simulations indicate that the twist breaks up due to its curvature and motion due to self induced velocity. This typically occurs at the point where a vortex terminates to the top or bottom wall or alternatively at the point where the helicity of the twist changes its sign. The details at what temperature the breakup occurs depend at least on the vortex number. With $R = 3\text{mm}$, $\Omega = 1\text{rad/s}$ and with 23 vortices the twist is stable at $T = 0.40T_c$ but at $T = 0.30T_c$ new vortices are generated due to the destruction of the helical structure and vortex reconnections.

The axial flow due to the twisted vortices is clearly seen in the simulations where $N \sim N_{\text{eq}}$. In the experimental conditions the number of vortices is typically of order 1000 or more. Computationally this is too time-consuming, since the spatial resolution has to be kept below the average inter-vortex spacing ($\sqrt{2\Omega/\kappa} \sim 0.2\text{mm}$). In practice this limits the calculations to low rotation velocities or, as was done here, to smaller cylinder radii than in the experiments. With a large number of vortices there are more reconnections between vortices that partly disrupt the twisted structure, but the twisting is still clearly visible. Figures 29 and 30 illustrate the form of the propagating front at low ($T=0.40T_c$) and high ($T=0.60T_c$) temperatures, together with the corresponding counterflow profiles. At low temperatures the front is sharp and clearly visible, but broadens at higher temperatures.

As an initial configuration for the simulations we used $N=N_{\text{eq}}$ curved vortices with one end connecting to the bottom of the cylinder, and the other bent to the side wall of the cylinder. The locations for the vortices at the bottom were chosen as the equilibrium positions of rectilinear vortex lines. The actual locations and the way how the vortices are bent to the outer cell only have a minor effect on the outcome of the simulations. This is because during the first couple of seconds the vortices move rapidly due to their curvature which breaks the ordered initial configuration.

Those vortices that are left behind the front feel a smaller azimuthal counterflow $v_n - v_{s,\phi}$ and, accordingly, their velocity of propagation slows down. This is seen in simulations at high temperatures where the twisting and the corresponding axial velocities are small. At lower temperatures the axial flow is larger and, additionally, reaches a maximum value slightly behind the front. Therefore, the vortices that are left

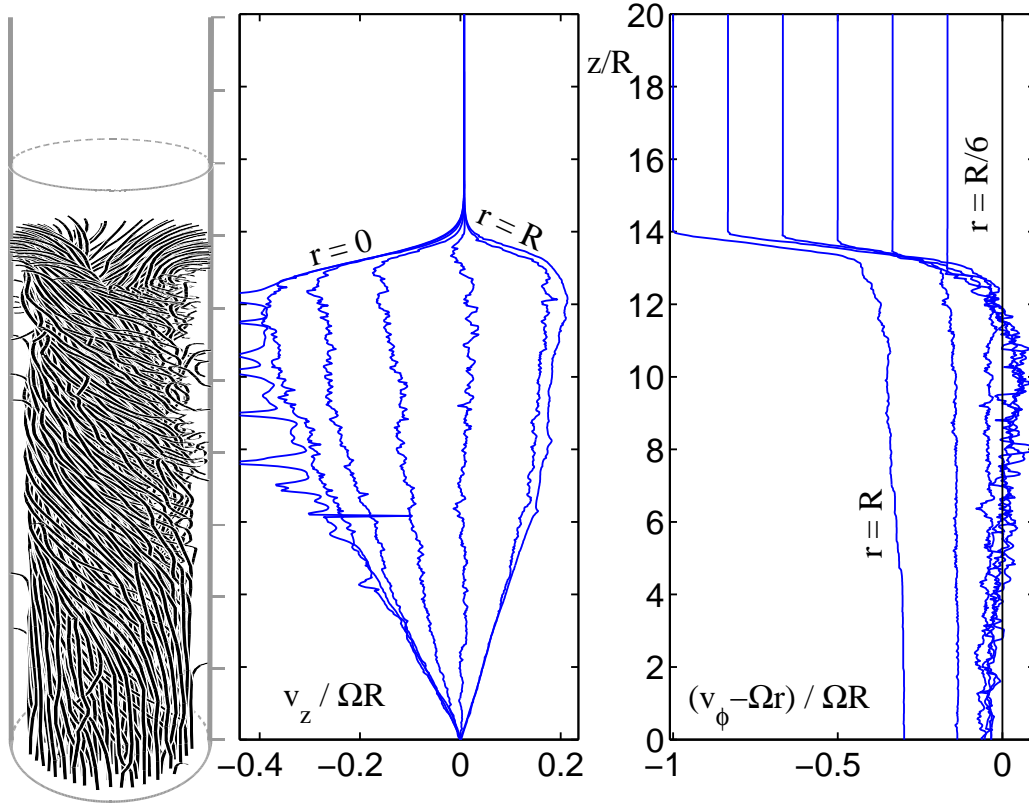


Figure 29. Vortex configuration (*left*) and counterflow velocity at $t = 60$ s from the simulations using $T = 0.40T_c$, $\Omega = 1.0$ rad/s, cylinder radius $R = 1.5$ mm and length $L = 40$ mm, of which only the lowest 30 mm are shown. For clarity the axial and radial dimensions have different scales on the left panel.

behind tend to move faster to catch up with the front. More clearly this can be seen by considering the motion of a radially oriented vortex segment on the wall. The axial velocity of this element is given by $v_{L,z} = \alpha(v_n - v_{s,\phi}) + (1 - \alpha')v_{s,z}$. At low temperatures, where α is small and $1 - \alpha'$ approaches unity, the increase in $v_{s,z}$ behind the front is sufficient to compensate for the decreased azimuthal counterflow.

At high temperatures the front also broadens since some of the vortices are left behind. These vortices still keep on generating the twist, which qualitatively explains why the relaxation of the twist slows down at high temperatures. The relaxation is mainly caused by the partial corruption of the twisted structure due to vortex reconnections and less regular vortex motion caused by the self-induced velocity contributions. The relaxation is faster than the simple unwinding of the twist which is observed when vortex number is small. Detailed calculations of the relaxation time have not yet been done.

At high temperatures the thickness of the front is found to increase with time; however, the corresponding growth rate is quite small. Here we locate the position of the front to be where the azimuthal counterflow at $r = R$ has decreased 2% from its maximum value ΩR . The back of the front is chosen to be situated at the position where

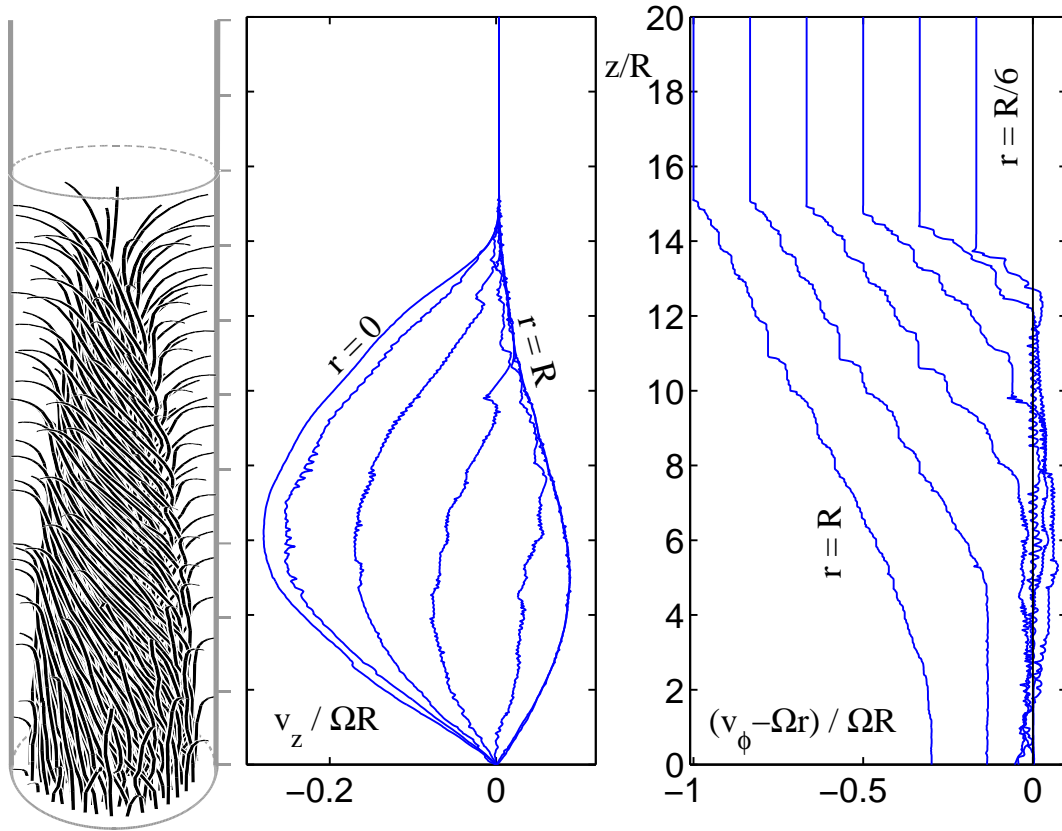


Figure 30. Vortex configuration (*left*) and counterflow velocity at $T = 0.60T_c$. The presentation and all the other parameters are as in Fig. 29.

the azimuthal counterflow at $r = R$ reaches the value half way between its maximum and minimum values (which is nonzero because of the vortex-free region outside the vortex bundle). We then define the front thickness as the difference between these two positions.

On the left in Fig 31 the propagation velocities of the vortex front are shown at a few different temperatures. At high temperatures the propagation velocity is approximately given by $\alpha\Omega R$ but at low temperatures the speed is higher. This is due to a nonzero axial velocity of the vortices at the front. Similar enhancement is also observed in experiments. The right-hand side of Fig. 31 illustrates the front thickness as a function of its location. Even if there are some quantitative differences between the simulations and experiments the main structure of the front is well reproduced. The next step would be to reproduce the profile of the vortex front using the collective description of vortex dynamics in terms of hydrodynamic equations.

6. Concluding remarks

This review discussed new features on the general phenomenon of superfluidity, which have been found in recent experiments on the superfluid phases of ^3He . New phenomena

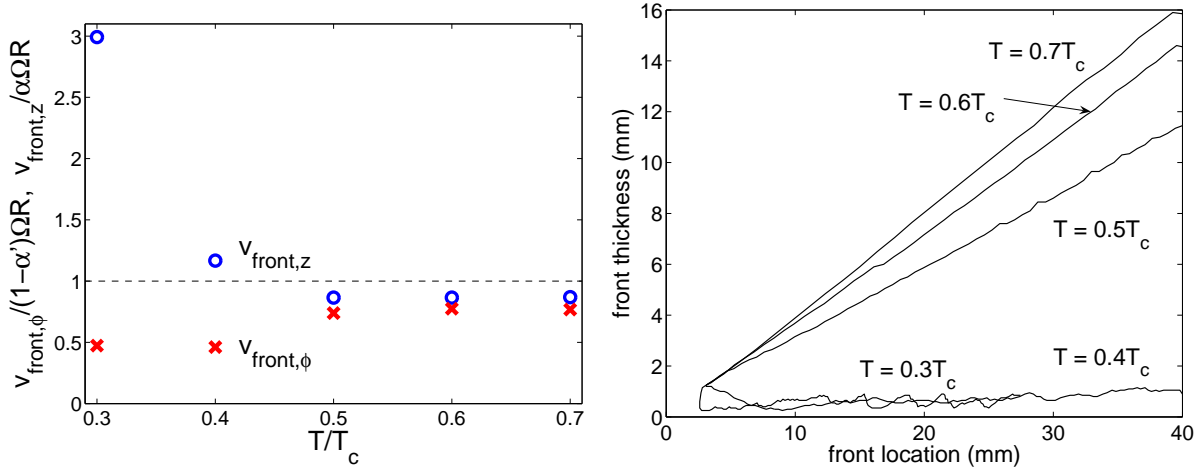


Figure 31. *Left:* Vortex-front velocity in simulations with a cylinder of radius $R = 1.5$ mm and length $L = 40$ mm rotating at $\Omega = 1.0$ rad/s. Axial velocity $v_{\text{front},z}$ (circ) was obtained from the location of the front, which was defined to be where the azimuthal counterflow at $r = R$ had decreased 2% from its maximum value. Azimuthal velocity $v_{\text{front},\phi}$ (\times) is the average velocity of the vortex endpoint at $r = R$ when the front is at $z \approx L/2$. In the averaging only the vortices within 5 mm from the front were taken into account. Here one should note the speedup ($v_{\text{front},z} > \alpha\Omega R$) of the front at low temperatures which is due to axial velocity caused by the twist. *Right:* Thickness of the front in simulations with cylinder of radius $R = 1.5$ mm and length $L = 40$ mm, rotating at $\Omega = 1.0$ rad/s. At low temperatures the axial velocity caused by the twist is enough to keep the front sharp. At higher temperatures some vortices are left behind the front and the thickness slowly increases.

have been revealed because of the much richer structure of these superfluid liquids compared to the first superfluid liquid – $^4\text{He-II}$ – where only the $U(1)$ symmetry has been spontaneously broken.

The logical chain of the discussed experiments originates from the existence of two superfluid phases, one of which – $^3\text{He-B}$ – has more or less traditional superfluid properties with quantized vortices, while the other one – $^3\text{He-A}$ – supports unconventional continuous vorticity. Under typical experimental conditions the continuous vorticity is arranged either in the form of doubly quantized vortex-skyrmions, or in the form of the meandering vortex sheet. The critical velocity for the formation of continuous vorticity is more than an order of magnitude smaller than the critical velocity for the formation of the more traditional (though nontrivial) singular vortices in $^3\text{He-B}$. This large difference allows us to construct a flow state in the rotating container, in which the equilibrium vortex state of $^3\text{He-A}$ coexists with the Landau vortex-free state of $^3\text{He-B}$ across the A-B interface.

This in turn allowed us to investigate the relative motion of two neighboring superfluids in a well-controlled and reproducible way. As a result, we were able to measure the well-defined threshold of instability for the non-dissipative shear flow of two liquids, which was impossible for the classical liquids because of their viscosity.

The outcome of these measurements, together with the theoretical analysis, shows

that there are actually two thresholds of instability. The upper one reproduces the traditional critical velocity of the relative motion of two ideal classical liquids at which the Kelvin-Helmholtz instability of the interfaces would occur in the absence of viscosity. Such a threshold can be reached in the limit of zero temperature and far from the wall of container, *i.e.* in the absence of environment. Under the conditions of the experiment, the environment cannot be avoided, and the instability takes place earlier. However, it appears that this lower threshold is also fundamental, *i.e.* it does not depend on the magnitude of the interaction with the environment. It simply requires the existence of the preferred reference frame of the environment, which in equilibrium is the frame where the normal component is at rest. Moreover, this threshold is not determined by the relative motion of the superfluid components: it is determined by the relative motion of each component with respect to the normal component.

It appears that both these thresholds have a connection to the instability of the quantum vacuum in the presence of black hole. While the lower threshold corresponds to the instability of the quantum vacuum due to the ergoregion or event horizon, the upper one corresponds to the instability of the quantum vacuum due to the presence of a physical singularity within the black hole.

The next step in the chain of the experiments has been triggered by the consequence of the interface instability after the first threshold has been reached. The development of the instability of the A-B interface leads to the injection of several vortices into the Landau vortex-free state of $^3\text{He-B}$, which is highly metastable in the rotating container. The fate of the vortices injected into the liquid which is rapidly moving with respect to the container walls appeared to depend on an intrinsic damping parameter $\Re = q^{-1} = (1 - \alpha')/\alpha$.

At high temperatures where $\Re \ll 1$ there is no evidence in our experiments of vortex multiplication even if a large number of vortex lines is injected into the flow. At the low temperature end of our experimental range, where $\Re \gtrsim 1$ the instability of individual curved vortex lines leads to the multiplication of vortices and eventually to turbulence. In other words, the parameter \Re plays a role similar to the Reynolds number of classical hydrodynamics, and turbulence becomes possible when $\Re \gtrsim 1$. The unexpected result is that the new Reynolds number is velocity independent. This conclusion is supported by numerical simulations and theoretical models. The latter allowed us to extend the theory of the developed turbulence to the case of the superfluid liquid. It was then shown that the Kolmogorov-Richardson cascade is modified in superfluids.

Finally, we investigated the development of the turbulent flow in the geometry of a long cylinder. Two important features were identified in the NMR measurements, which are related to the modern physics of the vortex matter in superfluids and superconductors: the propagating vortex front and the helically twisted vorticity. Turbulence in the rotating column is a short burst where the number of vortex lines rapidly multiplies. These are immediately polarized by the rotating flow. After the turbulent burst the vorticity moves as a front into the vortex-free region. Mutual friction causes the ends of the vortex lines in the front to spiral in a helical manner along the

cylinder wall. The front leaves behind a helically twisted vortex cluster with superflow velocity components along the rotation axis.

The main reason why the sharp hydrodynamic transition at $q_c \sim 1$ between the laminar and the turbulent flow states has only been observed in $^3\text{He-B}$ and has been missing in superfluid ^4He , is that $^3\text{He-B}$ is a Fermi liquid, where superfluidity occurs due to the mechanism of Cooper pairing. In practically all superfluid and superconducting systems with Cooper pairing the mutual friction parameter $q(T)$ crosses unity at $T \sim 0.5T_c$ (if the spectrum of fermionic quasiparticles is fully gapped and in the so-called clean limit, when the effects of impurities can be neglected). It is interesting that the mechanism of the mutual friction, due to which we have a fortunate coincidence of a hydrodynamic transition right in the middle of the experimentally accessible temperature range, has many common with the phenomenon of chiral anomaly in relativistic quantum field theories.

An important message we wish to emphasize is that, as distinct from the traditional superfluid liquid $^4\text{He-II}$, superfluid ^3He incorporates interacting Fermi and Bose quantum fields, similar to that in relativistic quantum theory. Moreover, if the superfluid/superconducting system has a sufficiently rich order parameter, the analogy becomes stronger: the elementary quasiparticles serve as the counterpart of elementary particles – electron, neutrino, and quarks – while the propagating collective modes of the system resemble gauge fields and gravity. In the broader context, studying the phenomena discussed in this review, we have found that superfluid ^3He liquids provide information for the benefit of many fields in physics. These include superfluidity in general, coexistence of quantum vacua across the interface and brane physics, general physics of topological defects (skyrmions, boojums, cosmic strings, etc.), hydrodynamic instabilities (instability of the interface between moving liquids, Kelvin wave instability of a vortex line, etc.), black-hole horizon, ergoregion and singularity within the black hole, the general phenomenon of turbulence, superconductivity, chiral anomaly for relativistic quantum fields, front propagation, Kibble-Zurek mechanism in cosmology, dark-matter detectors etc. All this combines to an astonishing manifestation of the unity of physics.

Acknowledgements

The work was supported in part by the Russian Foundation for Basic Research under grant 06-02-16002-a and by the ESF program COSLAB.

Appendix: Nuclear magnetic resonance in $^3\text{He-B}$

The vortex detection method in our experiments is based on continuous-wave nuclear magnetic resonance (cw-NMR); for details of the measurement electronics, see Ref. [123]. The resonance lineshape provides information on the spatial variation of the order parameter in the $^3\text{He-B}$ sample. This variation, or texture, is affected by presence

of vortices. Probing the NMR lineshape thus constitutes an indirect method of vortex detection. Here we present the main ingredients needed to understand the textures and NMR signals of $^3\text{He-B}$ in a rotating cylinder.

The bulk tensor order parameter of undisturbed $^3\text{He-B}$ can be written in the form $\mathbf{A} = \Delta e^{i\phi} \mathbf{R}(\hat{\mathbf{n}}, \theta)$, where the (real-valued) quantities Δ and ϕ are the magnitude and the phase of the order parameter, and \mathbf{R} is a rotation matrix which can be parametrized by a unit vector $\hat{\mathbf{n}}$ and an angle θ as $R_{\mu j} = \cos \theta \delta_{\mu j} + (1 - \cos \theta) \hat{n}_\mu \hat{n}_j - \sin \theta \epsilon_{\mu j k} \hat{n}_k$. While Δ and ϕ are usually fixed by external constraints and θ by the dipole-dipole interaction, the variable $\hat{\mathbf{n}}$ is more susceptible to various different orientational effects, giving rise to the textures $\hat{\mathbf{n}}(\mathbf{r})$. The appropriate texture in equilibrium represents a minimum of a free-energy functional, the main contributions to which in the presence of an external magnetic field \mathbf{H} are the field anisotropy energy

$$F_{DH} = -a \int d^3\mathbf{r} (\hat{\mathbf{n}} \cdot \mathbf{H})^2, \quad (63)$$

the surface energy (the unit vector $\hat{\mathbf{s}}$ denotes the surface normal)

$$F_{SH} = -d \int d^2\mathbf{r} (\mathbf{H} \cdot \mathbf{R} \cdot \hat{\mathbf{s}})^2, \quad (64)$$

the energy due to the counterflow velocity field $\mathbf{v}(\mathbf{r}) = \mathbf{v}_n(\mathbf{r}) - \mathbf{v}_s(\mathbf{r})$

$$F_{HV} = -\lambda_{HV} \int d^3\mathbf{r} (\mathbf{H} \cdot \mathbf{R} \cdot \mathbf{v})^2, \quad (65)$$

and the vortex contribution

$$F_{LH} = \int_L d^3\mathbf{r} \lambda_{LH} (\mathbf{H} \cdot \mathbf{R} \cdot \hat{\mathbf{l}})^2, \quad (66)$$

where $\hat{\mathbf{l}}$ is a unit vector directed along the vortex line and the integration extends over the volume occupied by vortices (the information on the vortex density is contained in λ_{LH}). Our notation follows that of Ref. [124]. In addition to the above energy terms, spatially varying order-parameter distributions are associated with a gradient (or bending) energy

$$F_G = \int d^3\mathbf{r} \left[\lambda_{G1} \frac{\partial R_{\mu i}}{\partial r_i} \frac{\partial R_{\mu j}}{\partial r_j} + \lambda_{G2} \frac{\partial R_{\mu j}}{\partial r_i} \frac{\partial R_{\mu j}}{\partial r_i} \right] + \lambda_{SG} \int d^2\mathbf{r} \hat{s}_j R_{\mu j} \frac{\partial R_{\mu i}}{\partial r_i}. \quad (67)$$

The characteristic length scale of the textures can be obtained by balancing the gradient energy with the bulk magnetic energy F_{DH} : this magnetic coherence length is defined as $\xi_H = \sqrt{65\lambda_{G2}/(8aH^2)}$, and is inversely proportional to the magnitude of the external magnetic field. Since the typical values of ξ_H are of the order of a millimeter, the textures are very extended. Therefore, with typical experimental setups the finite container size and the associated boundary effects are important, and need to be taken into account.

Also, it should be noted that the presence of vortices in the sample volume modifies the texture on several different ways. The free-energy term F_{LH} contains both the effect of order-parameter suppression at the vortex cores, and the orientational effect of the

quantized superflow fields circulating the cores. Additionally, the vortices modify the global counterflow velocity field $\mathbf{v}(\mathbf{r})$ entering the expression of F_{HV} ; this is typically the dominating effect.

In a long cylindrical container with the external magnetic field directed along the axis, the minimum-energy $\hat{\mathbf{n}}$ texture has an axially symmetric or flare-out form [125, 126]. In cylindrical coordinates, this can be represented in a form

$$\hat{\mathbf{n}}(\mathbf{r}) = -\sin\beta(r)\cos\alpha(r)\hat{\mathbf{r}} + \sin\beta(r)\sin\alpha(r)\hat{\boldsymbol{\phi}} + \cos\beta(r)\hat{\mathbf{z}}. \quad (68)$$

The NMR resonance frequency depends on the polar angle β as

$$\nu(\beta) \approx \nu_0 + \frac{\nu_B^2}{2\nu_0} \sin^2\beta, \quad (69)$$

where $\nu_0 = \gamma H/(2\pi)$ and ν_B are the Larmor frequency and the B-phase longitudinal resonance frequency, respectively. This approximate expression is valid at high external fields when $\nu_B \ll \nu_0$, which is the relevant regime for the experiments presented here. In the local oscillator picture (excluding line broadening effects), spatially varying $\beta(r)$ leads to a distribution of resonance frequencies, which then define the absorption spectrum [127]

$$P(\nu) \propto \int dr r \delta[\nu - \nu(r)], \quad (70)$$

where $\nu(r) \equiv \nu[\beta(r)]$. This defines the connection between the order-parameter texture $\beta(r)$, found by minimizing the sum of Eqs. (63)–(67), and the measured lineshape $P(\nu)$.

The form of the relevant free-energy functional in rotating ^3He -B is very complicated, giving rise to several different types of equilibrium textures depending on the magnitude and direction of the counterflow in the sample [128]. However, a rough qualitative view of the textures can be obtained relatively easily. First, consider the situation with an axial magnetic field and zero counterflow: through Eq. (63) the field tends to align $\hat{\mathbf{n}} \parallel \mathbf{H}$, or $\sin^2\beta = 0$, in bulk. Through Eq. (69), this corresponds to NMR absorption at the Larmor frequency ν_0 . However, the surface energy at the cylindrical sidewall, Eq. (64) with $\hat{\mathbf{s}} = -\hat{\mathbf{r}}$, favors the orientation $\sin^2\beta = 4/5$ and leads to the shifting of the NMR absorption towards higher frequencies. A combination of these two orienting effects and the gradient energy creates the characteristic low counterflow NMR lineshape with a long tail, as exhibited by Figs. 32 and 33.

If the sample is put to rotation with angular velocity Ω , maintaining the vortex-free state, azimuthal counterflow $\mathbf{v}(r) = \Omega r \hat{\boldsymbol{\phi}}$ is created. Since the flow energy F_{HV} in this case is also minimized by having $\sin^2\beta = 4/5$, this leads to the formation of the so-called counterflow peak in the NMR spectrum (see Figs. 32 and 33). However, in the equilibrium rotating state the sample contains rectilinear vortices oriented parallel to the axis of rotation, evenly distributed with an areal density such that the counterflow vanishes on the average. In this case, the NMR lineshape is very similar to that of the nonrotating sample; the small shift of absorption away from the Larmor region seen in Figs. 32 and 33 is due to the local contribution F_{LH} .

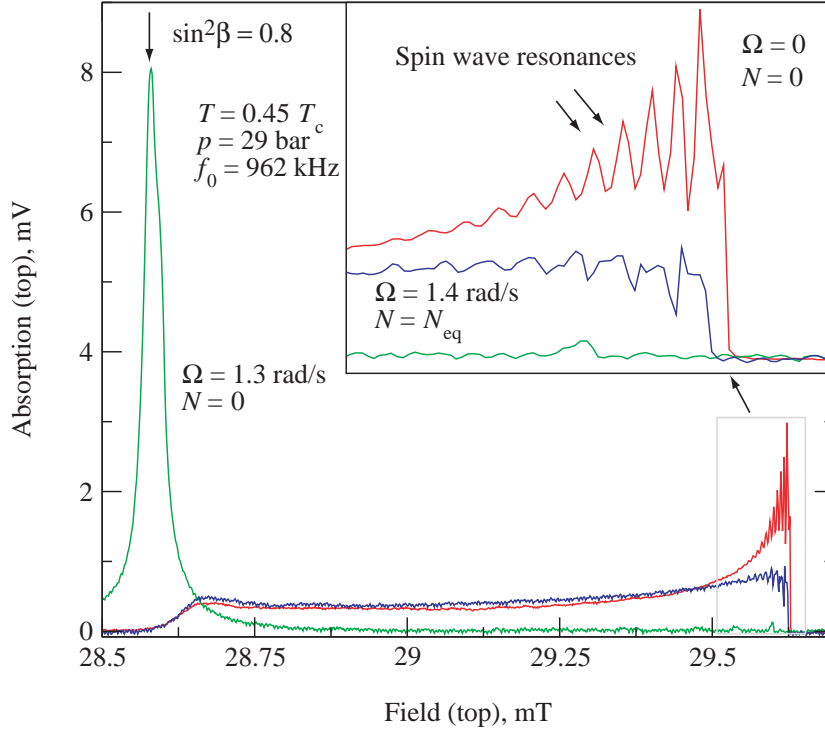


Figure 32. Spectra measured with the top spectrometer as a function of the polarizing field. The Larmor field is at 29.63 mT, the value around which the signal above T_c is centered. In the superfluid the signal forms a sharp edge at the Larmor value. (*Insert*) Spin wave resonances are clearly visible close to the Larmor edge in the top spectrometer. The strong spin wave excitations at low temperatures make the top spectrometer impractical for measurements in the Larmor region. For this reason this spectrometer is used to monitor the counterflow peak height at $\sin^2 \beta = 4/5$ in most measurements.

In general, metastable states containing a cluster of any number of vortices N between zero and the equilibrium number N_{eq} can be observed in rotating $^3\text{He-B}$. In such a case, the magnitude of the azimuthal counterflow is

$$v(r) = \begin{cases} 0, & 0 < r < R_v, \\ \Omega r - \Omega R_c^2/r, & R_c < r < R, \end{cases} \quad (71)$$

where the cluster radius $R_c = R\sqrt{N/N_{eq}}$. However, under transient conditions, or beyond the onset for superfluid turbulence, also more complicated flow profiles can arise, which are no longer necessary purely azimuthal. In particular, this was the case with a twisted vortex cluster left behind an advancing vortex front, as discussed in Sec. 5: the nonzero axial component of the counterflow velocity gave rise to excess absorption at the Larmor frequency.

In summary, NMR in $^3\text{He-B}$ has proven a powerful method in detecting different flow states and vortex configurations, when good models for the corresponding counterflow profiles are available. Such models can be obtained from either analytical

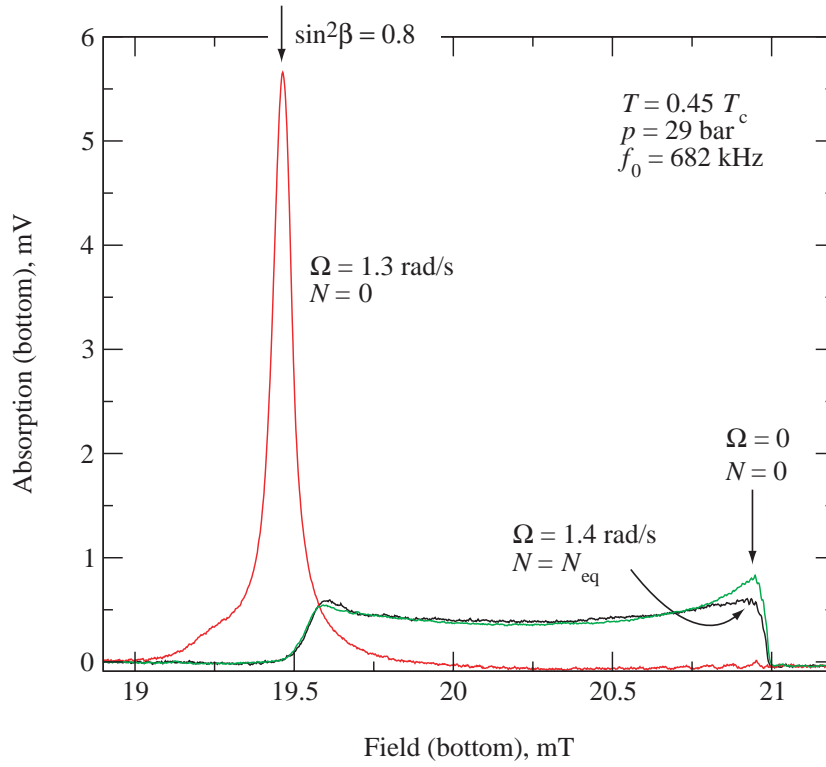


Figure 33. Spectra measured with the bottom spectrometer. Some spin wave resonances are already visible, but are much less prominent than in the top spectrometer. At still lower temperature $\sim 0.35 T_c$ the spin wave amplitude grows and they expand all throughout the spectrum (see Ref. [94]). This spectrometer is used in most measurements for recording the absorption close to the Larmor edge.

arguments, or from detailed numerical simulations. The latter ones are especially valuable in complicated dynamic situations.

- [1] Vinen W F and Niemela J 2002 *J. Low Temp. Phys.* **128** 167
- [2] Salomaa M M and Volovik G E 1987 *Rev. Mod. Phys.* **59** 533
- [3] Eltsov V B, Krusius M and Volovik G E 2005 in B Halperin, ed, *Progress in Low. Temp. Phys.*, Vol. XV (Amsterdam: Elsevier) pp 1–137
- [4] Volovik G E, Eltsov V B and Krusius M 2002 *Vortices in unconventional superconductors and superfluids* vol 132 of *Series in Solid-State Science* (Springer) p 21
- [5] Volovik G E 2003 *The Universe in a Helium Droplet* (Oxford, UK: Oxford University Press)
- [6] Vollhardt D and Wölfle P 1990 *The Superfluid Phases of Helium 3* (London: Taylor and Francis)
- [7] Varoquaux E, Avenel O, Mukharsky Y and Hakonen P 2000 in C F Barenghi, R J Donnelly and W F Vinen, eds, *Quantized Vortex Dynamics and Superfluid Turbulence* (Berlin: Springer)
- [8] Korshunov S 1991 *Europhys. Lett.* **16** 673
- [9] Korshunov S E 2002 *JETP Lett.* **75** 423
- [10] Abanin D 2003 *JETP Lett.* **77** 191
- [11] Finne A P, Araki T, Blaauwgeers R, Eltsov V B, Kopnin N B, Krusius M, Skrbek L, Tsubota M and Volovik G E 2003 *Nature* **424** 1022
- [12] Kopnin N B and Salomaa M M 1991 *Phys. Rev. B* **44** 9667
- [13] Kopnin N 1995 *Physica B* **210** 267
- [14] Kopnin N B and Lopatin A V 1997 *Phys. Rev. B* **56** 766
- [15] Kopnin N B 2002 *Rep. Prog. Phys.* **65** 1633
- [16] Fisher S N, Hale A, Guénault A M and Pickett G R 2001 *Phys. Rev. Lett.* **86** 244
- [17] Bradley D, Clubb D, Fisher S, Guénault A, Haley R, Matthews C, Pickett G, Tzepelin V and Zaki K 2005 *Phys. Rev. Lett.* **95** 35302
- [18] Enrico M, Fisher S, Guénault A, Pickett G and Torizuka K 1993 *Phys. Rev. Lett.* **70** 1846
- [19] Fisher S, Hale A, Guénault A, Pickett G and Torizuka K 2001 *Phys. Rev. Lett.* **86** 244
- [20] Bradley D, Fisher S, Guénault A, Lowe M, Pickett G, Rahm A and Whitehead R 2004 *Phys. Rev. Lett.* **93** 235302
- [21] Bradley D, Clubb D, Fisher S, Guénault A, Haley R, Matthews C, Pickett G, Tzepelin V and Zaki K 2006 *Phys. Rev. Lett.* **96** 035301
- [22] Belotsky K, Bunkov Y, Godfrin H, Khlopov M and Konoplich R 2006 *astro-ph/0606350*
- [23] Tilley D R and Tilley J 1990 *Superfluidity and superconductivity* 3rd ed (Bristol, UK: IOP Publishing)
- [24] Donnelly R 1991 *Quantized vortices in helium II* (Cambridge, UK: Cambridge University Press)
- [25] Pekola J P, Simola J T, Hakonen P J, Krusius M, Lounasmaa O V, Nummila K K, Mamniashvili G, Packard R E and Volovik G E 1984 *Phys. Rev. Lett.* **53** 584
- [26] Thuneberg E V 1986 *Phys. Rev. Lett.* **56** 359
- [27] Ikkala O, Volovik G, Hakonen P, Bunkov Y, Islander S and Kharadze G 1982 *JETP Lett.* **35** 416
- [28] Kondo Y, Korhonen J S, Krusius M, Dmitriev V V, Thuneberg E V and Volovik G E 1992 *Phys. Rev. Lett.* **68** 3331
- [29] Korhonen J, Kondo Y, Krusius M, Thuneberg E and Volovik G 1993 *Phys. Rev. B* **47** 8868
- [30] Mermin N D and Ho T L 1976 *Phys. Rev. Lett.* **36** 594
- [31] Blaauwgeers R, Eltsov V B, Krusius M, Ruohio J J, Schanen R and Volovik G E 2000 *Nature* **404** 471
- [32] Parts Ü, Karimäki J, Koivuniemi J, Krusius M, Ruutu V, Thuneberg E and Volovik G 1995 *Phys. Rev. Lett.* **75** 3320
- [33] Karimäki J and Thuneberg E V 1999 *Phys. Rev. B* **60** 15290
- [34] Parts Ü, Thuneberg E, Volovik G, Koivuniemi J, an M Heinilä V R, Karimäki J and Krusius M 1994 *Phys. Rev. Lett.* **72** 3839
- [35] Parts Ü, Ruutu V, Koivuniemi J, Krusius M, Thuneberg E and Volovik G 1995 *Physica B* **210** 311
- [36] Eltsov V and Krusius M 2000 *Proc. Nato Advanced Study Institute* **549**, Series C 325
- [37] Onsager L 1949 *Suppl. Nuovo Cimento* **6** 249

- [38] Feynman R P 1955 in C J Gorter, ed, *Progress in Low Temperature Physics* **1** (Amsterdam: North-Holland) pp 17–53
- [39] Chechetkin V 1976 *Sov. Phys. JETP* **44** 766
- [40] Anderson P W and Toulouse G 1977 *Phys. Rev. Lett.* **38** 508
- [41] Ruutu V, Ruohio J, Krusius M, Plaçais B and Sonin E 1998 *Physica B* **255** 27
- [42] Krusius M, Korhonen J, Kondo Y and Sonin E 1993 *Phys. Rev. B* **47** 15113
- [43] Feynman R 1955 in C Gorter, ed, *Progress in Low Temperature Physics* vol 1 (Amsterdam: North Holland) p 36
- [44] Ruutu V M H, Parts Ü, Koivuniemi J, Kopnin N B and Krusius M 1997 *J. Low Temp. Phys.* **107** 93
- [45] Parts Ü, Ruutu V, Koivuniemi J, Bunkov Y, Dmitriev V, Fogelström M, Huebner M, Kondo Y, Kopnin N, Korhonen J, Krusius M, Lounasmaa O, Soininen P and Volovik G 1995 *Europhys. Lett.* **31** 449
- [46] Ruutu V, Parts Ü, Koivuniemi J, Kopnin N and Krusius M 1997 *J. Low Temp. Phys.* **107** 93
- [47] Soininen P I and Kopnin N B 1994 *Phys. Rev. B* **49** 12087
- [48] Packard R 1998 *Rev. Mod. Phys.* **70** 641
- [49] Varoquaux E in *Topological defects and the non-equilibrium dynamics of symmetry-breaking phase transitions* (Kluwer Academic Publishers, Netherlands)
- [50] Davis J, Steinhauer J, Schwab K, Mukharsky Y, Amar A, Sasaki Y and Packard R 1992 *Phys. Rev. Lett.* **69** 323
- [51] Ihas G, Avenel O, Aarts R, Salmelin R and Varoquaux E 1992 *Phys. Rev. Lett.* **69** 327
- [52] Awschalom D D and Schwarz K W 1984 *Phys. Rev. Lett.* **52** 49
- [53] Parts Ü, Karimäki J M, Koivuniemi J H, Krusius M, Ruutu V M H, Thuneberg E V and Volovik G E 1995 *Phys. Rev. Lett.* **75** 3320
- [54] Ruutu V M H, Kopu J, Krusius M, Parts Ü, Plaçais B, Thuneberg E V and Xu W 1997 *Phys. Rev. Lett.* **79** 5058
- [55] Vollhardt D and Maki K 1979 *Phys. Rev. B* **20** 963
- [56] Kopu J, Hänninen R and Thuneberg E V 2000 *Phys. Rev. B* **62** 12374
- [57] Blaauwgeers R, Eltsov V B, Eska G, Finne A P, Haley R P, Krusius M, Ruohio J J, Skrbek L and Volovik G E 2002 *Phys. Rev. Lett.* **89** 155301
- [58] Hänninen R, Blaauwgeers R, Eltsov V B, Finne A P, Krusius M, Thuneberg E V and Volovik G E 2003 *Phys. Rev. Lett.* **90** 225301
- [59] Parts Ü, Kondo Y, Korhonen J S, Krusius M and Thuneberg E V 1993 *Phys. Rev. Lett.* **71** 2951
- [60] Krusius M, Thuneberg E V and Parts Ü 1994 *Physica B* **197** 376
- [61] Khalatnikov I M 1965 *An Introduction to the Theory of Superfluidity* (New York: Benjamin, Inc)
- [62] Kopnin N B 2001 *Theory of Nonequilibrium Superconductivity* (Oxford: Oxford University Press)
- [63] Hall H E and Vinen W F 1956 *Proc. Roy. Soc. A* **238** 215
- [64] Bevan T D C, Manninen A J, Cook J B, Alles H, Hook J R and Hall H E 1997 *J. Low Temp. Phys.* **109** 423
- [65] Bevan T D C, Manninen A J, Cook J B, Armstrong A J, Hook J R and Hall H E 1995 *Phys. Rev. Lett.* **74** 750 (correction **74**, 3092, 1995)
- [66] Kopnin N B 1993 *Phys. Rev. B* **47** 14354
- [67] Donnelly R J and Barenghi C F 1998 *J. Phys. Chem. Ref. Data* **27** 1217
- [68] Sonin E B 1987 *Rev. Mod. Phys.* **59** 87
- [69] Swanson C E, Barenghi C F and Donnelly R J 1983 *Phys. Rev. Lett.* **50** 190
- [70] Glaberson W I, Johnson W W and Ostermeyer R M 1974 *Phys. Rev. Lett.* **33** 1197
- [71] Ostermeyer R M and Glaberson W I 1975 *J. Low Temp. Phys.* **21** 191
- [72] Tsubota M, Araki T and Barenghi C 2003 *Phys. Rev. Lett.* **90** 205301
- [73] Sonin E B and Krusius M 1994 in N Bontemps, Y Bruynseraede, G Deutcher and A Kapitulinik, eds, *The Vortex State* (Netherlands: Kluwer Academic Publishing)
- [74] Barenghi C, Donnelly R and Vinen W 1985 *Phys. Fluids* **28** 498

- [75] Chandrasekhar S 1981 *Hydrodynamic and hydromagnetic stability* (New York: Dover Publications)
- [76] Lamb H 1945 *Hydrodynamics* (New York: Dover Publications)
- [77] Schiffer P, O’Keefe M T, Hildreth M D, Fukuyama H and Osheroff D D 1992 *Phys. Rev. Lett.* **69** 120
- [78] Lord Kelvin (Sir William Thomson) 1910 *Hydrodynamics and General Dynamics* vol 4 (Cambridge, UK: Cambridge University Press)
- [79] Lord Rayleigh (J W Strutt) 1899 *Scientific papers* vol 1 (Cambridge University Press)
- [80] Birkhoff G 1962 in *Hydrodynamic Instability* vol XIII (Providence, RI, USA: American Mathematical Society) pp 55–76
- [81] Volovik G E 2002 *JETP Letters* **75** 491
- [82] Ruokola T and Kopu J 2005 *JETP Lett.* **81** 634
- [83] Andersson N, Comer G and Prix R 2002 *Mon. Not. Roy. Astron. Soc.*
- [84] Landau L and Lifshitz E 1987 *Fluid Mechanics* 2nd ed (Oxford, UK: Pergamon Press)
- [85] Kopnin N 1987 *JETP. Lett.* **65** 1187
- [86] Leggett A J and Yip S 1990 in W P Halperin and L P Pitaevskii, eds, *Helium Three* (Netherlands: Elsevier Science) pp 523–607
- [87] Yip S and Leggett A J 1986 *Phys. Rev. Lett.* **57** 345
- [88] Volovik G 2002 *JETP. Lett.* **76** 240
- [89] Schützhold R and Unruh W 2002 *Phys. Rev. D* **66** 044019
- [90] J Zhang S Childress A U and Shelley M 2000 *Nature* **408** 835
- [91] Madison K W, Chevy F, Bretin V and Dalibard J 2001 *Phys. Rev. Lett.* **86** 4443
- [92] Sinha S and Castin Y 2001 *Phys. Rev. Lett.* **87** 190402
- [93] Aranson I S, Kopnin N B and Vinokur V M 2001 *Phys. Rev. B* **63** 184501
- [94] Finne A, Boldarev S, Eltsov V and Krusius M 2004 *J. Low Temp. Phys.* **136** 249
- [95] Eltsov V, Blaauwgeers R, Finne A P, Krusius M, Ruohio J and Volovik G 2003 *Physica B* **329-333** 96
- [96] Zieve R, Mukharsky Y, Close J, Davis J and Packard R 1993 *J. Low Temp. Phys.* **91** 315
- [97] Zieve R, Close J, Davis J and Packard R 1993 *J. Low Temp. Phys.* **90** 243
- [98] Finne A, Boldarev S, Eltsov V and Krusius M 2005 *J. Low Temp. Phys.* **138** 567
- [99] Faber T 1995 *Fluid dynamics for physicists* (Cambridge: Cambridge University Press)
- [100] Hof B, Juel A and Mullin T 2003 *Phys. Rev. Lett.* **91** 244502
- [101] Frisch U 1995 *Turbulence: The legacy of A.N. Kolmogorov* (Cambridge: Cambridge University Press)
- [102] Vinen W F 1957 *Proc. R. Soc. London Ser. A.* **242** 493
- [103] Schwarz K W 1988 *Phys. Rev. B* **38** 2398
- [104] Tsubota M, Araki T and Barenghi C F 2003 *Phys. Rev. Lett.* **90** 205301
- [105] Kivotides D and Leonard A 2003 *Phys. Rev. Lett.* **90** 234503
- [106] Chatelain P, Kivotides D and Leonard A 2003 *Phys. Rev. Lett.* **90** 054501
- [107] Schwarz K W and Rozen J 1991 *Phys. Rev. B* **44** 7563
- [108] L’vov V S, Nazarenko S V and Volovik G E 2004 *JETP Letters* **80** 546
- [109] Kovasznay L 1947 *J. Aeronaut. Sci.* **15** 745
- [110] Leith C 1967 *Phys. Fluids* **10** 1409
- [111] Leith C 1968 *Phys. Fluids* **11** 1612
- [112] Connaughton C and Nazarenko S 2004 *Phys. Rev. Lett.* **92** 044501
- [113] Laval J P, Dubrulle B and Nazarenko S 2001 *Phys. of Fluids* **13** 1995
- [114] Vinen W F 2005 *Phys. Rev. B* **71** 24513
- [115] Skrbek L 2004 *JETP Lett.* **80** 484
- [116] Vinen W F 2000 *Phys. Rev. B* **61** 1410
- [117] L’vov V S, Nazarenko S V and Skrbek L 2006 *nlin.CD/0606002*
- [118] Finne A P, Eltsov V B, Blaauwgeers R, Krusius M, Janu Z and Skrbek L 2004 *J. Low Temp.*

- Phys.* **134** 375
- [119] Ruutu V M H, Eltsov V B, Gill A J, Kibble T W B, Krusius M, Makhlin Y M, Placais B, Volovik G E and Xu W 1996 *Nature* **382** 334
 - [120] Finne A P, Eltsov V, Eski G, Hänninen R, Kopu J, Krusius M, Thuneberg E V and Tsubota M 2006 *Phys. Rev. Lett.* **96** 085301
 - [121] Eltsov V B, Finne A P, Hänninen R, Kopu J, Krusius M, Tsubota M and Thuneberg E V 2006 *Phys. Rev. Lett.* **96** 215302
 - [122] Schwarz K W 1985 *Phys. Rev. B* **31** 5782
 - [123] Koivuniemi J 1998 *Nuclear Magnetic Resonance Techniques in the Measurement of Superfluid ^3He Vortices* Ph.D. thesis Helsinki University of Technology
 - [124] Thuneberg E V 2001 *J. Low Temp. Phys.* **122** 657
 - [125] Smith H, Brinkman W F and Engelsberg S 1977 *Phys. Rev. B* **15** 199
 - [126] Osheroff D D 1977 *Physica B* **90** 20
 - [127] Hakonen P J, Krusius M, Salomaa M M, Salmelin R H, Simola J T, Gongadze A D, Vachnadze G E and Kharadze G A 1989 *J. Low Temp. Phys.* **76** 225
 - [128] Korhonen J S, Gongadze A D, Janu Z, Kondo Y, Krusius M, Mukharsky Y M and Thuneberg E V 1990 *Phys. Rev. Lett.* **65** 1211